

1 SEARCH FOR PRODUCTION OF A HIGGS BOSON AND A SINGLE TOP
2 QUARK IN MULTILEPTON FINAL STATES IN pp COLLISIONS AT $\sqrt{s} = 13$
3 TeV.

4 by

5 Jose Andres Monroy Montañez

6 A DISSERTATION

7 Presented to the Faculty of

8 The Graduate College at the University of Nebraska

In Partial Fulfilment of Requirements

10 For the Degree of Doctor of Philosophy

11 Major: Physics and Astronomy

12 Under the Supervision of Kenneth Bloom and Aaron Dominguez

13 Lincoln, Nebraska

14 July, 2018

15 SEARCH FOR PRODUCTION OF A HIGGS BOSON AND A SINGLE TOP
16 QUARK IN MULTILEPTON FINAL STATES IN pp COLLISIONS AT $\sqrt{s} = 13$
17 TeV.

18 Jose Andres Monroy Montañez, Ph.D.

19 University of Nebraska, 2018

20 Adviser: Kenneth Bloom and Aaron Dominguez

²¹ Table of Contents

²²	Table of Contents	iii
²³	List of Figures	vii
²⁴	List of Tables	x
²⁵	1 INTRODUCTION	1
²⁶	2 Theoretical approach	2
²⁷	2.1 Introduction	2
²⁸	2.2 Standard model of particle physics	3
²⁹	2.2.1 Fermions	5
³⁰	2.2.1.1 Leptons	6
³¹	2.2.1.2 Quarks	9
³²	2.2.2 Fundamental interactions	13
³³	2.2.3 Gauge Bosons	18
³⁴	2.3 Electroweak unification and the Higgs mechanism	20
³⁵	2.3.1 Spontaneous symmetry breaking (SSB)	28
³⁶	2.3.2 Higgs mechanism	32
³⁷	2.3.3 Masses of the gauge bosons	34

38	2.3.4	Masses of the fermions	35
39	2.3.5	The Higgs field	36
40	2.3.6	Higgs boson production mechanisms at LHC.	37
41	2.3.7	Higgs decay channels	41
42	2.4	Associated Production of Higgs Boson and Single Top Quark.	42
43	2.5	The CP-mixing in tH processes	47
44	2.6	Experimental status of anomalous Higg-fermion coupling.	51
45	3	The CMS experiment at the LHC	53
46	3.1	Introduction	53
47	3.2	The LHC	54
48	3.3	The CMS experiment	64
49	3.3.1	Coordinate system	66
50	3.3.2	Pixels detector	67
51	3.3.3	Silicon strip tracker	69
52	3.3.4	Electromagnetic calorimeter	71
53	3.3.5	Hadronic calorimeter	72
54	3.3.6	Superconducting solenoid magnet	74
55	3.3.7	Muon system	75
56	3.3.8	CMS trigger system	76
57	3.3.9	CMS computing	78
58	3.4	Event generation simulation and reconstruction	82
59	3.4.1	event generation	82
60	3.4.2	Hard scattering	82
61	3.4.3	parton shower	82
62	3.4.4	hadronization and decays	82

63	3.4.5	underlying events and pileup	82
64	3.4.6	MC - MadEvent, MadGraph and madgraphNLO, powheg, pythia, tauola	82
65	3.4.7	detector simulation	82
66	3.4.8	event reconstruction- particle flow algorithm, vertexing , muon reco, electron reco, photon and hadron reco, jets reco, anti-kt algoritm, jet energy corrections, btagging, MET	82
67	3.4.9	MVA methods, NN, BDT, boosting, overtraining, variable ranking	82
68	3.4.10	statistical inference, likelihood parametrization	82
69	3.4.11	nuisance paraeters	82
70	3.4.12	exclusion limits	82
71	3.4.13	asymptotic limits	82
72	4	Search for production of a Higgs boson and a single top quark in multilepton final states in pp collisions at $\sqrt{s} = 13$ TeV	83
73	4.1	Introduction	83
74	4.2	Data and MC Samples	85
75	4.2.1	Full 2016 dataset and MC samples	85
76	4.2.2	Triggers	88
77	4.2.2.1	Trigger efficiency scale factors	88
78	4.3	Object Identification and event selection	89
79	4.3.1	Jets and b tagging	89
80	4.3.2	Lepton selection	90
81	4.3.3	Lepton selection efficiency	91
82	4.4	Background predictions	92

88	4.5 Signal discrimination	93
89	4.5.1 Classifiers response	97
90	4.6 Additional discriminating variables	100
91	5 The CMS forward pixel detector	103
92	5.0.1 The phase 1 FPix upgrade	103
93	5.0.2 FPix module production line	103
94	5.0.3 The Gluing stage	103
95	5.0.4 The Encapsulation stage	103
96	5.0.5 The FPix module production yields	103
97	Bibliography	103
98	References	104

⁹⁹ List of Figures

100	1.1	^{14}N neutron capture in a PECVD polymerized pyridine film. The Q-value of this reaction is 626 keV. Taken from [22]	1
102	2.1	Standard model of particle physics.	4
103	2.2	WI transformations between quarks	12
104	2.3	Fundamental interactions in nature.	13
105	2.4	SM interactions diagrams	14
106	2.5	Neutral current processes	21
107	2.6	Spontaneous symmetry breaking mechanism	28
108	2.7	SSB Potential form	30
109	2.8	Potential for complex scalar field	30
110	2.9	SSB mechanism for complex scalar field	31
111	2.10	Proton-Proton collision	38
112	2.11	Higgs production mechanism Feynman diagrams	39
113	2.12	Higgs production cross section and decay branching ratios	40
114	2.13	Associated Higgs production mechanism Feynman diagrams	43
115	2.14	Cross section for tHq process as a function of κ_t	45
116	2.15	Cross section for tHW process as a function of κ_{Htt}	46
117	2.16	NLO cross section for tX_0 and $t\bar{t}X_0$	49

118	2.17 NLO cross section for $tWX_0, t\bar{t}X_0$	50
119	2.18 Combined coupling modifiers κ_t - κ_V fits of ATLAS and CMS.	51
120	3.1 CERN accelerator complex	54
121	3.2 LHC protons source and first acceleration stage.	55
122	3.3 The LINAC2 accelerating system at CERN.	56
123	3.4 LHC layout and RF cavities module.	57
124	3.5 LHC dipole magnet.	59
125	3.6 2016 CMS Integrated luminosity	61
126	3.7 LHC interaction points	62
127	3.8 Multiple pp collision bunch crossing at CMS.	64
128	3.9 CMS detector drawing	65
129	3.10 CMS coordinate system	66
130	3.11 CMS pixel detector schematic view.	68
131	3.12 SST Schematic view.	69
132	3.13 CMS ECAL schematic view	71
133	3.14 CMS HCAL schematic view	73
134	3.15 CMS solenoid magnet	74
135	3.16 CMS Muon system schematic view	75
136	3.17 CMS Level-1 trigger architecture	77
137	3.18 WLCG structure	78
138	3.19 Detector data flow through hardware Tiers	81
139	4.1 The two leading-order diagrams of tHq production.	84
140	4.2 Input variables to the BDT for signal discrimination normalized.	94
141	4.3 Input variables to the BDT for signal discrimination not normalized.	96
142	4.4 BDT inputs as seen by TMVA against $t\bar{t}$	97

143	4.5	BDT inputs as seen by TMVA against $t\bar{t}V$	98
144	4.6	Correlation matrices for the input variables in the TMVA.	99
145	4.7	MVA classifiers performance.	99
146	4.8	Additional discriminating variables distributions.	101

¹⁴⁷ List of Tables

148	2.1	Fermions of the SM.	5
149	2.2	Fermion masses.	6
150	2.3	Leptons properties.	9
151	2.4	Quarks properties.	9
152	2.5	Fermion weak isospin and weak hypercharge multiplets.	11
153	2.6	Fundamental interactions features.	15
154	2.7	SM gauge bosons.	20
155	2.8	Higgs boson properties.	37
156	2.9	Predicted branching ratios for a SM Higgs boson with $m_H = 125 \text{ GeV}/c^2$	42
157	2.10	Predicted SM cross sections for tH production at $\sqrt{s} = 13 \text{ TeV}$	44
158	2.11	Predicted enhancement of the tHq and tHW cross sections at LHC	47
159	4.1	Signal samples and their cross section and branching fraction.	85
160	4.2	κ_V and κ_t combinations.	86
161	4.3	List of background samples used in this analysis (CMSSW 80X).	87
162	4.4	Leading-order $t\bar{t}W$ and $t\bar{t}Z$ samples used in the signal BDT training. . . .	87
163	4.5	Table of high-level triggers that we consider in the analysis.	88
164	4.6	Trigger efficiency scale factors and associated uncertainties.	89
165	4.7	Requirements on each of the three muon selections.	90

166	4.8 Criteria for each of the three electron selections.	91
167	4.9 MVA input discriminating variables	95
168	4.10 TMVA input variables ranking for BDTA_GRAD method	100
169	4.11 TMVA configuration used in the BDT training.	100
170	4.12 ROC-integral for all the testing cases.	102

¹⁷¹ Chapter 1

¹⁷² INTRODUCTION

Figure 1.1: ^{14}N neutron capture in a PECVD polymerized pyridine film. The Q-value of this reaction is 626 keV. Taken from [22]

¹⁷³ **Chapter 2**

¹⁷⁴ **Theoretical approach**

¹⁷⁵ **2.1 Introduction**

¹⁷⁶ The physical description of the universe is a challenge that physicists have faced by
¹⁷⁷ making theories that refine existing principles and proposing new ones in an attempt
¹⁷⁸ to embrace emerging facts and phenomena.

¹⁷⁹

¹⁸⁰ At the end of 1940s Julian Schwinger [11] and Richard P. Feynman [12], based in
¹⁸¹ the work of Sin-Itiro Tomonaga [13], developed an electromagnetic theory consistent
¹⁸² with special relativity and quantum mechanics that describes how matter and light
¹⁸³ interact; the so-called “quantum eletrodynamics” (QED) had born.

¹⁸⁴

¹⁸⁵ QED has become the guide in the development of theories that describe the universe.
¹⁸⁶ It was the first example of a quantum field theory (QFT), which is the theoretical
¹⁸⁷ framework for building quantum mechanical models that describes particles and their
¹⁸⁸ interactions. QFT is composed of a set of mathematical tools that combines classical
¹⁸⁹ fields, special relativity and quantum mechanics, while keeping the quantum point

190 particles and locality ideas.

191 This chapter gives an overview of the standard model of particle physics, starting
 192 with a description of the particles and interactions that compose it, followed by a
 193 description of the electroweak interaction, the Higgs boson and the associated pro-
 194 duction of Higgs boson and a single top quark (tH). The description contained in
 195 this chapter is based on references [1–3].

196 2.2 Standard model of particle physics

197 Particle physics at the fundamental level is modeled in terms of a collection of in-
 198 teracting particles and fields in a theory known as the “standard model of particle
 199 physics (SM)”¹.

200

201 The full picture of the SM is composed of three fields², whose excitations are inter-
 202 preted as particles called mediators or force-carriers; a set of fields, whose excitations
 203 are interpreted as elementary particles, interacting through the exchange of those
 204 mediators and a field that gives the mass to elementary particles. Figure 2.1 shows
 205 an scheme of the SM particles organization. In addition to the particles in the scheme
 206 (but not listed in it), their corresponding anti-particles, with opposite quantum num-
 207 bers, are also part of the picture; some particles are their own anti-particles, like
 208 photon or Higgs, or anti-particle is already listed like in the W^+ and W^- case.

209

210 The mathematical formulation of the SM is based on group theory and the use of

¹ The formal and complete treatment of the SM is out of the scope of this document, however a plenty of textbooks describing it at several levels are available in the literature. The treatment in “An Introduction To Quantum Field Theory (Frontiers in Physics)” by Michael E. Peskin and Dan V. Schroeder is quite comprehensive and detailed.

² Note that gravitational field is not included in the standard model formulation

Standard Model of Elementary Particles

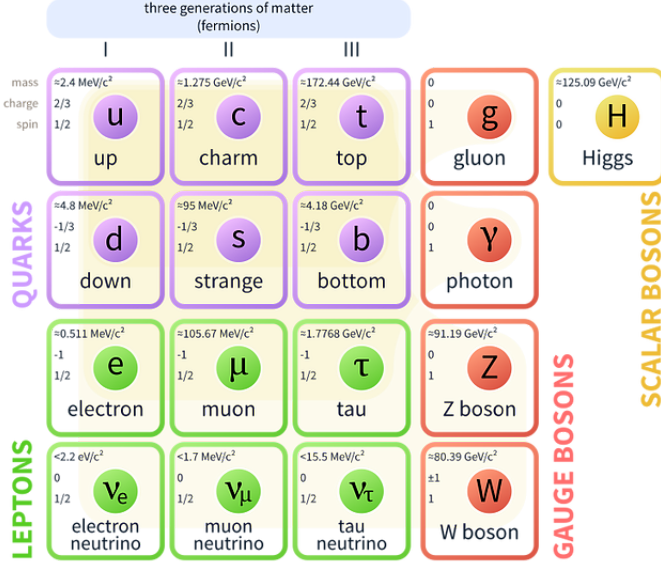


Figure 2.1: Schematic representation of the Standard model of particle physics. SM is a theoretical model intended to describe three of the four fundamental forces of the universe in terms of a set of particles and their interactions. [18].

211 Noether's theorem [17] which states that for a physical system modeled by a La-
 212 grangian that is invariant under a group of transformations a conservation law is
 213 expected. For instance, a system described by a time-independent Lagrangian is
 214 invariant (symmetric) under time changes (transformations) with the total energy
 215 conservation law as the expected conservation law. In QED, the charge operator
 216 (Q) is the generator of the $U(1)$ symmetry which according to the Noether's theorem
 217 means that there is a conserved quantity; this conserved quantity is the electric charge
 218 and thus the law conservation of electric charge is established.

219

220 In the SM, the symmetry group $SU(3)_C \otimes SU(2)_L \otimes U(1)_Y$ describes three of the
 221 four fundamental interactions in nature(see section 2.2.2): strong interaction(SI),
 222 weak interaction(WI) and electromagnetic interactions (EI) in terms of symmetries

223 associated to physical quantities:

224 • Strong: $SU(3)_C$ associated to color charge

225 • Weak: $SU(2)_L$ associated to weak isospin and chirality

226 • Electromagnetic: $U(1)_Y$ associated to weak hypercharge and electric charge

227 It will be shown that the electromagnetic and weak interactions are combined in
 228 the so-called electroweak interaction where chirality, hypercharge, weak isospin and
 229 electric charge are the central concepts.

230 **2.2.1 Fermions**

231 The basic constituents of the ordinary matter at the lowest level, which form the set
 232 of elementary particles in the SM formulation, are quarks and leptons. All of them
 233 have spin 1/2, therefore they are classified as fermions since they obey Fermi-Dirac
 234 statistics. There are six “flavors” of quarks and three of leptons organized in three
 235 generations, or families, as shown in table 2.1.

236

Generation				
	Type	1st	2nd	3rd
Leptons	Charged	Electron (e)	Moun(μ)	Tau (τ)
	Neutral	Electron neutrino (ν_e)	Muon neutrino (ν_μ)	Tau neutrino (ν_τ)
Quarks	Up-type	Up (u)	Charm (c)	Top (t)
	Down-type	Down (d)	Strange (s)	Bottom (b)

Table 2.1: Fermions of the SM. There are six flavors of quarks and three of leptons, organized in three generations, or families, composed of two pairs of closely related particles. The close relationship is motivated by the fact that WI between leptons is limited to the members of the same generation; WI between quarks is not limited but greatly favoured, to same generation members.

237

238 There is a mass hierarchy between generations (see table 2.2), where the higher gener-
 239 ation particles decays to the lower one, which can explain why the ordinary matter is
 240 made of particles in the first generation. In the SM, neutrinos are modeled as massless
 241 particles so they are not subject to this mass hierarchy; however, today it is known
 242 that neutrinos are massive so the hierarchy could be restated. The reason behind this
 243 mass hierarchy is one of the most important open questions in particle physics, and
 244 it becomes more puzzling when noticing that the mass difference between first and
 245 second generation fermions is small compared to the mass difference with respect to
 246 the third generation.

Lepton	Mass (MeV/c ²)	Quark	Mass (MeV/c ²)
e	0.51	u	2.2
μ	105.65	c	1.28×10^3
τ	1776.86	t	173.1×10^3
ν_e	Unknown	d	4.7
ν_μ	Unknown	s	96
τ_μ	Unknown	b	4.18×10^3

Table 2.2: Fermion masses [21]. Generations differ by mass in a way that have been interpreted as a masss hierarchy. Approximate values with no uncertainties are used, for comparison purpose.

247

248 Usually, the second and third generation fermions are produced in high energy pro-
 249 cesses, like the ones recreated in particle accelerators.

250 2.2.1.1 Leptons

251 A lepton is an elementary particle that is not subject to the SI. As seen in table 2.1,
 252 there are two types of leptons, the charged ones (electron, muon and tau) and the
 253 neutral ones (the three neutrinos). The electric charge (Q) is the property that gives
 254 leptons the ability to participate in the EI. From the classical point of view, Q plays

255 a central role determining, among others, the strength of the electric field through
256 which the electromagnetic force is exerted. It is clear that neutrinos are not affected
257 by EI because they don't carry electric charge.

258

259 Another feature of the leptons that is fundamental in the mathematical description
260 of the SM is the chirality, which is closely related to spin and helicity. Helicity defines
261 the handedness of a particle by relating its spin and momentum such that if they
262 are parallel then the particle is right-handed; if spin and momentum are antiparallel
263 the particle is said to be left-handed. The study of parity conservation (or viola-
264 tion) in β -decay has shown that only left-handed electrons/neutrinos or right-handed
265 positrons/anti-neutrinos are created [19]; the inclusion of that feature in the theory
266 was achieved by using projection operators for helicity, however, helicity is frame de-
267 pendent for massive particles which makes it not Lorentz invariant and then another
268 related attribute has to be used: *chirality*.

269

270 Chirality is a purely quantum attribute which makes it not so easy to describe in
271 graphical terms but it defines how the wave function of a particle transforms under
272 certain rotations. As with helicity, there are two chiral states, left-handed chiral (L)
273 and right-handed chiral (R). In the highly relativistic limit where $E \approx p \gg m$ helicity
274 and chirality converge, becoming exactly the same for massless particles.

275

276 In the following, when referring to left-handed (right-handed) it will mean left-handed
277 chiral (right-handed chiral). The fundamental fact about chirality is that while EI
278 and SI are not sensitive to chirality, in WI left-handed and right-handed fermions are
279 treated asymmetrically, such that only left handed fermions and right-handed anti-
280 fermions are allowed to couple to WI mediators, which is a violation of parity. The

way to translate this statement in a formal mathematical formulation is based on the
isospin symmetry group $SU(2)_L$.

283

284 Each generation of leptons is seen as a weak isospin doublet.³ The left-handed charged
285 lepton and its associated left-handed neutrino are arranged in doublets of weak isospin
286 $T=1/2$ while their right-handed partners are singlets:

$$\begin{pmatrix} \nu_l \\ l \end{pmatrix}_L, l_R := \begin{pmatrix} \nu_e \\ e \end{pmatrix}_L, \begin{pmatrix} \nu_\mu \\ \mu \end{pmatrix}_L, \begin{pmatrix} \nu_\tau \\ \tau \end{pmatrix}_L, e_R, \mu_R, \tau_R, \nu_{eR}, \nu_{\mu R}, \nu_{\tau R} \quad (2.1)$$

287 The isospin third component refers to the eigenvalues of the weak isospin operator
288 which for doublets is $T_3 = \pm 1/2$, while for singlets it is $T_3 = 0$. The physical meaning
289 of this doublet-singlet arrangement falls in that the WI couples the two particles in
290 the doublet by exchanging the interaction mediator while the singlet member is not
291 involved in WI. The main properties of the leptons are summarized in table 2.3.

292

293 Altough all three flavor neutrinos have been observed, their masses remain unknown
294 and only some estimations have been made [20]. The main reason is that the fla-
295 vor eigenstates are not the same as the mass eigenstates which implies that when
296 a neutrino is created its mass state is a linear combination of the three mass eigen-
297 states and experiments can only probe the squared difference of the masses. The
298 Pontecorvo-Maki-Nakagawa-Sakata (PMNS) mixing matrix encode the relationship
299 between flavor and mass eigenstates.

300

³ The weak isospin is an analogy of the isospin symmetry in strong interaction where neutron and proton are affected equally by strong force but differ in their charge.

Lepton	Q(e)	T_3	L_e	L_μ	L_τ	Lifetime (s)
Electron (e)	-1	-1/2	1	0	0	Stable
Electron neutrino(ν_e)	0	1/2	1	0	0	Unknown
Muon (μ)	-1	-1/2	0	1	0	2.19×10^{-6}
Muon neutrino (ν_μ)	0	1/2	0	1	0	Unknown
Tau (τ)	-1	-1/2	0	0	1	290.3×10^{-15}
Tau neutrino (τ_μ)	0	1/2	0	0	1	Unknown

Table 2.3: Leptons properties [21]. Q: electric charge, T_3 : weak isospin. Only left-handed leptons and right-handed anti-leptons participate in the WI. Anti-particles with inverted T_3 , Q and lepton number complete the leptons set but are not listed. Right-handed leptons and left-handed anti-leptons, neither listed, form weak isospin singlets with $T_3 = 0$ and do not take part in the weak interaction.

301 2.2.1.2 Quarks

302 Quarks are the basic constituents of protons and neutrons. The way quarks join to
 303 form bound states, called “hadrons”, is through the SI. Quarks are affected by all the
 304 fundamental interactions which means that they carry all the four types of charges:
 305 color, electric charge, weak isospin and mass.

Flavor	Q(e)	I_3	T_3	B	C	S	T	B'	Y	Color
Up (u)	2/3	1/2	1/2	1/3	0	0	0	0	1/3	r,b,g
Charm (c)	2/3	0	1/2	1/3	1	0	0	0	4/3	r,b,g
Top(t)	2/3	0	1/2	1/3	0	0	1	0	4/3	r,b,g
Down(d)	-1/3	-1/2	-1/2	1/3	0	0	0	0	1/3	r,b,g
Strange(s)	-1/3	0	-1/2	1/3	0	-1	0	0	-2/3	r,b,g
Bottom(b)	-1/3	0	-1/2	1/3	0	0	0	-1	-2/3	r,b,g

Table 2.4: Quarks properties [21]. Q: electric charge, I_3 : isospin, T_3 : weak isospin, B: baryon number, C: charmness, S: strangeness, T: topness, B' : bottomness, Y: hypercharge. Anti-quarks posses the same mass and spin as quarks but all charges (color, flavor numbers) have opposite sign.

306

307 Table 2.4 summarizes the features of quarks, among which the most particular is
 308 their fractional electric charge. Note that fractional charge is not a problem, given
 309 that quarks are not found isolated, but serves to explain how composed particles are

310 formed out of two or more valence quarks⁴.

311

312 Color charge is the responsible for the SI between quarks and is the symmetry
 313 ($SU(3)_C$) that defines the formalism to describe SI. There are three colors: red (r),
 314 blue(b) and green(g) and their corresponding three anti-colors; thus each quark carries
 315 one color unit while anti-quarks carries one anti-color unit. As said above, quarks are
 316 not allowed to be isolated due to the color confinement effect, therefore their features
 317 have been studied indirectly by observing their bound states created when:

318 • one quark with a color charge is attracted by an anti-quark with the correspond-
 319 ing anti-color charge forming a colorless particle called a “meson.”

320 • three quarks (anti-quarks) with different color (anti-color) charges are attracted
 321 among them forming a colorless particle called a “baryon(anti-baryon).”

322 In the first version of the quark model (1964), M. Gell-Mann [22] and G. Zweig
 323 [23,24] developed a consistent way to classify hadrons according to their properties.
 324 Only three quarks (u, d, s) were involved in a scheme in which all baryons have
 325 baryon number $B=1$ and therefore quarks have $B=1/3$; non-baryons have $B=0$. The
 326 scheme organizes baryons in a two-dimensional space ($I_3 - Y$); Y (hypercharge) and I_3
 327 (isospin) are quantum numbers related by the Gell-Mann-Nishijima formula [25, 26]:

$$Q = I_3 + \frac{Y}{2} \quad (2.2)$$

328 where $Y = B + S + C + T + B'$ are the quantum numbers listed in table 2.4. Baryon
 329 number is conserved in SI and EI which means that single quarks cannot be created

⁴ Hadrons can contain an indefinite number of virtual quarks and gluons, known as the quark and gluon sea, but only the valence quarks determine hadrons' quantum numbers.

330 but in pairs $q - \bar{q}$.

331

332 There are six quark flavors organized in three generations (see table 2.1) following a
 333 mass hierarchy which, again, implies that higher generations decay to first generation
 334 quarks.

	Quarks			T_3	Y_W	Leptons			T_3	Y_W
Doublets	$(\frac{u}{d'})_L$	$(\frac{c}{s'})_L$	$(\frac{t}{b'})_L$	$(\frac{1/2}{-1/2})$	1/3	$(\frac{\nu_e}{e})_L$	$(\frac{\nu_\mu}{\mu})_L$	$(\frac{\nu_\tau}{\tau})_L$	$(\frac{1/2}{-1/2})$	-1
Singlets	u_R	c_R	t_R	0	4/3	ν_{eR}	$\nu_{\mu R}$	$\nu_{\tau R}$	0	-2

Table 2.5: Fermion weak isospin and weak hypercharge multiplets. Weak hypercharge is calculated through the Gell-Mann-Nishijima formula 2.2 but using the weak isospin and charge for quarks.

335

336 Isospin doublets of quarks are also defined (see table 2.5) and as for neutrinos, the
 337 mass eigenstates are not the same as the WI eigenstates which means that members of
 338 different quark generations are connected by the WI mediator; thus, up-type quarks
 339 are coupled not to down-type quarks directly but to a superposition of down-type
 340 quarks (q'_d) via WI according to:

341

$$\begin{pmatrix} q'_d \\ s' \\ b' \end{pmatrix} = \begin{pmatrix} V_{ud} & V_{us} & V_{ub} \\ V_{cd} & V_{cs} & V_{cb} \\ V_{td} & V_{ts} & V_{tb} \end{pmatrix} \begin{pmatrix} d \\ s \\ b \end{pmatrix} \quad (2.3)$$

342 where V_{CKM} is known as Cabibbo-Kobayashi-Maskawa (CKM) mixing matrix [27,28].
 343 The weak decays of quarks are represented in the diagram of figure 2.2; again the
 344 CKM matrix plays a central role since it contains the probabilities for the different

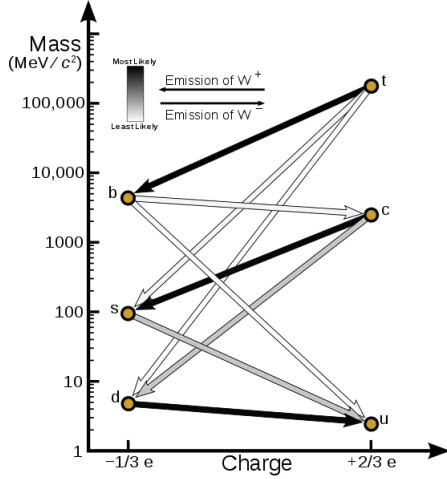


Figure 2.2: Transformations between quarks through WI. Higher generations quarks decay to first generation quarks by emitting a W boson. The arrow color indicates the likelihood of the transition according to the grey scale in the top left side which represent the CKM matrix parameters [29].

345 quark decay channels, in particular, note that quark decays are greatly favored be-
 346 tween generation members.

347

348 CKM matrix is a 3×3 unitary matrix parametrized by three mixing angles and
 349 the *CP-mixing phase*; the latter is the parameter responsible for the Charge-Parity
 350 symmetry violation (CP-violation) in the SM. The fact that the b quark decays almost
 351 all the times to a top quark is exploited in this thesis when making the selection of
 352 the signal events by requiring the presence of a jet tagged as a jet coming from a
 353 b quark in the final state. The effect of the *CP-mixing phase* on the cross section of
 354 associated production of Higgs boson and a single top process is also explored in this
 355 thesis.

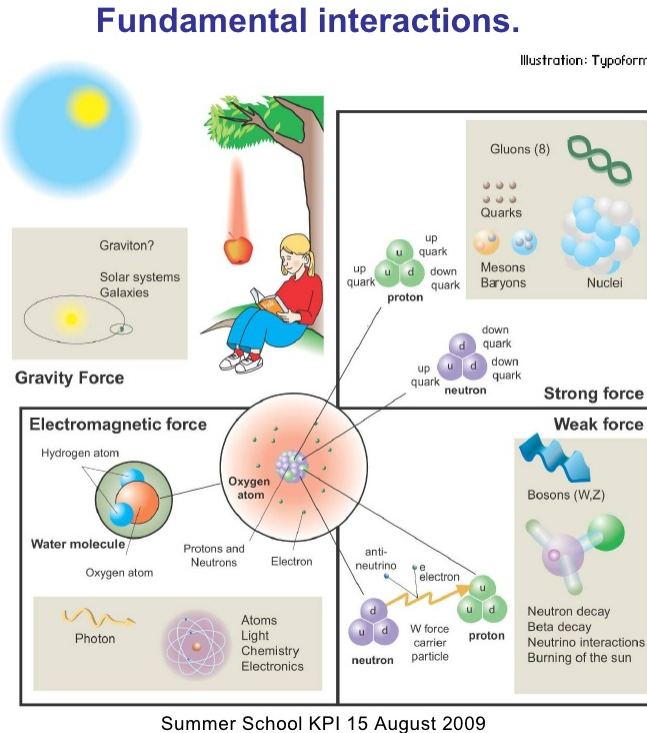


Figure 2.3: Fundamental interactions in nature. Despite the many manifestations of forces in nature, we can track all of them back to one of the fundamental interactions. The most common forces are gravity and electromagnetic given that all of us are subject and experience them in everyday life.

356 2.2.2 Fundamental interactions

357 Even though there are many manifestations of force in nature, like the ones represented in figure 2.3, we can classify all of them into one of four fundamental interactions:

- 360 • *Electromagnetic interaction (EI)* affects particles that are “electrically charged,”
 361 like electrons and protons. It is described by QED combining quantum mechanics,
 362 special relativity and electromagnetism in order to explain how particles
 363 with electric charge interact through the exchange of photons, therefore, one
 364 says that “Electromagnetic Force” is mediated by “photons”. Figure 2.4a. shows
 365 a graphical representation, known as “feynman diagram”, of electron-electron

366 scattering.

- 367 • *Strong interaction (SI)* described by Quantum Chromodynamics (QCD). Hadrons
 368 like proton and neutron have internal structure given that they are composed
 369 of two or more valence quarks⁵. Quarks have fractional electric charge which
 370 means that they are subject to electromagnetic interaction and in the case of the
 371 proton they should break apart due to electrostatic repulsion; however, quarks
 372 are held together inside the hadrons against their electrostatic repulsion by the
 373 “Strong Force” through the exchange of “gluons.” The analog to the electric
 374 charge is the “color charge”. Electrons and photons are elementary particles
 375 as quarks but they don’t carry color charge, therefore they are not subject to
 376 SI. The feynman diagram for gluon exchange between quarks is shown in figure
 377 2.4b.

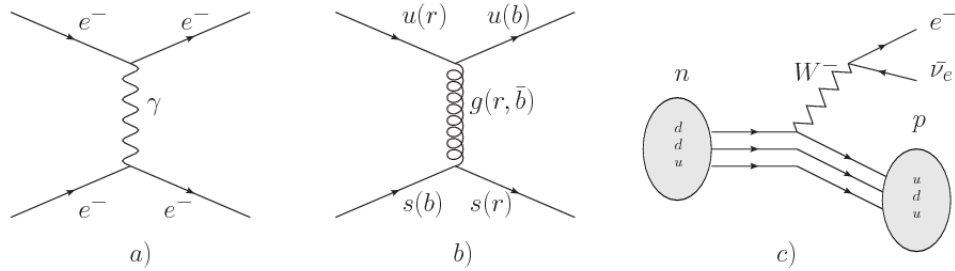


Figure 2.4: Feynman diagrams representing the interactions in SM; a) EI: e - e scattering; b) SI: gluon exchange between quarks ; c) WI: β -decay

- 378 • *Weak interaction (WI)* described by the weak theory (WT), is responsible, for
 379 instance, for the radioactive decay in atoms and proton-proton (pp) fusion
 380 within the sun. Quarks and leptons are the particles affected by the weak
 381 interaction; they possess a property called “flavor charge” (see 2.2.1) which can
 382 be changed by emitting or absorbing one weak force mediator. There are three
 383 mediators of the “weak force” known as “Z” boson in the case of electrically

⁵ particles made of four and five quarks are exotic states not so common.

384 neutral changes and “ W^\pm ” bosons in the case of electrically charged changes.
 385 The “weak isospin” is the WI analog to electric charge in EI, and color charge
 386 in SI, and defines how quarks and leptons are affected by the weak force. Figure
 387 2.4c. shows the feynman diagram of β -decay where a newtron (n) is transformed
 388 in a proton (p) by emmiting a W^- particle. Since this thesis is in the frame
 389 of the electroweak interaction, a more detailed description of it will be given in
 390 section 2.3

391 • *Gravitational interaction (GI)* described by General Theory of Relativity (GR).
 392 It is responsible for the structure of galaxies and black holes as well as the
 393 expansion of the universe. As a classical theory, in the sense that it can be for-
 394 mulated without even appeal to the concept of quantization, it implies that the
 395 spacetime is a continuum and predictions can be made without limitation to the
 396 precision of the measurement tools. The latter represent a direct contradiction
 397 of the quantum mechanics principles. Gravity is deterministic while quantum
 398 mechanics is probabilistic; despite that, efforts to develop a quantum theory of
 399 gravity have predicted the “graviton” as mediator of the Gravitational force⁶.

Interaction	Acts on	Relative strength	Range (m)	Mediators
Electromagnetic (QED)	Electrically charged particles	10^{-2}	Infinite	Photon
Strong (QCD)	Quarks and gluons	1	10^{-15}	Gluon
Weak (WI)	Leptons and quarks	10^{-6}	10^{-18}	W^\pm , Z
Gravitational (GI)	Massive particles	10^{-39}	Infinite	Graviton

Table 2.6: Fundamental interactions features [30].

400

401 Table 2.6 sumarizes the main features of the fundamental interactions. The rela-
 402 tive strength of the fundamental forces reveals the meaning of strong and weak; in

⁶ Actually a wide variety of theories have been developed in an attempt to describe gravity; some famous examples are string theory and supergravity.

403 a context where the relative strength of the SI is 1, the EI is about hundred times
 404 weaker and WI is about million times weaker than the SI. A good description on
 405 how the relative strength and range of the fundamental interactions are calculated
 406 can be found in references [30, 31]. In the everyday life, only EI and GI are explicitly
 407 experienced due to the range of these interactions; i.e., at the human scale distances
 408 only EI and GI have appreciable effects, in contrast to SI which at distances greater
 409 than 10^{-15} m become negligible.

410

411 QED was built successfully on the basis of the classical electrodynamics theory (CED)
 412 of Maxwell and Lorentz, following theoretical and experimental requirements imposed
 413 by

- 414 • lorentz invariance: independence on the reference frame.
- 415 • locallity: interacting fields are evaluated at the same space-time point to avoid
 416 action at a distance.
- 417 • renormalizability: physical predictions are finite and well defined
- 418 • particle spectrum, symmetries and conservation laws already known must emerge
 419 from the theory.
- 420 • gauge invariance.

421 The gauge invariance requirement reflects the fact that the fundamental fields cannot
 422 be directly measured but associated fields which are the observables. Electric (“**E**”)
 423 and magnetic (“**B**”) fields in CED are associated with the electric scalar potential
 424 “**V**” and the vector potential “**A**”. In particular, **E** can be obtained by measuring
 425 the change in the space of the scalar potential (ΔV); however, two scalar potentials

426 differing by a constant “f” correspond to the same electric field. The same happens in
 427 the case of the vector potential “ \mathbf{A} ”; thus, different configurations of the associated
 428 fields result in the same set of values of the observables. The freedom in choosing
 429 one particular configuration is known as “gauge freedom”; the transformation law con-
 430 necting two configurations is known as “gauge transformation” and the fact that the
 431 observables are not affected by a gauge transformation is called “gauge invariance”.

432

433 When the gauge transformation:

$$\begin{aligned} \mathbf{A} &\rightarrow \mathbf{A} - \Delta f \\ V &\rightarrow V - \frac{\partial f}{\partial t} \end{aligned} \tag{2.4}$$

434 is applied to Maxwell equations, they are still satisfied and the fields remain invariant.
 435 Thus, CED is invariant under gauge transformations and is called a “gauge theory”.
 436 The set of all gauge transformations form the “symmetry group” of the theory, which
 437 according to the group theory, has a set of “group generators”. The number of group
 438 generators determine the number of “gauge fields” of the theory.

439

440 As mentioned in the first lines of section 2.2, QED has one symmetry group ($U(1)$)
 441 with one group generator (the Q operator) and one gauge field (the electromagnetic
 442 field A^μ). In CED there is not a clear definition, beyond the historical convention, of
 443 which fields are the fundamental and which are the associated, but in QED it is clear
 444 that the fundamental field is A^μ . When a gauge theory is quantized, the gauge field
 445 is quantized and its quanta is called “gauge boson”. The word boson characterizes
 446 particles with integer spin which obey Bose-Einstein statistics.

447

448 As will be detailed in section 2.3, interactions between particles in a system can be
 449 obtained by considering first the Lagrangian density of free particles in the system,
 450 which of course is incomplete because the interaction terms have been left out, and
 451 demanding global phase transformation invariance. Global phase transformation in-
 452 variance means that a gauge transformation is performed identically to every point
 453 in the space⁷ and the Lagrangian remains invariant. Then, the global transformation
 454 is promoted to a local phase transformation (this time the gauge transformation de-
 455 pends on the position in space) and again invariance is required.

456

457 Due to the space dependence of the local transformation, the Lagrangian density is
 458 not invariant anymore. In order to restate the gauge invariance, the gauge covariant
 459 derivative is introduced in the Lagrangian and with it the gauge field responsible for
 460 the interaction between particles in the system. The new Lagrangian density is gauge
 461 invariant, includes the interaction terms needed to account for the interactions and
 462 provides a way to explain the interaction between particles through the exchange of
 463 the gauge boson.

464 This recipe was used to build QED and the theories that aim to explain the funda-
 465 mental interactions.

466 2.2.3 Gauge Bosons

467 The importance of the gauge bosons comes from the fact that they are the force
 468 mediators or force carriers. The features of the gauge bosons reflect those of the
 469 fields they represent and they are extracted from the Lagrangian density used to
 470 describe the interactions. In section 2.3, it will be shown how the gauge bosons of the

⁷ Here space corresponds to the 4-dimensional space i.e. space-time.

471 EI and WI emerge from the electroweak Lagrangian. The SI gauge bosons features
 472 are also extracted from the SI Lagrangian but it is not detailed in this document. The
 473 main features of the SM gauge bosons will be briefly presented below and summarized
 474 in table 2.7.

475 • **Photon.** EI occurs when the photon couples to (is exchanged between) particles
 476 carrying electric charge; however, the photon itself does not carry electric charge,
 477 therefore, there is no coupling between photons. Given that the photon is
 478 massless the EI is of infinite range, i.e., electrically charged particles interact
 479 even if they are located far away one from each other; this also implies that
 480 photons always move with the speed of light.

481 • **Gluon.** SI is mediated by gluons which, same as photons, are massless. They
 482 carry one unit of color charge and one unit of anticolor charge which means that
 483 gluons couple to other gluons. As a result, the range of the SI is not infinite
 484 but very short due to the attraction between gluons, giving rise to the “color
 485 confinement” which explains why color charged particles cannot be isolated but
 486 live within composited particles, like quarks inside protons.

487 • **W, Z.** The WI mediators, W^\pm and Z, are massive which explains their short-
 488 range. Given that the WI is the only interaction that can change the flavor
 489 of the interacting particles, the W boson is the responsible for the nuclear
 490 transmutation where a neutron is converted in a proton or vice versa with the
 491 involvement of an electron and a neutrino (see figure 2.4c). The Z boson is the
 492 responsible of the neutral weak processes like neutrino elastic scattering where
 493 no electric charge but momentum transference is involved. WI gauge bosons
 494 carry isospin charge which makes possible the interaction between them.

Interaction	Mediator	Electric charge (e)	Color charge	Weak Isospin	mass (GeV/c ²)
Electromagnetic	Photon (γ)	0	No	0	0
Strong	Gluon (g)	0	Yes -octet	No	0
Weak	W^\pm	± 1	No	± 1	80.385 ± 0.015
	Z	0	No	0	91.188 ± 0.002

Table 2.7: SM gauge bosons main features [21].

495

496 **2.3 Electroweak unification and the Higgs
497 mechanism**

498 Physicists dream of building a theory that contains all the interactions in one single
499 interaction, i.e., showing that at some scale in energy all the four fundamental in-
500 teractions are unified and only one interaction emerges in a “Theory of everything”.
501 The first sign of the feasibility of such unification comes from success in the con-
502 struction of the CED. Einstein spent years trying to reach that dream, which by
503 1920 only involved electromagnetism and gravity, with no success; however, a new
504 partial unification was achieved in the 1960’s, when S.Glashow [14], A.Salam [15] and
505 S.Weinberg [16] independently proposed that electromagnetic and weak interactions
506 are two manifestations of a more general interaction called “electroweak interaction
507 (EWT)”. Both, QCD and EWT, were developed in parallel and following the useful
508 prescription provided by QED and the gauge invariance principles.

509

510 The theory of weak interactions was capable of explaining the β -decay and in general
511 the processes mediated by W^\pm bosons. However, there were some processes like the
512 “ $\nu_\mu - e$ scattering” which would require the exchange of two W bosons (see figure 2.5
513 top diagrams) giving rise to divergent loop integrals and then non finite predictions.

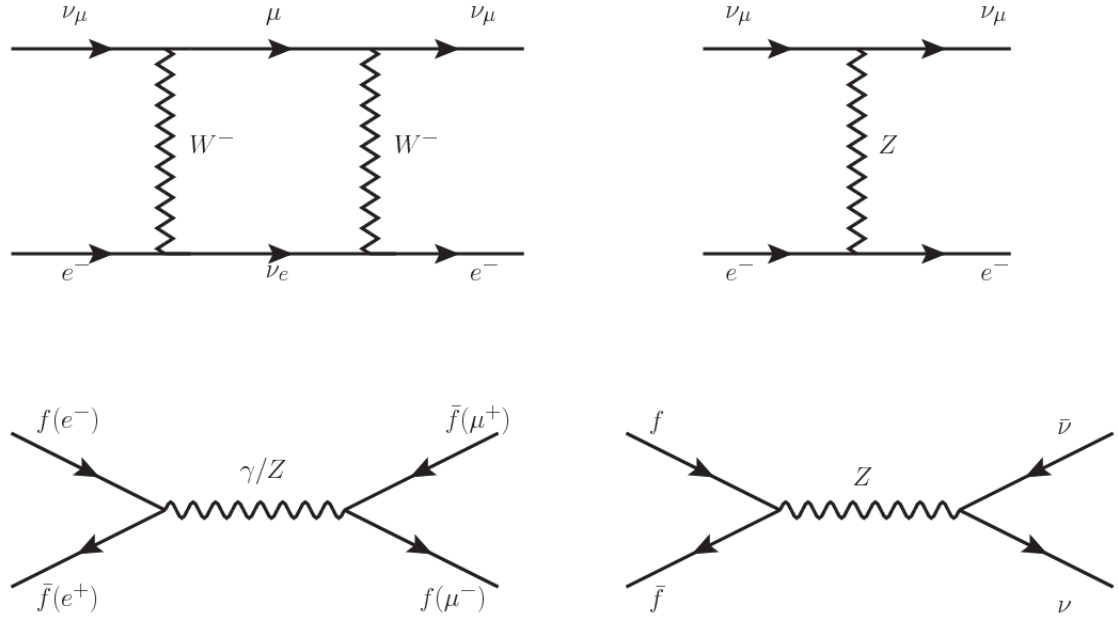


Figure 2.5: Top: $\nu_\mu - e^-$ scattering going through charged currents (left) and neutral currents (right). Bottom: neutral current processes for charged fermions (left) and involving neutrinos (right). While neutral current processes involving only charged fermions can proceed through EI or WI, those involving neutrinos can only proceed via WI.

514 By including neutral currents involving fermions via the exchange of neutral bosons
 515 Z , those divergences are compensated and the predictions become realistic.

516

517 Neutral weak interaction vertices conserve flavor in the same way as the electromag-
 518 netic vertices do, but additionally, the Z boson can couple to neutrinos which implies
 519 that processes involving charged fermions can proceed through EI or WI but processes
 520 involving neutrinos can proceed only through WI.

521

522 The prescription to build a gauge theory of the WI consists of proposing a free field
 523 Lagrangian density that includes the particles involved; next, by requesting invari-
 524 ance under global phase transformations first and generalizing to local phase trans-
 525 formations invariance later, the conserved currents are identified and interactions are

526 generated by introducing gauge fields. Given that the goal is to include the EI and
 527 WI in a single theory, the group symmetry considered should be a combination of
 528 $SU(2)_L$ and $U(1)_{em}$, however the latter cannot be used directly because the EI treats
 529 left and right-handed particles indistinctly in contrast to the former. Fortunately, the
 530 weak hypercharge, which is a combination of the weak isospin and the electric charge
 531 (eqn 2.2) is suitable to be used since it is conserved by the EI and WI. Thus, the
 532 symmetry group to be considered is

$$G \equiv SU(2)_L \otimes U(1)_Y \quad (2.5)$$

533 The following treatment applies to any of the fermion generations, but for simplicity
 534 the first generation of leptons will be considered [2, 3, 32, 33].

535

536 Given the first generation of leptons

$$\psi_1 = \begin{pmatrix} \nu_e \\ e^- \end{pmatrix}_L, \quad \psi_2 = \nu_{eR}, \quad \psi_3 = e_R^- \quad (2.6)$$

537 the charged fermionic currents are given by

$$J_\mu \equiv J_\mu^+ = \bar{\nu}_{eL} \gamma_\mu e_L, \quad J_\mu^\dagger \equiv J_\mu^- = \bar{e}_L \gamma_\mu \nu_{eL} \quad (2.7)$$

538 and the free Lagrangian is given by

$$\mathcal{L}_0 = \sum_{j=1}^3 i\bar{\psi}_j(x) \gamma^\mu \partial_\mu \psi_j(x). \quad (2.8)$$

539 Mass terms are included directly in the QED and QCD free Lagrangians since they
 540 preserve the invariance under the symmetry transformations involved which treat
 541 left-handed and right-handed similarly, however mass terms of the form

$$m_W^2 W_\mu^\dagger(x) W^\mu(x) + \frac{1}{2} m_Z^2 Z_\mu(x) Z^\mu(x) - m_e \bar{\psi}_e(x) \psi_e(x) \quad (2.9)$$

542 which represent the mass of W^\pm , Z and electrons, are not invariant under G trans-
 543 formations, therefore the gauge fields described by the EWI are in principle massless.

544

545 Experiments have shown that the gauge fields are not massless; however, they have
 546 to acquire mass through a mechanism compatible with the gauge invariance; that
 547 mechanism is known as the “Higgs mechanism” and will be considered later in this
 548 section. The global transformations in the combined symmetry group G can be
 549 written as

$$\begin{aligned} \psi_1(x) &\xrightarrow{G} \psi'_1(x) \equiv U_Y U_L \psi_1(x), \\ \psi_2(x) &\xrightarrow{G} \psi'_2(x) \equiv U_Y \psi_2(x), \\ \psi_3(x) &\xrightarrow{G} \psi'_3(x) \equiv U_Y \psi_3(x) \end{aligned} \quad (2.10)$$

550 where U_L represent the $SU(2)_L$ transformation acting only on the weak isospin dou-
 551 blet and U_Y represent the $U(1)_Y$ transformation acting on all the weak isospin mul-
 552 tiplets. Explicitly

$$U_L \equiv \exp\left(i \frac{\sigma_i}{2} \alpha^i\right), \quad U_Y \equiv \exp(i y_i \beta) \quad (i = 1, 2, 3) \quad (2.11)$$

553 with σ_i the Pauli matrices and y_i the weak hypercharges. In order to promote the
 554 transformations from global to local while keeping the invariance, it is required that
 555 $\alpha^i = \alpha^i(x)$, $\beta = \beta(x)$ and the replacement of the ordinary derivatives by the covariant
 556 derivatives

$$\begin{aligned}
D_\mu \psi_1(x) &\equiv \left[\partial_\mu + ig\sigma_i W_\mu^i(x)/2 + ig'y_1 B_\mu(x) \right] \psi_1(x) \\
D_\mu \psi_2(x) &\equiv \left[\partial_\mu + ig'y_2 B_\mu(x) \right] \psi_2(x) \\
D_\mu \psi_3(x) &\equiv \left[\partial_\mu + ig'y_3 B_\mu(x) \right] \psi_3(x)
\end{aligned} \tag{2.12}$$

557 introducing in this way four gauge fields, $W_\mu^i(x)$ and $B_\mu(x)$, in the process. The
558 covariant derivatives (eqn 2.12) are required to transform in the same way as fermion
559 fields $\psi_i(x)$ themselves, therefore, the gauge fields transform as:

$$\begin{aligned}
B_\mu(x) &\xrightarrow{G} B'_\mu(x) \equiv B_\mu(x) - \frac{1}{g'} \partial_\mu \beta(x) \\
W_\mu^i(x) &\xrightarrow{G} W_\mu^{i'}(x) \equiv W_\mu^i(x) - \frac{i}{g} \partial_\mu \alpha_i(x) - \varepsilon_{ijk} \alpha_i(x) W_\mu^j(x).
\end{aligned} \tag{2.13}$$

560 The G invariant version of the Lagrangian density 2.8 can be written as

$$\mathcal{L}_0 = \sum_{j=1}^3 i\bar{\psi}_j(x) \gamma^\mu D_\mu \psi_j(x) \tag{2.14}$$

561 where free massless fermion and gauge fields and fermion-gauge boson interactions
562 are included. The EWI Lagrangian density must additionally include kinetic terms
563 for the gauge fields (\mathcal{L}_G) which are built from the field strengths, according to

$$B_{\mu\nu}(x) \equiv \partial_\mu B_\nu - \partial_\nu B_\mu \tag{2.15}$$

$$W_{\mu\nu}^i(x) \equiv \partial_\mu W_\nu^i(x) - \partial_\nu W_\mu^i(x) - g\varepsilon^{ijk} W_\mu^j W_\nu^k \tag{2.16}$$

564 the last term in eqn. 2.16 is added in order to hold the gauge invariance; therefore,

$$\mathcal{L}_G = -\frac{1}{4}B_{\mu\nu}(x)B^{\mu\nu}(x) - \frac{1}{4}W_{\mu\nu}^i(x)W_i^{\mu\nu}(x) \quad (2.17)$$

565 which contains not only the free gauge fields contributions, but also the gauge fields
 566 self-interactions and interactions among them.

567

568 The three weak isospin conserved currents resulting from the $SU(2)_L$ symmetry are
 569 given by

$$J_\mu^i(x) = \frac{1}{2}\bar{\psi}_1(x)\gamma_\mu\sigma^i\psi_1(x) \quad (2.18)$$

570 while the weak hypercharge conserved current resulting from the $U(1)_Y$ symmetry is
 571 given by

$$J_\mu^Y = \sum_{j=1}^3 \bar{\psi}_j(x)\gamma_\mu y_j \psi_j(x) \quad (2.19)$$

572 In order to evaluate the electroweak interactions modeled by an isos triplet field W_μ^i
 573 which couples to isospin currents J_μ^i with strength g and additionally the singlet
 574 field B_μ which couples to the weak hypercharge current J_μ^Y with strength $g'/2$. The
 575 interaction Lagrangian density to be considered is

$$\mathcal{L}_I = -g J^{i\mu}(x) W_\mu^i(x) - \frac{g'}{2} J^{Y\mu}(x) B_\mu(x) \quad (2.20)$$

576 Note that the weak isospin currents are not the same as the charged fermionic currents
 577 that were used to describe the WI (eqn 2.7), since the weak isospin eigenstates are
 578 not the same as the mass eigenstates, but they are closely related

$$J_\mu = \frac{1}{2}(J_\mu^1 + iJ_\mu^2), \quad J_\mu^\dagger = \frac{1}{2}(J_\mu^1 - iJ_\mu^2). \quad (2.21)$$

579 The same happens with the gauge fields W_μ^i which are related to the mass eigenstates
 580 W^\pm by

$$W_\mu^+ = \frac{1}{\sqrt{2}}(W_\mu^1 - iW_\mu^2), \quad W_\mu^- = \frac{1}{\sqrt{2}}(W_\mu^1 + iW_\mu^2). \quad (2.22)$$

581 The fact that there are three weak isospin conserved currents is an indication that in
 582 addition to the charged fermionic currents, which couple charged to neutral leptons,
 583 there should be a neutral fermionic current that does not involve electric charge
 584 exchange; therefore, it couples neutral fermions or fermions of the same electric charge.
 585 The third weak isospin current contains a term that is similar to the electromagnetic
 586 current (j_μ^{em}), indicating that there is a relation between them and resembling the
 587 Gell-Mann-Nishijima formula 2.2 adapted to electroweak interactions

$$Q = T_3 + \frac{Y_W}{2}. \quad (2.23)$$

588 Just as Q generates the $U(1)_{em}$ symmetry, the weak hypercharge generates the $U(1)_Y$
 589 symmetry as said before. It is possible to write the relationship in terms of the currents
 590 as

$$j_\mu^{em} = J_\mu^3 + \frac{1}{2}J_\mu^Y. \quad (2.24)$$

591 The neutral gauge fields W_μ^3 and B_μ cannot be directly identified with the Z and the
 592 photon fields since the photon interacts similarly with left and right-handed fermions;
 593 however, they are related through a linear combination given by

$$A_\mu = B_\mu \cos \theta_W + W_\mu^3 \sin \theta_W \quad (2.25)$$

$$Z_\mu = -B_\mu \sin \theta_W + W_\mu^3 \cos \theta_W$$

594 where θ_W is known as the “Weinberg angle.” The interaction Lagrangian is now given

595 by

$$\mathcal{L}_I = -\frac{g}{\sqrt{2}}(J^\mu W_\mu^+ + J^{\mu\dagger} W_\mu^-) - \left(g \sin \theta_W J_\mu^3 + g' \cos \theta_W \frac{J_\mu^Y}{2}\right) A^\mu - \left(g \cos \theta_W J_\mu^3 - g' \sin \theta_W \frac{J_\mu^Y}{2}\right) Z^\mu \quad (2.26)$$

596 the first term is the weak charged current interaction, while the second term is the

597 electromagnetic interaction under the condition

$$g \sin \theta_W = g' \cos \theta_W = e, \quad \frac{g'}{g} = \tan \theta_W \quad (2.27)$$

598 contained in the eqn.2.24; the third term is the neutral weak current.

599

600 Note that the neutral fields transformation given by the eqn. 2.25 can be written in

601 terms of the coupling constants g and g' as:

$$A_\mu = \frac{g' W_\mu^3 + g B_\mu}{\sqrt{g^2 + g'^2}}, \quad Z_\mu = \frac{g W_\mu^3 - g' B_\mu}{\sqrt{g^2 + g'^2}} \quad (2.28)$$

602 So far, the Lagrangian density describing the non-massive EWI is:

$$\mathcal{L}_{nmEWI} = \mathcal{L}_0 + \mathcal{L}_G \quad (2.29)$$

603 where fermion and gauge fields have been considered massless because their regular

604 mass terms are manifestly non invariant under G transformations; therefore, masses

605 have to be generated in a gauge invariant way. The mechanism by which this goal is
 606 achieved is known as the “Higgs mechanism” and is closely connected to the concept
 607 of “spontaneous symmetry breaking.”

608 2.3.1 Spontaneous symmetry breaking (SSB)

609 Figure 2.6 left shows a steel nail (top) which is subject to an external force; the form
 610 of the potential energy is also shown (bottom).

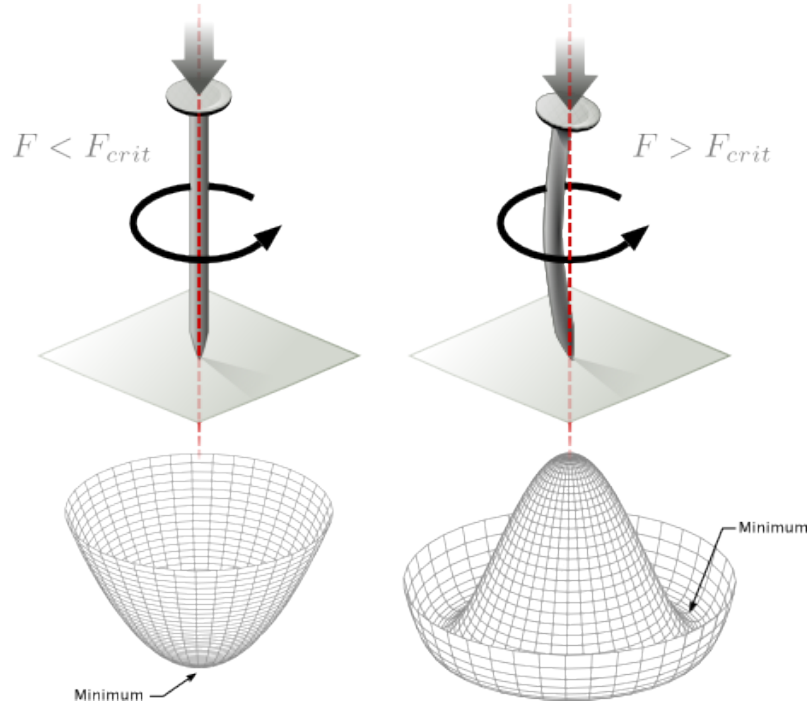


Figure 2.6: Spontaneous symmetry breaking mechanism. The steel nail, subject to an external force (top left), has rotational symmetry with respect to its axis. When the external force overcomes a critical value the nail buckles (top right) choosing a minimal energy state (ground state) and thus “*breaking spontaneously the rotational symmetry*”. The potential energy (bottom) changes but holds the rotational symmetry; however, an infinite number of asymmetric ground states are generated and circularly distributed in the bottom of the potential [34].

612 Before reaching the critical force value, the system has rotational symmetry with re-
 613 spect to the nail axis; however, after the critical force value is reached the nail buckles
 614 (top right). The form of the potential energy (bottom right) changes, preserving its
 615 rotational symmetry although its minima does not exhibit that rotational symmetry
 616 any longer. Right before the nail buckles there is no indication of the direction the
 617 nail will bend because any of the directions are equivalent, but once the nail bends,
 618 choosing a direction, an arbitrary minimal energy state (ground state) is selected and
 619 it does not share the system's rotational symmetry. This mechanism for reaching an
 620 asymmetric ground state is known as "*spontaneous symmetry breaking*".
 621 The lesson from this analysis is that the way to introduce the SSB mechanism into a
 622 system is by adding the appropriate potential to it.

623

624 Figure 2.7 shows a plot of the potential $V(\phi)$ in the case of a scalar field ϕ

$$V(\phi) = \mu^2 \phi^\dagger \phi + \lambda (\phi^\dagger \phi)^2 \quad (2.30)$$

625 If $\mu^2 > 0$ the potential has only one minimum at $\phi = 0$ and describes a scalar field
 626 with mass μ . If $\mu^2 < 0$ the potential has a local maximum at $\phi = 0$ and two minima
 627 at $\phi = \pm\sqrt{-\mu^2/\lambda}$ which enables the SSB mechanism to work.

628

629 In the case of a complex scalar field $\phi(x)$

$$\phi(x) = \frac{1}{\sqrt{2}}(\phi_1 + i\phi_2) \quad (2.31)$$

630 the Lagrangian (invariant under global $U(1)$ transformations) is given by

$$\mathcal{L} = (\partial_\mu \phi)^\dagger (\partial^\mu \phi) - V(\phi), \quad V(\phi) = \mu^2 \phi^\dagger \phi + \lambda (\phi^\dagger \phi)^2 \quad (2.32)$$

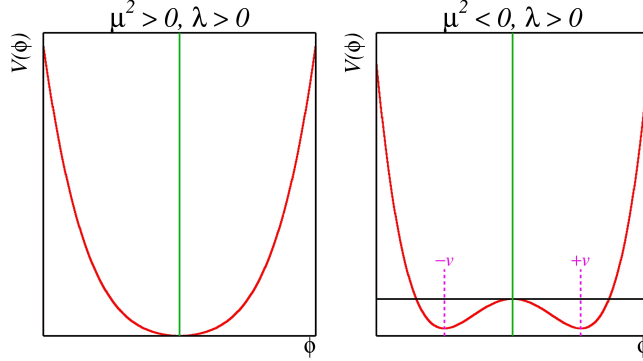


Figure 2.7: Shape of the potential $V(\phi)$ for $\lambda > 0$ and: $\mu^2 > 0$ (left) and $\mu^2 < 0$ (right). The case $\mu^2 < 0$ corresponds to the potential suitable for introducing the SSB mechanism by choosing one of the two ground states which are connected via reflection symmetry. [34].

631 where an appropriate potential has been added in order to introduce the SSB.

632

633 As seen in figure 2.8, the potential has now an infinite number of minima circularly
 634 distributed along the ξ -direction which makes possible the occurrence of the SSB by
 635 choosing an arbitrary ground state; for instance, $\xi = 0$, i.e. $\phi_1 = v, \phi_2 = 0$

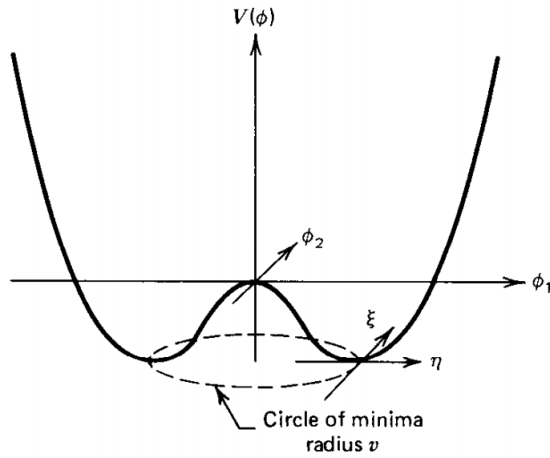


Figure 2.8: Potential for complex scalar field. There is a circle of minima of radius v along the ξ -direction [3].

$$\phi_0 = \frac{v}{\sqrt{2}} \exp(i\xi) \xrightarrow{\text{SSB}} \phi_0 = \frac{v}{\sqrt{2}} \quad (2.33)$$

636 As usual, excitations over the ground state are studied by making an expansion about
 637 it; thus, the excitation can be parametrized as:

$$\phi(x) = \frac{1}{\sqrt{2}}(v + \eta(x) + i\xi(x)) \quad (2.34)$$

638 which when substituted into eqn. 2.32 produces a Lagrangian in terms of the new
 639 fields η and ξ

$$\mathcal{L}' = \frac{1}{2}(\partial_\mu \xi)^2 + \frac{1}{2}(\partial_\mu \eta)^2 + \mu^2 \eta^2 - V(\phi_0) - \lambda v \eta (\eta^2 + \xi^2) - \frac{\lambda}{4}(\eta^2 + \xi^2)^2 \quad (2.35)$$

640 where the last two terms represent the interactions and self-interaction between the
 641 two fields η and ξ . The particular feature of the SSB mechanism is revealed when
 642 looking to the first three terms of \mathcal{L}' . Before the SSB, only the massless ϕ field is
 643 present in the system; after the SSB there are two fields of which the η -field has
 644 acquired mass $m_\eta = \sqrt{-2\mu^2}$ while the ξ -field is still massless (see figure 2.9).

645

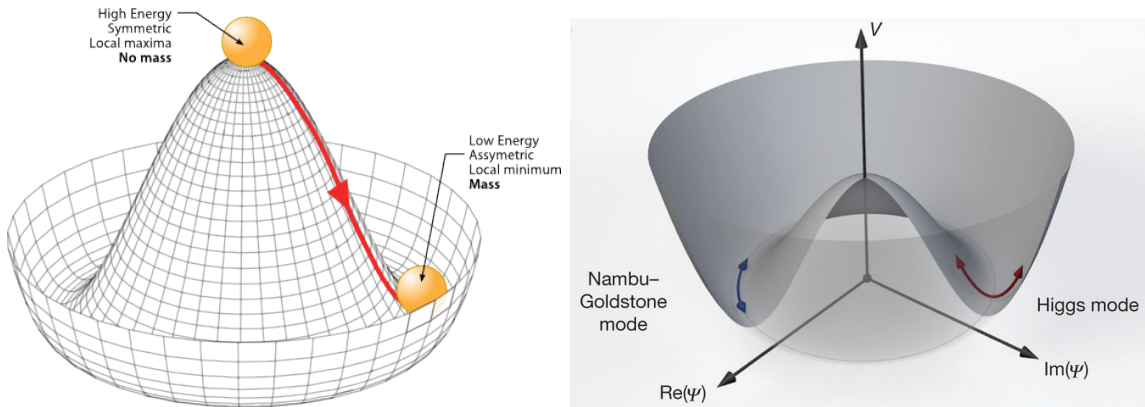


Figure 2.9: SSB mechanism for a complex scalar field [34, 35].

646 Thus, the SSB mechanism serves as a method to generate mass but as a side effect a

647 massless field is introduced in the system. This fact is known as the Goldstone theorem
 648 and states that a massless scalar field appears in the system for each continuous
 649 symmetry spontaneously broken. Another version of the Goldstone theorem states
 650 that “*if a Lagrangian is invariant under a continuous symmetry group G , but the*
 651 *vacuum is only invariant under a subgroup $H \subset G$, then there must exist as many*
 652 *massless spin-0 particles (Nambu-Goldstone bosons) as broken generators.*” [33] The
 653 Nambu-Goldstone boson can be understood considering that the potential in the ξ -
 654 direction is flat so excitations in that direction are not energy consuming and thus
 655 represent a massless state.

656 2.3.2 Higgs mechanism

657 When the SSB mechanism is introduced in the formulation of the EWI in an attempt
 658 to generate the mass of the so far massless gauge bosons and fermions, an interesting
 659 effect is revealed. In order to keep the G symmetry group invariance and generate
 660 the mass of the EW gauge bosons, a G invariant Lagrangian density (\mathcal{L}_S) has to be
 661 added to the non massive EWI Lagrangian (eqn. 2.29)

$$\mathcal{L}_S = (D_\mu \phi)^\dagger (D^\mu \phi) - \mu^2 \phi^\dagger \phi - \lambda (\phi^\dagger \phi)^2, \quad \lambda > 0, \mu^2 < 0 \quad (2.36)$$

$$D_\mu \phi = \left(i\partial_\mu - g \frac{\sigma_i}{2} W_\mu^i - g' \frac{Y}{2} B_\mu \right) \phi \quad (2.37)$$

662 ϕ has to be an isospin doublet of complex scalar fields so it preserves the G invariance;
 663 thus ϕ can be defined as:

$$\phi = \begin{pmatrix} \phi^+ \\ \phi^0 \end{pmatrix} \equiv \frac{1}{\sqrt{2}} \begin{pmatrix} \phi_1 + i\phi_2 \\ \phi_3 + i\phi_4 \end{pmatrix}. \quad (2.38)$$

664 The minima of the potential are defined by

$$\phi^\dagger \phi = \frac{1}{2}(\phi_1^2 + \phi_2^2 + \phi_3^2 + \phi_4^2) = -\frac{\mu^2}{2\lambda}. \quad (2.39)$$

665 The choice of the ground state is critical. By choosing a ground state, invariant under
 666 $U(1)_{em}$ gauge symmetry, the photon will remain massless and the W^\pm and Z bosons
 667 masses will be generated which is exactly what is needed. In that sense, the best
 668 choice corresponds to a weak isospin doublet with $T_3 = -1/2$, $Y_W = 1$ and $Q = 0$
 669 which defines a ground state with $\phi_1 = \phi_2 = \phi_4$ and $\phi_3 = v$:

$$\phi_0 \equiv \frac{1}{\sqrt{2}} \begin{pmatrix} 0 \\ v \end{pmatrix}, \quad v^2 \equiv -\frac{\mu^2}{\lambda}. \quad (2.40)$$

670 where the vacuum expectation value v is fixed by the Fermi coupling G_F according
 671 to $v = (\sqrt{2}G_F)^{1/2} \approx 246$ GeV.

672

673 The G symmetry has been broken and three Nambu-Goldstone bosons will appear.

674 The next step is to expand ϕ about the chosen ground state as:

$$\phi(x) = \frac{1}{\sqrt{2}} \exp\left(\frac{i}{v} \sigma_i \theta^i(x)\right) \begin{pmatrix} 0 \\ v + H(x) \end{pmatrix} \approx \frac{1}{\sqrt{2}} \begin{pmatrix} \theta_1(x) + i\theta_2(x) \\ v + H(x) - i\theta_3(x) \end{pmatrix} \quad (2.41)$$

675 to describe fluctuations from the ground state ϕ_0 . The fields $\theta_i(x)$ represent the
 676 Nambu-Goldstone bosons while $H(x)$ is known as “higgs field.” The fundamental
 677 feature of the parametrization used is that the dependence on the $\theta_i(x)$ fields is
 678 factored out in a global phase that can be eliminated by taking the physical “unitary
 679 gauge” $\theta_i(x) = 0$. Therefore the expansion about the ground state is given by:

$$\phi(x) \frac{1}{\sqrt{2}} \begin{pmatrix} 0 \\ v + H(x) \end{pmatrix} \quad (2.42)$$

680 which when substituted into \mathcal{L}_S (eqn. 2.36) results in a Lagrangian containing the now
 681 massive three gauge bosons W^\pm, Z , one massless gauge boson (photon) and the new
 682 Higgs field (H). The three degrees of freedom corresponding to the Nambu-Goldstone
 683 bosons are now integrated into the massive gauge bosons as their longitudinal po-
 684 larizations which were not available when they were massless particles. The effect
 685 by which vector boson fields acquire mass after an spontaneous symmetry breaking,
 686 but without an explicit gauge invariance breaking is known as the “*Higgs mechanism*”.

687

688 The mechanism was proposed by three independent groups: F.Englert and R.Brout
 689 in August 1964 [36], P.Higgs in October 1964 [37] and G.Guralnik, C.Hagen and
 690 T.Kibble in November 1964 [38]; however, its importance was not realized until
 691 S.Glashow [14], A.Salam [15] and S.Weinberg [16], independently, proposed that elec-
 692 tromagnetic and weak interactions are two manifestations of a more general interac-
 693 tion called “electroweak interaction” in 1967.

694 2.3.3 Masses of the gauge bosons

695 The mass of the gauge bosons is extracted by evaluating the kinetic part of Lagrangian
 696 \mathcal{L}_S in the ground state (known also as the vacuum expectation value), i.e.,

$$\left| \left(\partial_\mu - ig \frac{\sigma_i}{2} W_\mu^i - i \frac{g'}{2} B_\mu \right) \phi_0 \right|^2 = \left(\frac{1}{2} v g \right)^2 W_\mu^+ W^{-\mu} + \frac{1}{8} v^2 (W_\mu^3, B_\mu) \begin{pmatrix} g^2 & -gg' \\ -gg' & g'^2 \end{pmatrix} \begin{pmatrix} W^{3\mu} \\ B^\mu \end{pmatrix} \quad (2.43)$$

697 comparing with the typical mass term for a charged boson $M_W^2 W^+ W^-$

$$M_W = \frac{1}{2} v g. \quad (2.44)$$

The second term in the right side of the eqn.2.43 comprises the masses of the neutral

bosons, but it needs to be written in terms of the gauge fields Z_μ and A_μ in order to be compared to the typical mass terms for neutral bosons, therefore using eqn. 2.28

$$\begin{aligned} \frac{1}{8}v^2[g^2(W_\mu^3)^2 - 2gg'W_\mu^3B^\mu + g'^2B_\mu^2] &= \frac{1}{8}v^2[gW_\mu^3 - g'B_\mu]^2 + 0[g'W_\mu^3 + gB_\mu]^2 \\ &= \frac{1}{8}v^2[\sqrt{g^2 + g'^2}Z_\mu]^2 + 0[\sqrt{g^2 + g'^2}A_\mu]^2 \end{aligned} \quad (2.45)$$

698 and then

$$M_Z = \frac{1}{2}v\sqrt{g^2 + g'^2}, \quad M_A = 0 \quad (2.46)$$

699 2.3.4 Masses of the fermions

700 The lepton mass terms can be generated by introducing a gauge invariant Lagrangian
701 term describing the Yukawa coupling between the lepton field and the Higgs field

$$\mathcal{L}_{Yl} = -G_l \left[(\bar{\nu}_l, \bar{l})_L \begin{pmatrix} \phi^+ \\ \phi^0 \end{pmatrix} l_R + \bar{l}_R (\phi^-, \bar{\phi}^0) \begin{pmatrix} \nu_l \\ l \end{pmatrix}_L \right], \quad l = e, \mu, \tau. \quad (2.47)$$

702 After the SSB and replacing the usual field expansion about the ground state (eqn.2.40)
703 into \mathcal{L}_{Yl} , the mass term arises

$$\mathcal{L}_{Yl} = -m_l(\bar{l}_L l_R + \bar{l}_R l_L) - \frac{m_l}{v}(\bar{l}_L l_R + \bar{l}_R l_L)H = -m_l \bar{l} \left(1 + \frac{H}{v} \right) \quad (2.48)$$

704

$$m_l = \frac{G_l}{\sqrt{2}}v \quad (2.49)$$

705 where the additional term represents the lepton-Higgs interaction. The quark masses
706 are generated in a similar way as lepton masses but for the upper member of the

707 quark doublet a different Higgs doublet is needed:

$$\phi_c = -i\sigma_2\phi^* = \begin{pmatrix} -\bar{\phi}^0 \\ \phi^- \end{pmatrix}. \quad (2.50)$$

708 Additionally, given that the quark isospin doublets are not constructed in terms of
 709 the mass eigenstates but in terms of the flavor eigenstates, as shown in table 2.5, the
 710 coupling parameters will be related to the CKM matrix elements; thus the quark
 711 Lagrangian is given by:

$$\mathcal{L}_{Yq} = -G_d^{i,j}(\bar{u}_i, \bar{d}_i)_L \begin{pmatrix} \phi^+ \\ \phi^0 \end{pmatrix} d_{jR} - G_u^{i,j}(\bar{u}_i, \bar{d}_i)_L \begin{pmatrix} -\bar{\phi}^0 \\ \phi^- \end{pmatrix} u_{jR} + h.c. \quad (2.51)$$

712 with $i,j=1,2,3$. After SSB and expansion about the ground state, the diagonal form
 713 of \mathcal{L}_{Yq} is:

$$\mathcal{L}_{Yq} = -m_d^i \bar{d}_i d_i \left(1 + \frac{H}{v} \right) - m_u^i \bar{u}_i u_i \left(1 + \frac{H}{v} \right) \quad (2.52)$$

714 Fermion masses depend on arbitrary couplings G_l and $G_{u,d}$ and are not predicted by
 715 the theory.

716 2.3.5 The Higgs field

717 After the characterization of the fermions and gauge bosons as well as their interac-
 718 tions, it is necessary to characterize the Higgs field itself. The Lagrangian \mathcal{L}_S in eqn.
 719 2.36 written in terms of the gauge bosons is given by

$$\mathcal{L}_S = \frac{1}{4}\lambda v^4 + \mathcal{L}_H + \mathcal{L}_{HV} \quad (2.53)$$

720

$$\mathcal{L}_H = \frac{1}{2}\partial_\mu H \partial^\mu H - \frac{1}{2}m_H^2 H^2 - \frac{1}{2v}m_H^2 H^3 - \frac{1}{8v^2}m_H^2 H^4 \quad (2.54)$$

721

$$\mathcal{L}_{HV} = m_H^2 W_\mu^+ W^{\mu-} \left(1 + \frac{2}{v}H + \frac{2}{v^2}H^2 \right) + \frac{1}{2}m_Z^2 Z_\mu Z^\mu \left(1 + \frac{2}{v}H + \frac{2}{v^2}H^2 \right) \quad (2.55)$$

722 The mass of the Higgs boson is deduced as usual from the mass term in the Lagrangian
 723 resulting in:

$$m_H = \sqrt{-2\mu^2} = \sqrt{2\lambda}v \quad (2.56)$$

724 however, it is not predicted by the theory either. The experimental efforts to find
 725 the Higgs boson, carried out by the “Compact Muon Solenoid (CMS)” experiment
 726 and the “A Toroidal LHC AppartuS (ATLAS)” experiments at the “Large Hadron
 727 Collider(LHC)”, gave great results by July of 2012 when the discovery of a new
 728 particle compatible with the Higgs boson predicted by the electroweak theory [39, 40]
 729 was announced. Although at the announcement time there were some reservations
 730 about calling the new particle the “Higgs boson”, today this name is widely accepted.
 731 The Higgs mass measurement, reported by both experiments [41], is in table 2.8.

Property	Value
Electric charge	0
Colour charge	0
Spin	0
Weak isospin	-1/2
Weak hypercharge	1
Parity	1
Mass (GeV/c ²)	125.09±0.21 (stat.)±0.11 (syst.)

Table 2.8: Higgs boson properties. Higgs mass is not predicted by the theory and the value here corresponds to the experimental measurement.

732

733 2.3.6 Higgs boson production mechanisms at LHC.

734 At LHC, Higgs boson is produced as a result of the collision of two counter-rotating
 735 protons beams. A detailed description of the LHC machine will be presented in
 736 chapter 3. “The total cross section” is a parameter that quantifies the number of pp
 737 collisions that happen when a number of protons are fired at each other. Different
 738 results can be obtained after a pp collision and for each one the “cross section” is

defined as the number of pp collisions that conclude in that particular result with respect to the number of protons fired at each other.

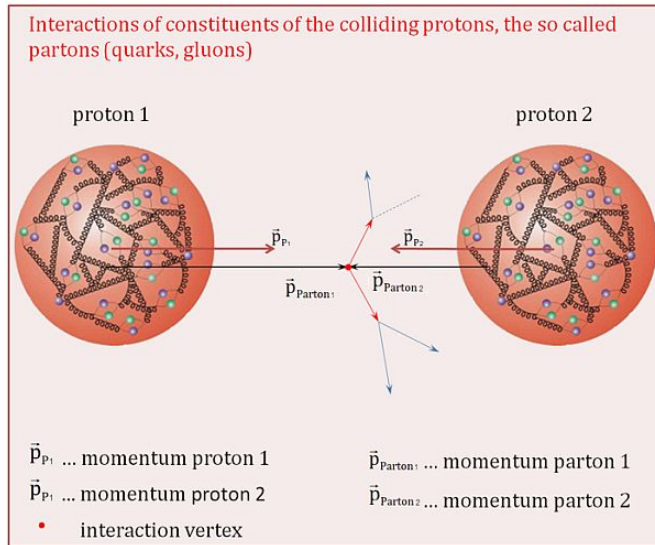


Figure 2.10: Proton-proton collision. Protons are composed of 3 valence quarks, a sea of quarks and gluons; therefore in a proton-proton collision, quarks and gluons are those who collide. [45].

740

741 Protons are composed of quarks and these quarks are bound by gluons; however,
742 what is commonly called the quark content of the proton makes reference to the
743 valence quarks. A sea of quarks and gluons is also present inside the proton as repre-
744 sented in figure 2.10. In a proton-proton (pp) collision, the constituents (quarks and
745 gluons) are those who collide. The pp cross section depends on the momentum of
746 the colliding particles, reason for which it is needed to know how the momentum is
747 distributed inside the proton. Quarks and gluons are known as partons and the func-
748 tions that describe how the proton momentum is distributed among partons inside it
749 are called “parton distribution functions (PDFs)”; PDFs are determined from experi-
750 mental data obtained in experiments where the internal structure of hadrons is tested.

751

⁷⁵² In addition, in physics, a common approach to study complex systems consists in

753 starting with a simpler version of them, for which a well known description is avail-
 754 able, and add an additional “perturbation” which represents a small deviation from
 755 the known behavior. If the perturbation is small enough, the physical quantities as-
 756 sociated with the perturbed system are expressed as a series of corrections to those
 757 of the simpler system; therefore, the more terms are considered in the series (the
 758 higher order in the perturbation series), the more precise is the the description of the
 759 complex system.

760

761 This thesis explores the Higgs production at LHC; therefore the overview presented
 762 here will be oriented specifically to the production mechanisms after pp collisions at
 763 LHC.

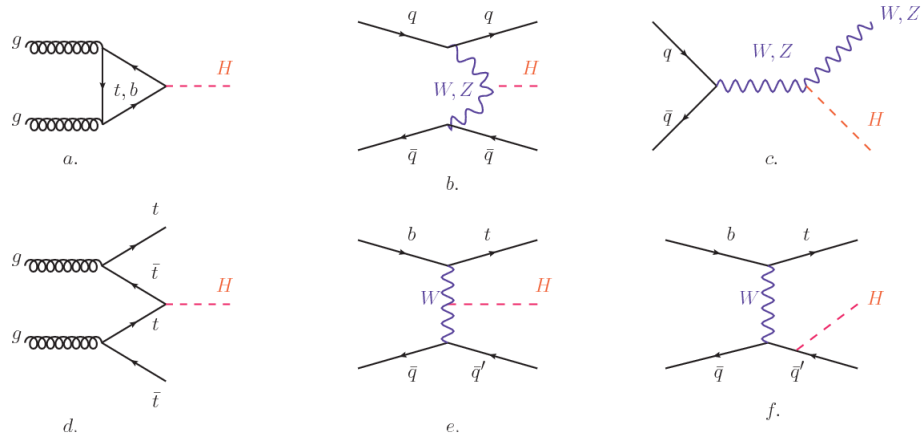


Figure 2.11: Main Higgs production mechanism Feynman diagrams. a. gluon-gluon fusion, b. vector boson fusion (VBF), c. Higgs-strahlung, d. Associated production with a top or bottom quark pair, e-f. associated production with a single top quark.

764 Figure 2.11 shows the Feynman diagrams for the leading order (first order) Higgs
 765 production processes at LHC, while the cross section for Higgs production as a func-
 766 tion of the center of mass-energy (\sqrt{s}) for pp collisions is showed in figure 2.12 left.
 767 The tags NLO (next to leading order), NNLO (next to next to leading order) and
 768 N3LO (next to next to next to leading order) make reference to the order at which

769 the perturbation series have been considered.

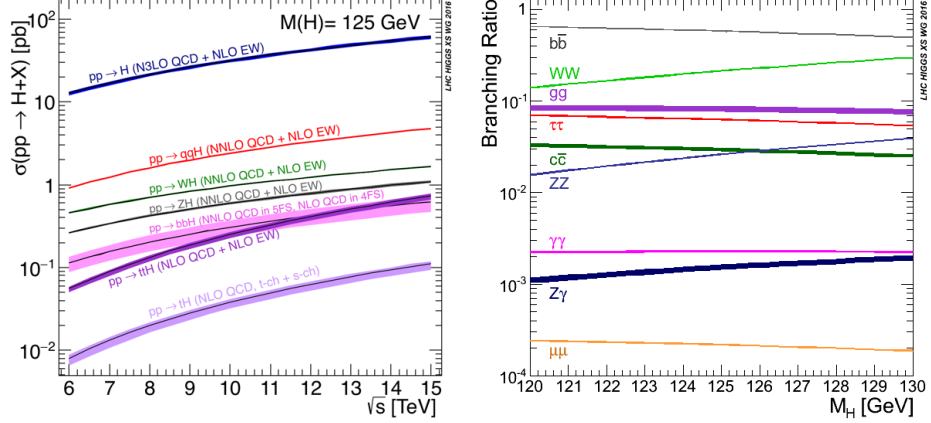


Figure 2.12: Higgs production cross sections (left) and decay branching ratios (right) for the main mechanisms. The VBF is indicated as $q\bar{q}H$ [42].

770 As shown in eqns 2.47, 2.51 and 2.55, the strength of the Higgs-fermion interaction
 771 is proportional to the fermion mass while the strength of the Higgs-gauge boson
 772 interaction is proportional to the square of the gauge boson mass, which implies
 773 that the Higgs production and decay mechanisms are dominated by couplings $H -$
 774 (W, Z, t, b, τ) .

775 The main production mechanism is the gluon fusion (figure 2.11a and $pp \rightarrow H$ in figure
 776 2.12) given that gluons carry the highest fraction of momentum of the protons in pp
 777 colliders. Since the Higgs boson does not couple to gluons, the mechanism proceeds
 778 through the exchange of a virtual top-quark loop given that for it the coupling is
 779 the biggest. Note that in this process, the Higgs boson is produced alone, which
 780 makes this mechanism experimentally clean when combined with the two-photon or
 781 the four-lepton decay channels (see section 2.3.7).

782 Vector boson fusion (figure 2.11b and $pp \rightarrow q\bar{q}H$ in figure 2.12) has the second largest
 783 production cross section. The scattering of two fermions is mediated by a weak
 784 gauge boson which later emits a Higgs boson. In the final state, the two fermions

785 tend to be located in a particular region of the detector which is used as a signature
 786 when analyzing the datasets provided by the experiments. More details about how
 787 to identify events of interest in an analysis will be given in chapter 4.

788 The next production mechanism is Higgs-strahlung (figure 2.11c and $pp \rightarrow WH, pp \rightarrow$
 789 ZH in figure 2.12) where two fermions annihilate to form a weak gauge boson. If the
 790 initial fermions have enough energy, the emergent boson eventually will emit a Higgs
 791 boson.

792 The associated production with a top or bottom quark pair and the associated pro-
 793 duction with a single top quark (figure 2.11d-f and $pp \rightarrow bbH, pp \rightarrow t\bar{t}H, pp \rightarrow tH$
 794 in figure 2.12) have a smaller cross section than the main three mechanisms above,
 795 but they provide a good opportunity to test the Higgs-top coupling. The analysis
 796 reported in this thesis is developed using these production mechanisms. A detailed
 797 description of the tH mechanism will be given in section 2.4.

798 2.3.7 Higgs decay channels

799 When a particle can decay through several modes, also known as channels, the
 800 probability of decaying through a given channel is quantified by the “branching ratio
 801 (BR)” of the decay channel; thus, the BR is defined as the ratio of number of decays
 802 going through that given channel to the total number of decays. In regard to the
 803 Higgs boson decay, the BR can be predicted with accuracy once the Higgs mass is
 804 known [43, 44]. In figure 2.12 right, a plot of the BR as a function of the Higgs mass
 805 is presented. The largest predicted BR corresponds to the $b\bar{b}$ pair decay channel (see
 806 table 2.9).

Decay channel	Branching ratio	Rel. uncertainty
$H \rightarrow bb$	5.84×10^{-1}	+3.2% – 3.3%
$H \rightarrow W^+W^-$	2.14×10^{-1}	+4.3% – 4.2%
$H \rightarrow \tau^+\tau^-$	6.27×10^{-2}	+5.7% – 5.7%
$H \rightarrow ZZ$	2.62×10^{-2}	+4.3% – 4.1%
$H \rightarrow \gamma\gamma$	2.27×10^{-3}	+5.0% – 4.9%
$H \rightarrow Z\gamma$	1.53×10^{-3}	+9.0% – 8.9%
$H \rightarrow \mu^+\mu^-$	2.18×10^{-4}	+6.0% – 5.9%

Table 2.9: Predicted branching ratios and the relative uncertainty for a SM Higgs boson with $m_H = 125 GeV/c^2$. [21]

808 2.4 Associated Production of Higgs Boson and 809 Single Top Quark.

810 Associated production of Higgs boson has been extensively studied [46–50]. While
811 measurements of the main Higgs production mechanisms rates are sensitive to the
812 strength of the Higgs coupling to W boson or top quark, they are not sensitive to the
813 relative sign between the two couplings. In this thesis, the Higgs boson production
814 mechanism explored is the associated production with a single top quark (*th*) which
815 offers sensitiveness to the relative sign of the Higgs couplings to W boson and to top
816 quark. The description given here is based on the reference [48]

817
818 A process where two incoming particles interact and produce a final state with two
819 particles can proceed in three ways also called channels (see, for instance, figure 2.13
820 ommiting the red line). The t-channel represents processes where an intermediate
821 particle is emitted by one of the incoming particles and absorbed by the other. The
822 s-channel represents processes where the two incoming particles merge into an inter-
823 mediate particle which eventually will split into the particles in the final state. The
824 third channel, u-channel, is similar to the t-channel but the two outgoing particles

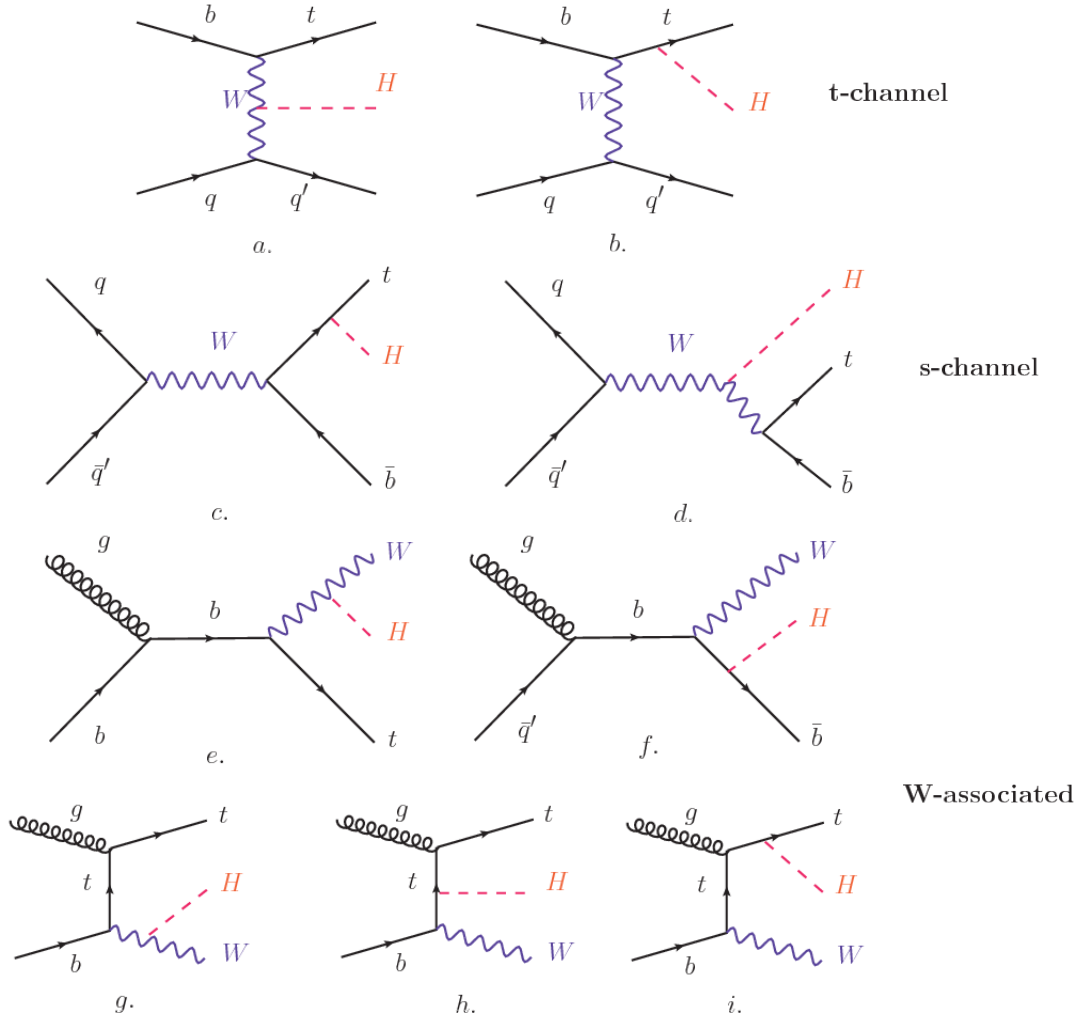


Figure 2.13: Associated higgs production mechanism Feynman diagrams. a.,b. t-channel (tHq), c.,d. s-channel ($tH\bar{b}$), e.-i. W-associated.

825 interchange their roles.

826

827 The th production, where Higgs boson can be radiated either from the top quark or
 828 from the W boson, is represented by the leading order Feynman diagrams in figure
 829 2.13. The cross section for the th process is calculated, as usual, summing over
 830 the contributions from the different feynman diagrams; therefore it depends on the
 831 interference between the contributions. In the SM, the interference for t-channel (tHq

process) and W-associated (tHW process) production is destructive [46] resulting in the small cross sections presented in table 2.10.

tH production channel	Cross section (fb)
t-channel ($pp \rightarrow tHq$)	$70.79^{+2.99}_{-4.80}$
W-associated ($pp \rightarrow tHW$)	$15.61^{+0.83}_{-1.04}$
s-channel($pp \rightarrow tHb$)	$2.87^{+0.09}_{-0.08}$

Table 2.10: Predicted SM cross sections for tH production at $\sqrt{s} = 13$ TeV [51, 52].

834

835 While the s-channel contribution can be neglected, it will be shown that a deviation
 836 from the SM destructive interference would result in an enhancement of the th cross
 837 section compared to that in SM, which could be used to get information about the
 838 sign of the Higgs-top coupling [48, 49]. In order to describe th production processes,
 839 Feynman diagram 2.13b will be considered; there, the W boson is radiated by a
 840 quark in the proton and eventually it will interact with the b quark. In the high
 841 energy regime, the effective W approximation [53] allows to describe the process as
 842 the emmision of an approximately on-shell W and its hard scattering with the b
 843 quark; i.e. $Wb \rightarrow th$. The scattering amplitude for the process is given by

$$\mathcal{A} = \frac{g}{\sqrt{2}} \left[(\kappa_t - \kappa_V) \frac{m_t \sqrt{s}}{m_W v} A \left(\frac{t}{s}, \varphi; \xi_t, \xi_b \right) + \left(\kappa_V \frac{2m_W s}{v} \frac{1}{t} + (2\kappa_t - \kappa_V) \frac{m_t^2}{m_W v} \right) B \left(\frac{t}{s}, \varphi; \xi_t, \xi_b \right) \right], \quad (2.57)$$

844 where $\kappa_V \equiv g_{HVV}/g_{HVV}^{SM}$ and $\kappa_t \equiv g_{Ht}/g_{Ht}^{SM} = y_t/y_t^{SM}$ are scaling factors that quan-
 845 tify possible deviations of the couplings, Higgs-Vector boson (H-W) and Higgs-top
 846 (H-t) respectively, from the SM couplings; $s = (p_W + p_b)^2$, $t = (p_W - p_H)^2$, φ is the
 847 Higgs azimuthal angle around the z axis taken parallel to the direction of motion of
 848 the incoming W; A and B are funtions describing the weak interaction in terms of

849 the chiral states of the quarks b and t. Terms that vanish in the high energy limit
 850 have been neglected as well as the Higgs and b quark masses⁸.

851

852 The scattering amplitude grows with energy like \sqrt{s} for $\kappa_V \neq \kappa_t$, in contrast to
 853 the SM ($\kappa_t = \kappa_V = 1$), where the first term in 2.57 cancels out and the amplitude
 854 is constant for large s; therefore, a deviation from the SM predictions represents an
 855 enhancement in the tHq cross section. In particular, for a SM H-W coupling and a H-t
 856 coupling of inverted sign with respect to the SM ($\kappa_V = -\kappa_t = 1$) the tHq cross section
 857 is enhanced by a factor greater 10 as seen in the figure 2.14 taken from reference [48];
 858 reference [54] has reported similar enhancement results.

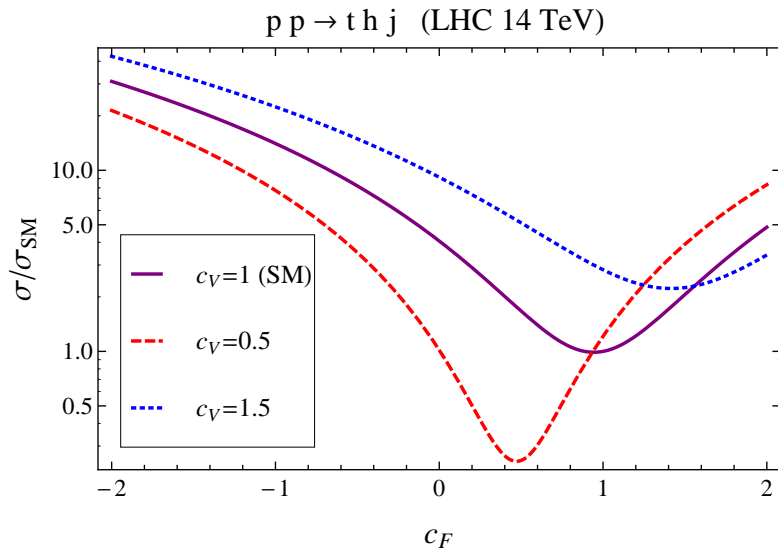


Figure 2.14: Cross section for tHq process as a function of κ_t , normalized to the SM, for three values of κ_V . In the plot c_f refers to the Higgs-fermion coupling which is dominated by the H-t coupling and represented here by κ_t . Solid, dashed and dotted lines correspond to $c_V \rightarrow \kappa_V = 1, 0.5, 1.5$ respectively. Note that for the SM ($\kappa_V = \kappa_t = 1$), the destructive effect of the interference is maximal.

859 A similar analysis is valid for the W-associated channel but, in that case, the inter-
 860 ference is more complicated since there are more than two contributions and an ad-

⁸ A detailed explanation of the structure and approximations used to derive \mathcal{A} can be found in reference [48]

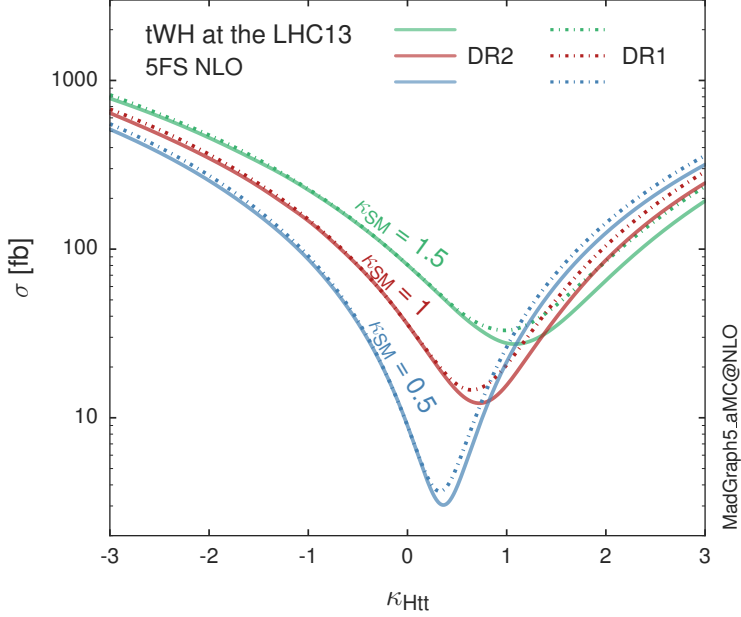


Figure 2.15: Cross section for tHW process as a function of κ_{Htt} , for three values of κ_{SM} at $\sqrt{s} = 13$ TeV. $\kappa_{Htt}^2 = \sigma_{Htt}/\sigma_{Htt}^{SM}$ is a simple rescaling of the SM Higgs interactions.

ditional interference with the production of Higgs boson and a top pair process($t\bar{t}H$).
 The calculations are made using the so-called Diagram Removal (DR) technique where
 interfering diagrams are removed (or added) from the calculations in order to evaluate
 the impact of the removed contributions. DR1 was defined to neglect $t\bar{t}H$ interference
 while DR2 was defined to take $t\bar{t}H$ interference into account [55]. As shown in figure
 2.15, the tHW cross section is enhanced from about 15 fb (SM: $\kappa_{Htt} = 1$) to about
 150 fb ($\kappa_{Htt} = -1$). Differences between curves for DR1 and DR2 help to gauge the
 impact of the interference with $t\bar{t}H$.
 Results of the calculations of the tHq and tHW cross sections at $\sqrt{s} = 13$ TeV can be
 found in reference [56] and a summary of the results is presented in table 2.11.

	\sqrt{s} TeV	$\kappa_t = 1$	$\kappa_t = -1$
$\sigma^{LO}(tHq)(\text{fb})$ [48]	8	≈ 17.4	≈ 252.7
	14	≈ 80.4	≈ 1042
$\sigma^{NLO}(tHq)(\text{fb})$ [48]	8	$18.28^{+0.42}_{-0.38}$	$233.8^{+4.6}_{-0.0}$
	14	$88.2^{+1.7}_{-0.0}$	$982.8^{+28}_{-0.0}$
$\sigma^{LO}(tHq)(\text{fb})$ [54]	14	≈ 71.8	≈ 893
$\sigma^{LO}(tHW)(\text{fb})$ [54]	14	≈ 16.0	≈ 139
$\sigma^{NLO}(tHq)(\text{fb})$ [56]	8	$18.69^{+8.62\%}_{-17.13\%}$	-
	13	$74.25^{+7.48\%}_{-15.35\%}$	$848^{+7.37\%}_{-13.70\%}$
	14	$90.10^{+7.34\%}_{-15.13\%}$	$1011^{+7.24\%}_{-13.39\%}$
$\sigma^{LO}(tHW)(\text{fb})$ [55]	13	$15.77^{+15.91\%}_{-15.76\%}$	-
$\sigma^{NLO}DR1(tHW)(\text{fb})$ [55]	13	$21.72^{+6.52\%}_{-5.24\%}$	≈ 150
$\sigma^{NLO}DR2(tHW)(\text{fb})$ [55]	13	$16.28^{+7.34\%}_{-15.13\%}$	≈ 150

Table 2.11: Predicted enhancement of the tHq and tHW cross sections at LHC for $\kappa_V = 1$ and $\kappa_t = \pm 1$ at LO and NLO; the cross section enhancement of more than a factor of 10 is due to the flippling in the sign of the H-t coupling with respect to the SM one.

872 2.5 The CP-mixing in tH processes

873 In addition to the sensitivity to sign of the H-t coupling, tHq and tHW processes have
 874 been proposed as a tool to investigate the possibility of a H-t coupling that does not
 875 conserve CP [50, 55, 57]. Current experimental results are consistent with SM H-V
 876 and H-t couplings; however, negative H-t coupling is not excluded completely [59].

877

878 In this thesis, the sensitivity of th processes to CP-mixing is also studied in the
 879 effective field theory framework and based in references [50, 55]; a generic particle
 880 (X_0) of spin-0 and a general CP violating interaction with the top quark, can couple
 881 to scalar and pseudoscalar fermionic densities. The H-W interaction is assumed to
 882 be SM-like. The Lagrangian modeling the H-t interaction is given by

$$880 \quad \mathcal{L}_0^t = -\bar{\psi}_t (c_\alpha \kappa_{Htt} g_{Htt} + i s_\alpha \kappa_{Att} g_{Att} \gamma_5) \psi_t X_0, \quad (2.58)$$

883 where α is the CP-mixing phase, $c_\alpha \equiv \cos \alpha$ and $s_\alpha \equiv \sin \alpha$, κ_{Htt} and κ_{Att} are real
 884 dimensionless rescaling parameters⁹, $g_{Htt} = g_{Att} = m_t/v = y_t/\sqrt{2}$ and $v \sim 246$ GeV is
 885 the Higgs vacuum expectation value. In this parametrization, it is easy to recover
 886 three special cases

- 887 • CP-even coupling $\rightarrow \alpha = 0^\circ$
- 888 • CP-odd coupling $\rightarrow \alpha = 90^\circ$
- 889 • SM coupling $\rightarrow \alpha = 0^\circ$ and $\kappa_{Htt} = 1$

890 The loop induced X_0 coupling to gluons can also be described in terms of the
 891 parametrization above, according to

$$\mathcal{L}_0^g = -\frac{1}{4} \left(c_\alpha \kappa_{Hgg} g_{Hgg} G_{\mu\nu}^a G^{a,\mu\nu} + s_\alpha \kappa_{Agg} g_{Agg} G_{\mu\nu}^a \tilde{G}^{a,\mu\nu} \right) X_0. \quad (2.59)$$

892 where $g_{Hgg} = -\alpha_s/3\pi v$ and $g_{Agg} = \alpha_s/2\pi v$. Under the assumption that the top quark
 893 dominates the gluon-fusion process at LHC energies, $\kappa_{Hgg} \rightarrow \kappa_{Htt}$ and $\kappa_{Agg} \rightarrow \kappa_{Att}$,
 894 so that the ratio between the gluon-gluon fusion cross section for X_0 and for the SM
 895 Higgs prediction can be written as

$$\frac{\sigma_{NLO}^{gg \rightarrow X_0}}{\sigma_{NLO,SM}^{gg \rightarrow H}} = c_\alpha^2 \kappa_{Htt}^2 + s_\alpha^2 \left(\kappa_{Att} \frac{g_{Agg}}{g_{Hgg}} \right)^2. \quad (2.60)$$

896 If the rescaling parameters are set to

$$\kappa_{Htt} = 1, \quad \kappa_{Att} = \left| \frac{g_{Hgg}}{g_{Agg}} \right| = \frac{2}{3}. \quad (2.61)$$

897 the gluon-fusion SM cross section is reproduced for every value of the CP-mixing
 898 angle α ; therefore, by imposing that condition to the Lagrangian density 2.58, the

⁹ analog to κ_t and κ_V

CP-mixing angle is not constrained by current data. Figure 2.16 shows the NLO cross sections for t-channel tX_0 (blue) and $t\bar{t}X_0$ (red) associated production processes as a function of the CP-mixing angle α . X_0 is a generic spin-0 particle with top quark CP-violating coupling. Rescaling factors κ_{Htt} and κ_{Att} have been set to reproduce the SM gluon-fusion cross sections.

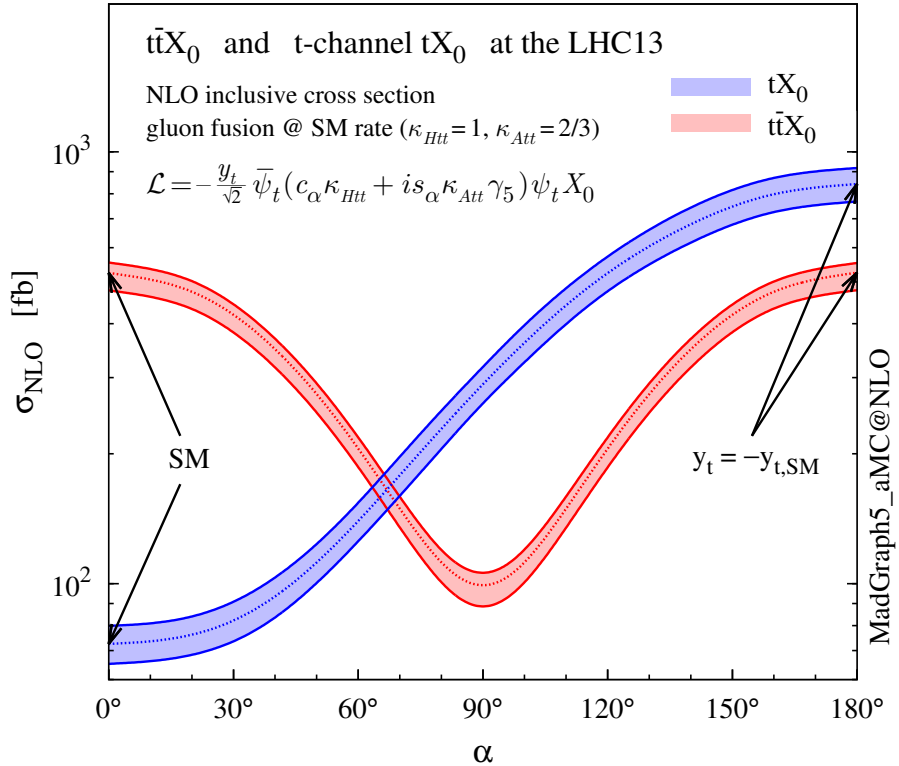


Figure 2.16: NLO cross sections for t-channel tX_0 (blue) and $t\bar{t}X_0$ (red) associated production processes as a function of the CP-mixing angle α . X_0 is a generic spin-0 particle with top quark CP-violating coupling [50].

It is interesting to notice that the tX_0 cross section is enhanced, by a factor of about 10, when a continuous rotation in the scalar-pseudoscalar plane is applied; this enhancement is similar to the enhancement produced when the H-t coupling is flipped in sign with respect to the SM ($y_t = -y_{t,SM}$ in the plot), as showed in section 2.4. In contrast, the degeneracy in the $t\bar{t}X_0$ cross section is still present given that it depends

quadratically on the H-t coupling, but more interesting is to notice that $t\bar{t}X_0$ cross section is exceeded by tX_0 cross section after $\alpha \sim 60^\circ$.

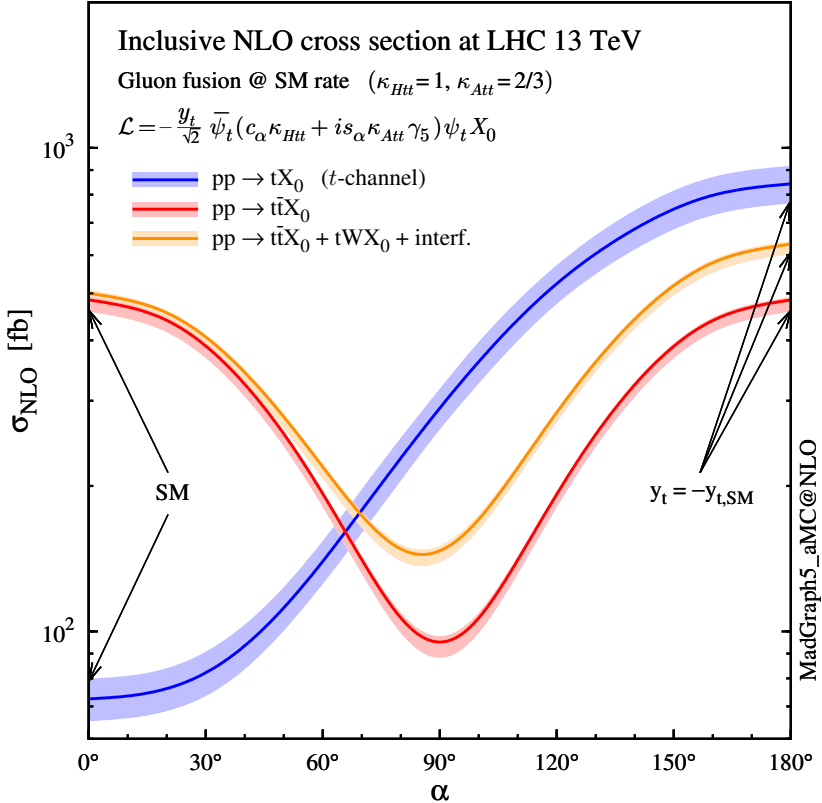


Figure 2.17: NLO cross sections for t-channel tX_0 (blue), $t\bar{t}X_0$ (red) associated production processes and combined $tWX_0 + t\bar{t}X_0$ (including interference) production as a function of the CP-mixing angle α [50].

910

911 A similar parametrization can be used to investigate the tHW process sensitivity to
 912 CP-violating H-t coupling. As said in 2.4, the interference in the W-associated chan-
 913 nel is more complicated because there are more than two contributions and also there
 914 is interference with the $t\bar{t}H$ production process.

915

916 Figure 2.17 shows the NLO cross sections for t-channel tX_0 (blue), $t\bar{t}X_0$ (red) asso-
 917 ciated production and for the combined $tWX_0 + t\bar{t}X_0 +$ interference (orange) as a
 918 function of the CP-mixing angle. It is clear that the effect of the interference in the

919 combined case is the lifting of the degeneracy present in the $t\bar{t}X_0$ production. The
 920 constructive interference enhances the cross section from about 500 fb at SM ($\alpha = 0$)
 921 to about 600 fb ($\alpha = 180^\circ \rightarrow y_t = -y_{t,SM}$).

922 An analysis combining tHq and tHW processes will be made in this thesis taking
 923 advantage of the sensitivity improvement.

924 **2.6 Experimantal status of anomalous**
 925 **Higg-fermion coupling.**

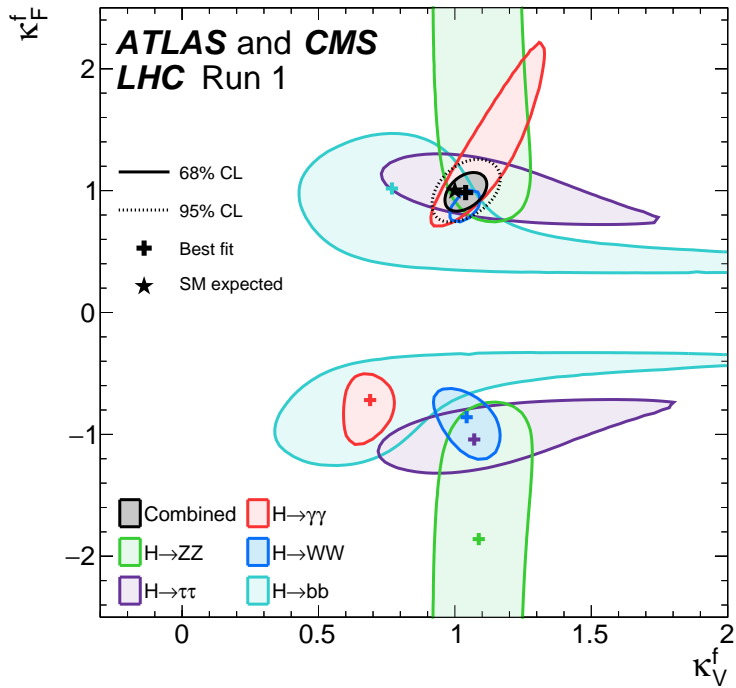


Figure 2.18: Combination of coupling modifiers κ_t - κ_V fits of ATLAS and CMS; also shown the individual decay channels combination and their global combination. No assumptions have been made on the sign of the coupling modifiers [59].

926 ATLAS and CMS have performed analysis of the anomalous H-f coupling by making
 927 likelihood scans for the two coupling modifiers, κ_t and κ_V , under the assumption that

928 $\kappa_Z = \kappa_W = \kappa_V$ and $\kappa_t = \kappa_\tau = \kappa_b = \kappa_f$. Figure 2.18 shows the result of the combination
929 of ATLAS and CMS fits; also the individual decay channels combination and the
930 global combination result are shown.

931 While all the channels are compatible for positive values of the modifiers, for negative
932 values of κ_t there is no compatibility. The best fit for individual channels is compatible
933 with negative values of κ_t except for the $H \rightarrow bb$ channel which is expected to be the
934 most sensitive channel; therefore, the best fit for the global fit yields $\kappa_t \geq 0$. Thus,
935 the anomalous H-t coupling cannot be excluded completely.

₉₃₆ **Chapter 3**

₉₃₇ **The CMS experiment at the LHC**

₉₃₈ **3.1 Introduction**

₉₃₉ Located in the Swiss-French border, the European Council for Nuclear Research
₉₄₀ (CERN) is the largest scientific organization leading the particle physics research.
₉₄₁ About 13000 people in a broad range of fields including users, students, scientists,
₉₄₂ engineers among others, contribute to the data taking and analysis, with the goal
₉₄₃ of unveiling the secrets of the nature and revealing the fundamental structure of the
₉₄₄ universe. CERN is also the home of the Large Hadron Collider (LHC), the largest
₉₄₅ circular particle accelerator around the world, where protons (or heavy ions) travel-
₉₄₆ ing close to the speed of light, are made to collide. These collisions open a window
₉₄₇ to investigate how particles (and their constituents if they are composite) interact
₉₄₈ with each other, providing clues about the laws of the nature. This chapter present
₉₄₉ an overview of the LHC structure and operation. A detailed description of the CMS
₉₅₀ detector is offered, given that the data used in this thesis have been taken with this
₉₅₁ detector.

952 3.2 The LHC

953 With 27 km of circumference, the LHC is currently the largest and most powerful
 954 accelerator in the world. It is installed in the same tunnel where the large Electron-
 955 Positron (LEP) collider was located, taking advantage of the existing infraestructure.
 956 The LHC is also the larger accelerator in the CERN's accelerator complex and is
 957 assisted by several successive accelerating stages before the particles are injected into
 958 the LHC ring where they reach their maximum eneregy (see figure 3.1).

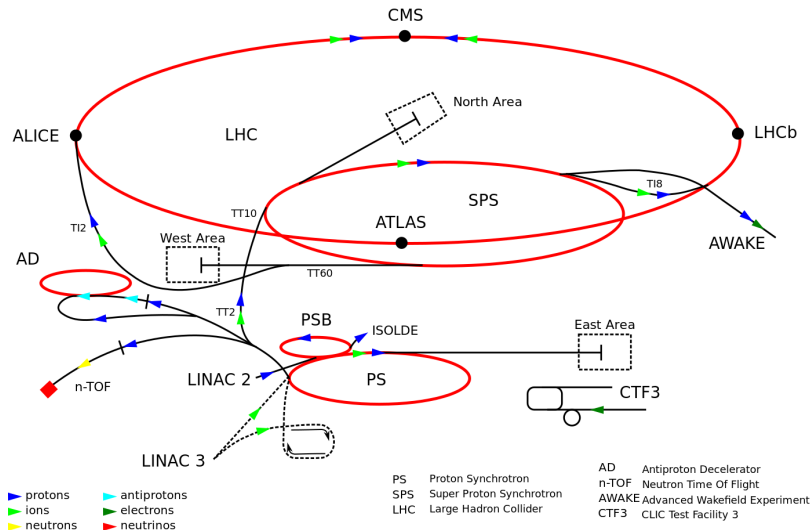


Figure 3.1: CERN accelerator complex. Blue arrows show the path followed by protons along the acceleration process [60].

959 LHC run in three modes depending on the particles being accelerated

- 960 ● Proton-Proton collisions (pp) for multiple physics experiments.
- 961 ● Lead-Lead collisions (Pb-Pb) for heavy ion experiments.
- 962 ● Proton-Lead collisions (p-Pb) for quark-gluon plasma experiments.

963 In this thesis pp collisions will be considered.

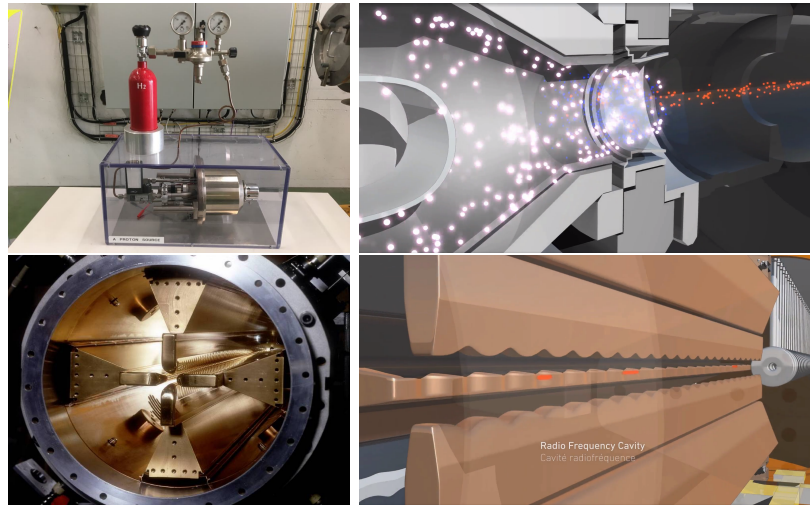


Figure 3.2: LHC protons source and first acceleration stage. Top: the bottle contains hydrogen gas (white dots) which is injected into the metal cylinder to be broken down into electrons(blue dots) and protons(red dots); Bottom: the obtained protons are directed towards the radio frequency quadrupole which perform the first acceleration, focus the beam and create the bunches of protons. [64, 65]

965 Collection of protons starts with hydrogen atoms taken from a bottle, containing hy-
 966 drogen gas, and injecting them in a metal cillinder; hydrogen atoms are broken down
 967 into electrons and protons by an intense electric field (see figure3.2 top). The result-
 968 ing protons leave the metal cylinder towards a radio frecuency quadrupole (RFQ)
 969 that focus the beam, accelerate the protons and create the packets of protons called
 970 bunches. In the RFQ, an electric field is generated by a RF wave at a frecuency that
 971 matches the resonance frecuency of the cavity where the electrodes are contained.
 972 The beam of protons traveling on the RFQ axis experience an alternating electric
 973 field gradient that generates the focusing forces.

974

975 In order to accelerate the protons, a longitudinal time-varying electric field compo-
 976 nent is added to the system; it is done by giving the electrodes a sinus-like profile as
 977 shown in figure 3.2 bottom. By matching the speed and phase of the protons with the
 978 longitudinal electric field the bunching is performed; protons synchronized with the

979 RFQ (synchronous proton) does not feel an accelerating force, but those protons in
 980 the beam that have more (or less) energy than the synchronous proton (asynchronous
 981 protons) will feel a decelerating (accelerating) force; therefore, asynchronous protons
 982 will oscillate around the synchronous ones forming bunches of protons [62]. From
 983 the RFQ emerges protons with energy 750 keV in bunches of about 1.15×10^{11} pro-
 984 tons [63].

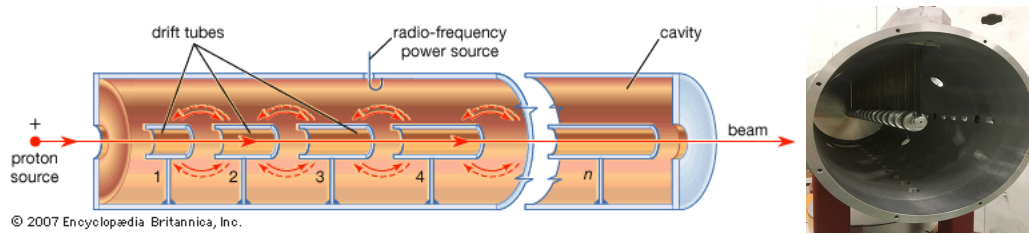


Figure 3.3: The LINAC2 accelerating system at CERN. Radio frequency (RF) generated electric fields create acceleration and deceleration zones inside the cavity; deceleration zones are blocked by drift tubes where quadrupole magnets focus the proton beam. [66]

985 Proton bunches coming from the RFQ goes to the linear accelerator 2 (LINAC2)
 986 where they are accelerated to reach 50 MeV energy. In the LINAC2 stage, acceler-
 987 ation is performed using radio frequency generated electric fields which create zones
 988 of acceleration and deceleration as shown in figure 3.3. In the decelerations zones
 989 the electric field is blocked using drift tubes where protons are free to drift while
 990 quadrupole magnets focus the beam.

991

992 The beam coming from LINAC2 is injected into the proton synchrotron booster
 993 (PSB) to reach 1.4 GeV in energy. The next acceleration is provided at the pro-
 994 ton synchrotron (PS) up to 26 GeV, followed by the injection into the super proton
 995 synchrotron (SPS) where protons are accelerated to 450 GeV. Finally, protons are
 996 injected into the LHC where they are accelerated to the target energy of 6.5 TeV.
 997 PSB, PS, SPS and LHC accelerate protons using the same RF acceleration technic

998 described before.

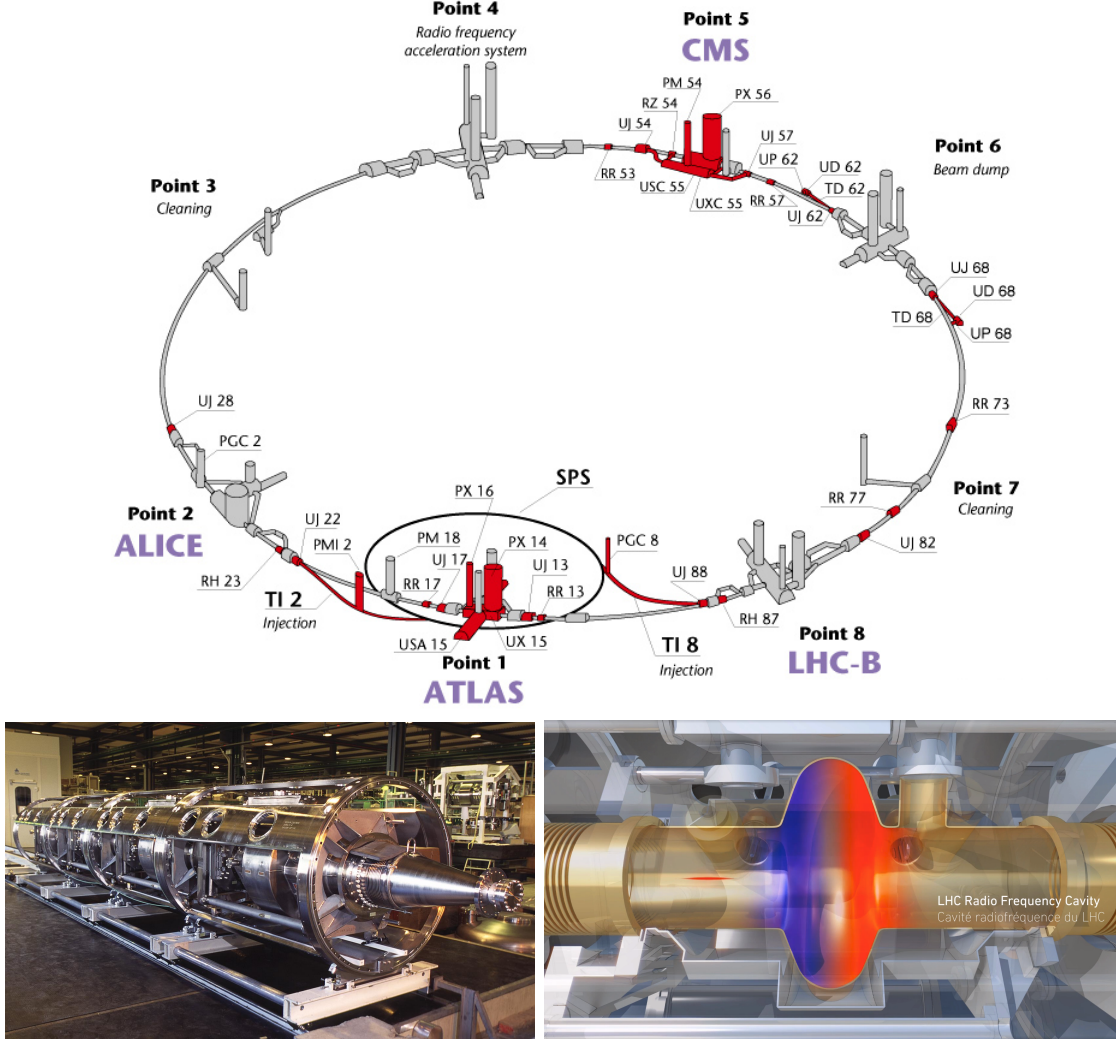


Figure 3.4: Top: LHC layout. The red zones indicate the infrastructure additions to the LEP installations, built to accomodate the ATLAS and CMS experiments which exceed the size of the former experiments located there [61]. Bottom: LHC RF cavities. A module accomodates 4 cavities that accelerate protons and preserve the bunch structure of the beam. [65, 67]

999 LHC have a system of 16 RF cavities located in the so-called point 4, as shown in
1000 figure 3.4 top, tunned at a freqency of 400 MHz and the protons are carefully timed
1001 so additionally to the acceleration effect the bunch structure of the beam is preserved.
1002 Bottom side of figure 3.4 shows a picture of a Rf module composed of 4 RF cavities

1003 working in a superconducting state at 4.5 K; also is showed a representation of the
 1004 accelerating electric field that accelerates the protons in the bunch.

1005

1006 While protons are accelerated in one section of the LHC ring, where the RF cavities
 1007 are located, in the rest of their path they have to be kept in the curved trajectory
 1008 defined by the LHC ring. Technically, LHC is not a perfect circle; RF, injection, beam
 1009 dumping, beam cleaning and sections before and after the experimental points where
 1010 protons collide are all straight sections. In total, there are 8 arcs 2.45 Km long each
 1011 and 8 straight sections 545 m long each. In order to curve the proton's trajectory in
 1012 the the arc sections, superconducting dipole magnets are used.

1013

1014 Inside the LHC ring, there are two proton beams traveling in opposite directions in
 1015 two separated beam pipes; the beam pipes are kept at ultra high vacuum ($\sim 10^{-9}$
 1016 Pa) to ensure that there are no particles that interact with the proton beams. The
 1017 superconducting dipole magnets used in LHC are made of a NbTi alloy, capable of
 1018 transporting currents of about 12000 A when cooled at a temperature below 2K using
 1019 liquid helium (see figure 3.5).

1020 Protons in the arc sections of LHC feel a centripetal force exerted by the dipole
 1021 magnets which is perpendicular to the beam trajectory; The magnitude of magnetic
 1022 field needed can be found assuming that protons travel at $v \approx c$, using the standard
 1023 values for proton mass and charge and the LHC radius, as

$$F_m = \frac{mv^2}{r} = qBv \quad \rightarrow B = 8.33T \quad (3.1)$$

1024 which is about 100000 times the Earth's magnetic field. A representation of the mag-
 1025 netic field generated by the dipole magnets is shown in the bottom left side of figure

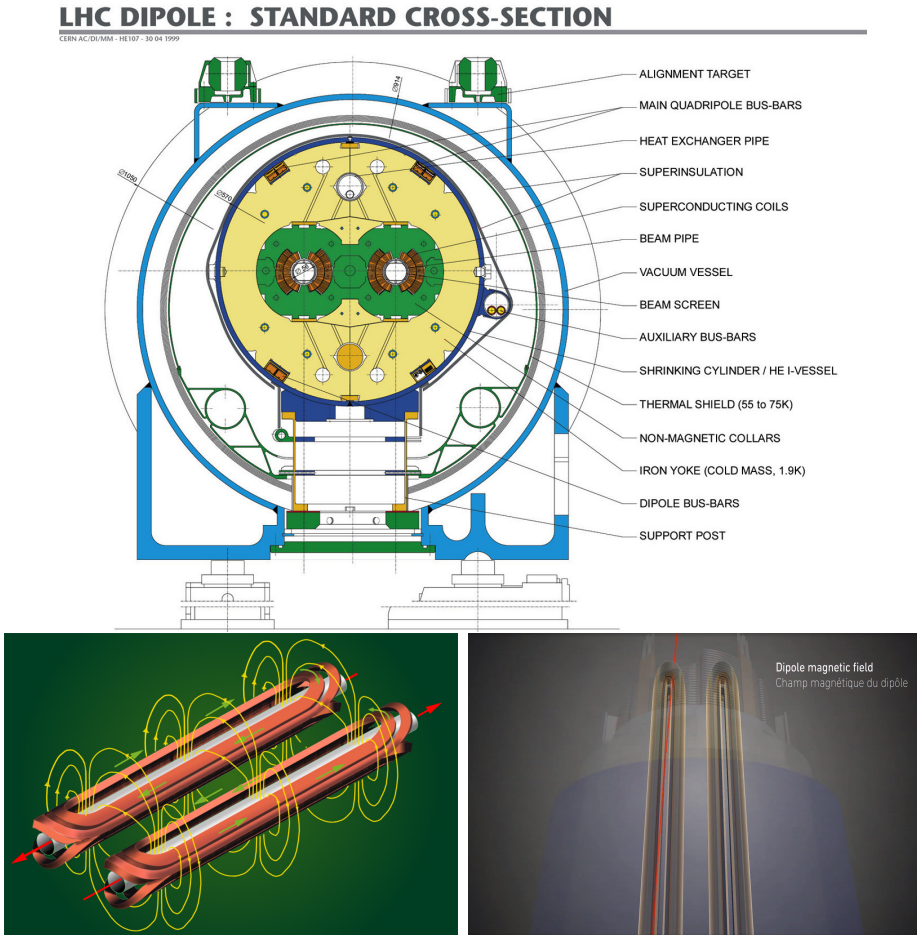


Figure 3.5: Top: LHC dipole magnet transversal view; cooling, shielding and mechanical support are indicated. Bottom left: Magnetic field generated by the dipole magnets; note that the direction of the field inside one beam pipe is opposite with respect to the other beam pipe which guarantee that both proton beams are curved in the same direction towards the center of the ring. The effect of the dipole magnetic field on the proton beam is represented in the bottom right side [65, 68, 69].

1026 3.5. The bending effect of the magnetic field on the proton beam is shown in the
 1027 bottom right side of figure 3.5. Note that the dipole magnets are not curved; the arc
 1028 section of the LHC ring is composed of straight dipole magnets of about 15 m. In
 1029 total there are 1232 dipole magnets along the LHC ring.
 1030 In addition to bending the beam trajectory, the beam has to be focused so it stays in
 1031 side the beam pipe. The focusing is performed by quadrupole magnets installed in

1032 another straight section; in total 858 quadrupole magnets are installed along the LHC
 1033 ring. Other effects like electromagnetic interaction among bunches, interaction with
 1034 electron clouds from the beam pipe, gravitational force on the protons, differences in
 1035 energy among protons in the same bunch, among others, are corrected using sextupole
 1036 and other magnetic multipoles.

1037 The two proton beams inside the LHC ring are made of bunches with a cylindrical
 1038 shape of about 7.5 cm long and about 1 mm in diameter; when bunches are close
 1039 to the collision point (CP), the beam is focused up to a diameter of about 16 μm
 1040 in order to maximize the luminosity (L) defined as the number of collisions per unit
 1041 area and per second. Luminosity can be calculated using

$$L = fn \frac{N_1 N_2}{4\pi\sigma_x\sigma_y} \quad (3.2)$$

1042 where f is the revolution frequency, n is the number of bunches per beam, N_1 and N_2
 1043 are the number of protons per bunch, σ_x and σ_y are the gaussian transverse sizes of
 1044 the bunches. Using

$$f = \frac{v}{2\pi r_{LHC}} \approx \frac{3 \times 10^8 \text{ m/s}}{27 \text{ km}} \approx 11.1 \text{ kHz},$$

$$n = 2808$$

$$N_1 = N_2 = 1.5 \times 10^{11}$$

$$\sigma_x = \sigma_y = 16 \mu\text{m}$$

1045

$$L = 1.28 \times 10^{34} \text{ cm}^{-2} \text{ s}^{-1} \quad (3.3)$$

1046 Luminosity is a fundamental aspect for LHC given that the bigger luminosity, the
 1047 bigger number of collisions, which means that for processes with a very small cross

section the number of expected occurrences is increased and so the chances of being detected. The integrated luminosity collected by the CMS experiment during 2016 is shown in figure 3.6; the data analyzed in this thesis corresponds to an integrated luminosity of 35.9 fb^{-1} at $\sqrt{s} = 13 \text{ TeV}$.

A way to increase L is increasing the number of bunches in the beam. Currently, the separation between two consecutive bunches in the beam is 7.5 m which corresponds to a time separation of 25 ns. In the full LHC ring the allowed number of bunches is $n = 27\text{km}/7.5\text{m} = 3600$; however, there are some gaps in the bunch pattern intended for preparing the dumping and injection of the beam, thus, the proton beams are composed of 2808 bunches.

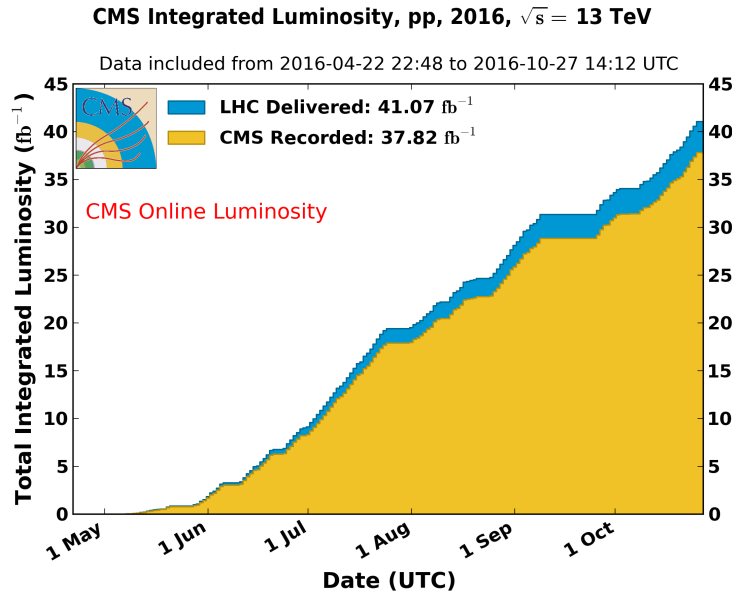


Figure 3.6: Integrated luminosity delivered by LHC and recorded by CMS during 2016. The difference between the delivered and the recorded luminosities is due to fails and issues occurred during the data taking in the CMS experiment [70].

Once the proton beams reach the desired energy, they are brought to cross each other producing proton-proton collisions. The bunch crossing happens in precise places where the four LHC experiments are located, as seen in figure 3.7 left. In 2008, the

1061 first set of collisions involved protons with $\sqrt{s} = 7$ TeV; the energy was increased to
 1062 8 TeV in 2012 and to 13 TeV in 2015.

1063 CMS and ATLAS experiments, which are multi-purpose experiments, are enabled
 1064 to explore physics in any of the collision modes. LHCb experiment is optimized
 1065 to explore bottom quark physics, while ALICE is optimized for heavy ion collisions
 1066 searches; TOTEM and LHCf are dedicated to forward physics studies; MoEDAL (not
 1067 indicated in the figure) is intended for monopoles or massive pseudo stable particles
 1068 searches.

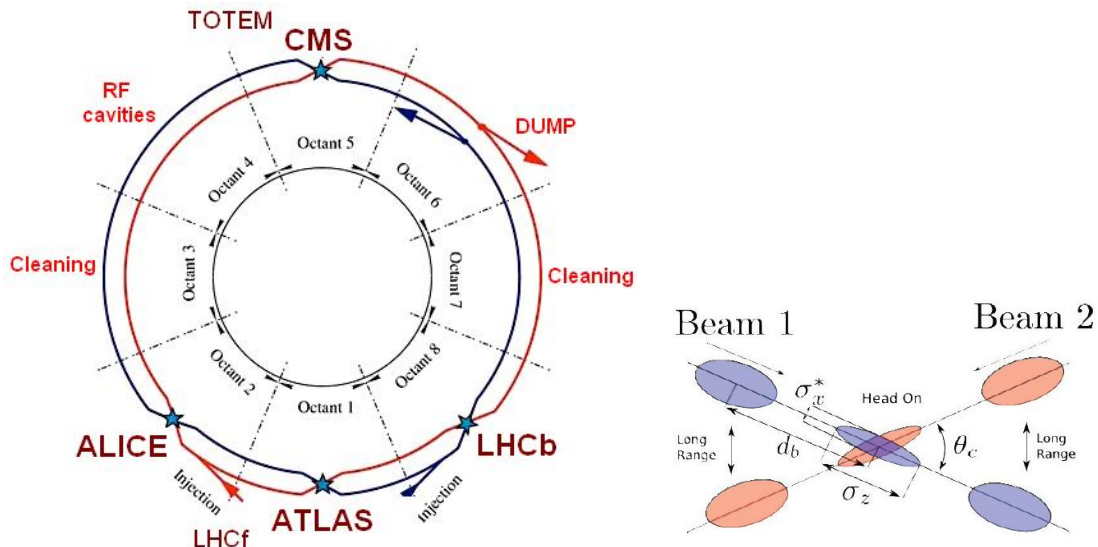


Figure 3.7: Left: LHC interaction points. Bunch crossing occurs where the LHC experiments are located [71]. Sections indicated as cleaning are dedicated to collimate the beam in order to protect the LHC ring from collisions with protons in very spreaded bunches. Right: bunch crossing scheme. Since the bunch crossing is not perfectly head-on, the luminosity is reduced in a factor of 17%.

1069 At the CP there are two interesting details that need to be addressed. The first
 1070 one is that the bunch crossing does not occur head-on but at a small crossing angle
 1071 (280 μ rad in CMS and ATLAS) as shown in the right side of figure 3.7, affecting the
 1072 overlapping between bunches; the consequence is a reduction of about 17% in the
 1073 luminosity. The second one is occurrence of multiple pp collisions in the same bunch

1074 crossing; this effect is called pile-up (PU). A fairly simple estimation of the PU follows
 1075 from estimating the probability of collision between two protons, one from each of
 1076 the bunches in course of collision; it depends roughly on the ratio of proton size and
 1077 the cross section of the bunch in the interaction point, i.e.,

$$P(pp\text{-}collision) \sim \frac{d_{proton}^2}{\sigma_x \sigma_y} = \frac{(1fm)^2}{(16\mu m)^2} \sim 4 \times 10^{-21} \quad (3.4)$$

1078 however, there are $N = 1.15 \times 10^{11}$ protons in a bunch, thus the estimated number of
 1079 collisions in a bunch crossing is

$$PU = N^2 * P(pp\text{-}collision) \sim 50 \text{ pp-collision per bunch crossing}, \quad (3.5)$$

1080 about 20 of those pp collisions are inelastic. Each collision generates a vertex, but
 1081 only the most energetic is considered as a primary vertex; the rest are considered
 1082 as PU vertices. A simulation of a multiple pp collision event in a bunch crossing at
 1083 CMS is showed in figure3.8. Unstable particles outgoing from the primary vertex will
 1084 eventually decay; this decay vertex is known as a secondary vertex.

1085 When the beams are exhausted, i.e. the number of protons in the bunches is reduced
 1086 beyond a limit, or in case of emergency, the beams have to be extracted from the
 1087 beam pipes; the dumping system, in the dump section, perform the extraction safely
 1088 by directing the beams towards graphite blocks that absorb the beam energy.

1089

1090 Next section present a description of the CMS detector, since it is the detector used
 1091 to collect the data used in this thesis.

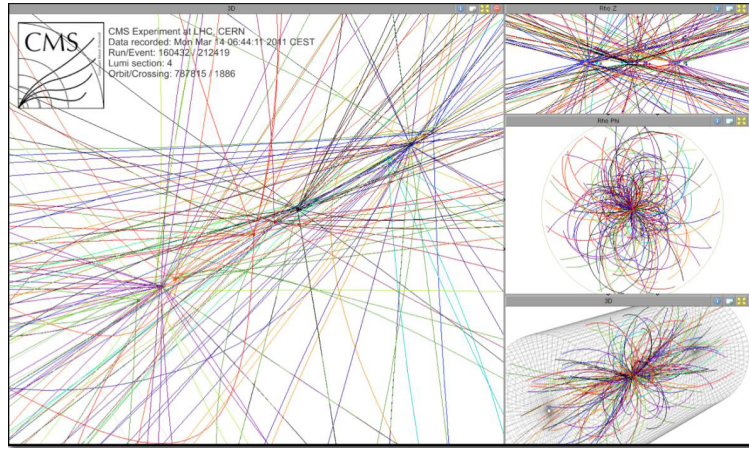


Figure 3.8: Multiple pp collision bunch crossing at CMS. Only the most energetic vertex is considered and the rets are cataloged as PU vertices [].

1092 3.3 The CMS experiment

1093 CMS is a general purpose detector designed to conduct research in a wide range of
 1094 physics from standard model to new physics like extra dimensions and dark matter.
 1095 Located at the point 5 in the LHC layout as shown in figure 3.4, CMS is composed
 1096 of several detection systems distributed in a cylindrical structure,. In total, CMS
 1097 weights about 12500 tons in a very compact 21.6 m long and 14.6 m diameter cylin-
 1098 der. It was built in 15 separate sections at the ground level and lowered to the
 1099 cavern individually to be assembled. A complete and detailed description of the CMS
 1100 detector and its components is given in reference [72] on which this section is based in.
 1101

1102 Figure 3.9 shows the layout of the CMS detector. The design is driven by the require-
 1103 ments on the identification, momentum resolution and unambiguous charge determi-
 1104 nation of the muons; therefore, a large bending power is provided by the solenoid
 1105 magnet made of superconducting cable capable to generate a 3.8 T magnetic field.
 1106 The detection system is composed of (from the innermost to the outermost)

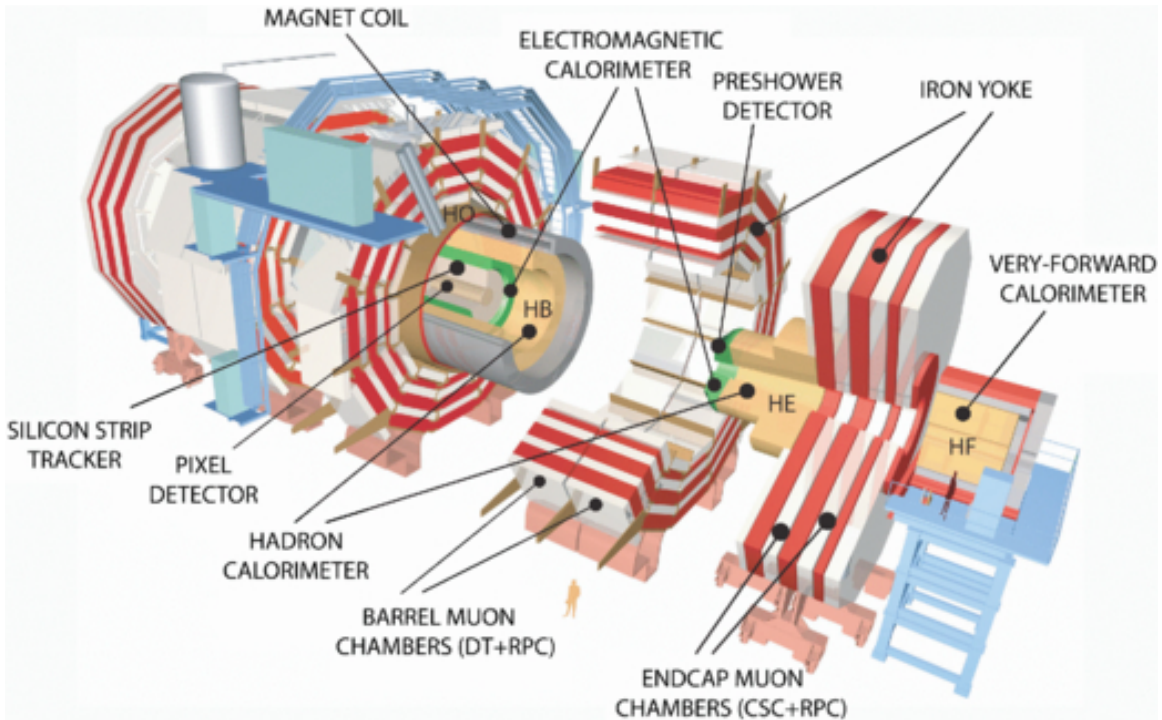


Figure 3.9: CMS detector drawing. The several subdetectors are indicated. The central region of the detector is referred as the Barrel section while the endcaps are referred as the forward sections. [73].

- 1107 • Pixel detector.
 - 1108 • Silicon strip tracker.
 - 1109 • Preshwoer detector.
 - 1110 • Electromagnetic calorimeter.
 - 1111 • Hadronic calorimeter.
 - 1112 • Muon chambers (Barrel and endcap)
- 1113 The central region of the detector is commonly referred as the barrel section while the
 1114 endcaps are referred as the forward sections of the detector; thus, each subdetector
 1115 is composed of a barrel section and a forward section.

1116 3.3.1 Coordinate system

1117 The coordinate system used by CMS is centered in the geometrical center of the
 1118 detector which is the same as the CP as shown in figure3.10. The z -axis is parallel
 1119 to the beam direction, while the Y -axis pointing vertically upward, and the X -axis
 1120 pointing radially inward toward the center of the LHC.

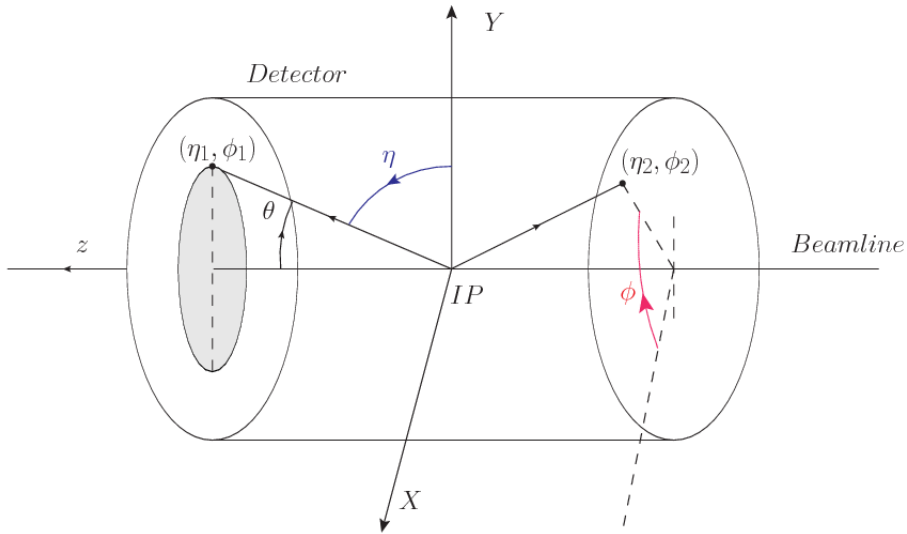


Figure 3.10: CMS coordinate system.

1121 In addition to the common cartesian and cylindrical coordinate systems, two coordi-
 1122 nates are of particular utility in particle physics: rapidity(y) and pseudorapidity(η),
 1123 defined in connection to the polar angle θ , energy and longitudinal momentum com-
 1124 ponent (momentum along the z -axis) according to

$$y = \frac{1}{2} \ln \frac{E + p_z}{E - p_z} \quad \eta = -\ln \left(\tan \frac{\theta}{2} \right) \quad (3.6)$$

1125 Rapidity is related to the angle between the XY -plane and the direction in which
 1126 the products of a collision are emitted; it has the nice property that the difference
 1127 between the rapidities of two particles is invariant with respect to Lorentz boosts
 1128 along the z -axis. Thus, data analysis becomes more simple when based in rapidity;

however, it is not simple to measure the rapidity of highly relativistic particles, as those produced after pp collisions. Under the highly relativistic motion approximation y can be rewritten in terms of the polar angle, arriving to the conclusion that rapidity is approximately equal to the pseudorapidity defined above, i.e. $y \approx \eta$. Note that η is easier to measure than y given the direct relationship between the former and the polar angle. Angular distance between two objects in the detector (ΔR) is defined in terms of their coordinates $(\eta_1, \phi_1), (\eta_2, \phi_2)$ as

$$\Delta R = \sqrt{(\Delta\eta)^2 - (\Delta\phi)^2} \quad (3.7)$$

3.3.2 Pixels detector

The CMS tracking system is designed to provide a precise measurement of the trajectory followed by the charged particles created after the pp collisions as; also, the precise reconstruction of the primary and secondary vertices is expected in an environment where, each 25 ns, the bunch crossing produce about 20 inelastic collisions and about 1000 particles. An increment in the luminosity is ongoing which implies that the PU will increase accordingly.

1143

The pixel detector was replaced during the 2016-2017 year end shut down, due to the increasingly challenging operation conditions like the higher particle flow and more radiation harsh environment among others. The new one is responding as expected, reinforcing its crucial role in the successful way to fulfil the new LHC physics objectives after the discovery of the Higgs boson. The last chapter of this thesis is dedicated to describe my contribution to the “Forward Pixel Phase 1 upgrade”.

1150

1151 The current pixel detector is composed of 1856 silicon pixel detector modules orga-
 1152 nized in four barrel layers in the central region and three disks in the forward region;
 1153 it is designed to record efficiently and with high precision, up to $10\mu\text{m}$ in the XY -
 1154 plane and $20\mu\text{m}$ in the z -direction, the first four space-points near to the CP region
 1155 (see figure 3.11 left side) in the range $|\eta| \leq 2.5$. The first barrel layer is located at a
 1156 radius of 30 mm from the beamline, while the fourth layer is located at a radius of
 1157 160 mm closer to the strip tracker inner barrel layer (see section 3.3.3) in order to
 1158 reduce the rate of fake tracks. The high granularity of the detector is represented in
 1159 its about 123 Mpixels, each of size $100 \times 150\mu\text{m}^2$, which is almost twice the channels
 1160 of the old detector. The transverse momentum resolution of tracks can be measured
 1161 with a resolution of 1-2% for muons of $p_T = 100$ GeV.

1162

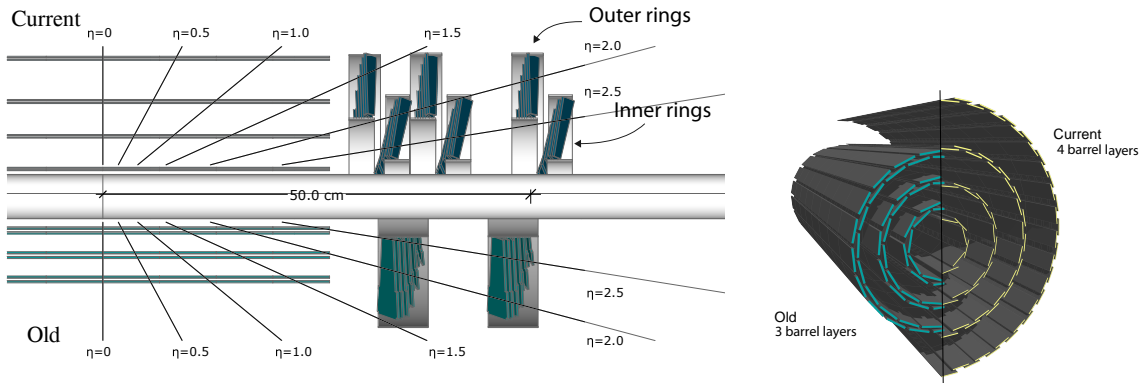


Figure 3.11: CMS pixel detector schematic view. Left: layout comparing the layers and disks in the old and current pixel detectors. Right: Transverse-oblique view comparing the pixel barrel layers in the two [75].

1163 Some of the improvements with respect to the previous pixel detector include a higher
 1164 average tracking efficiency and lower average fake rate as well as higher track impact
 1165 parameter resolution which is fundamental in order to increase the efficiency in the
 1166 identification of jets originating from b quarks (b-tagging). A significant source of

improvement comes from the overall reduction in the material budget of the detector which results in less photon conversions and less multiple scattering from charged particles.

3.3.3 Silicon strip tracker

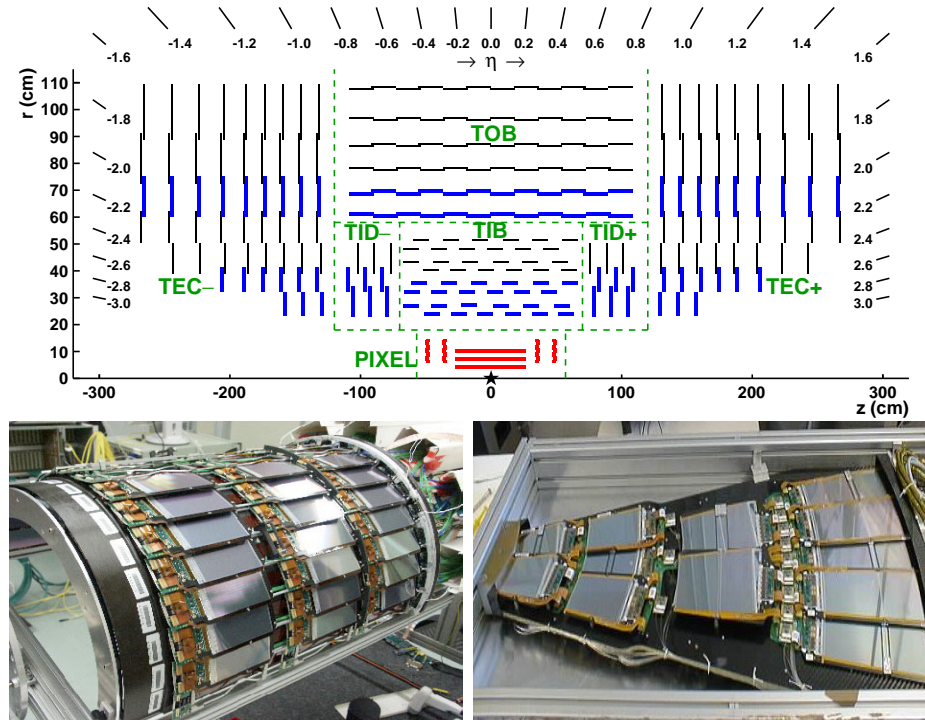


Figure 3.12: Top: CMS Silicon Strip Tracker (SST) schematic view. The SST is composed of the tracker inner barrel (TIB), the tracker inner disks (TID), the tracker outer barrel (TOB) and the tracker endcaps (TEC). Each part is made of silicon strip modules; the modules in blue represent two modules mounted back-to-back and rotated in the plane of the module by a stereo angle of 120 mrad in order to provide a 3-D reconstruction of the hit positions. Bottom: pictures of the TIB (left) and TEC (right) modules [76–78].

The silicon strip tracker (SST) is the second stage in the CMS tracking system . The top side of figure 3.12 shows a schematic of the SST. The inner tracker region is composed of the tracker inner barrel (TIB) and the tracker inner disks (TID) covering the region $r < 55$ cm and $|z| < 118$ cm. The TIB is composed of 4 layers while the TID

1175 is composed of 3 disks at each end. The silicon sensors in the inner tracker are 320
1176 μm thick, providing a resolution of about 13-38 μm in the $r\phi$ position measurement.

1177

1178 The modules indicated in blue in the schematic view of figure 3.12 are two modules
1179 mounted back-to-back and rotated in the plane of the module by a “stereo” angle of
1180 100 mrad; the hits from these two modules, known as “stereo hits”, are combined to
1181 provide a measurement of the second coordinate (z in the barrel and r on the disks)
1182 allowing the reconstruction of hit positions in 3-D.

1183

1184 The outer tracker region is composed of the tracker outer barrel (TOB) and the
1185 tracker endcaps (TEC). The 6 layers of the TOB offers coverage in the region $r > 55$
1186 cm and $|z| < 118$ cm, while the 9 disks of the TEC cover the region $124 < |z| < 282$
1187 cm. The resolution offered by the outer tracker is about 13-38 μm in the $r\phi$ position
1188 measurement. The inner four TEC disks use silicon sensors 320 μm thick; those in
1189 the TOB and the outer three TEC disks use silicon sensors of 500 μm thickness. The
1190 silicon strips run parallel to the z -axis and the distance between strips varies from 80
1191 μm in the inner TIB layers to 183 μm in the inner TOB layers; in the endcaps the
1192 wedge-shaped sensors with radial strips, whose pitch range between 81 μm at small
1193 radii and 205 μm at large radii.

1194

1195 The whole SST has 15148 silicon modules, 9.3 million silicon strips and cover a total
1196 active area of about 198 m^2

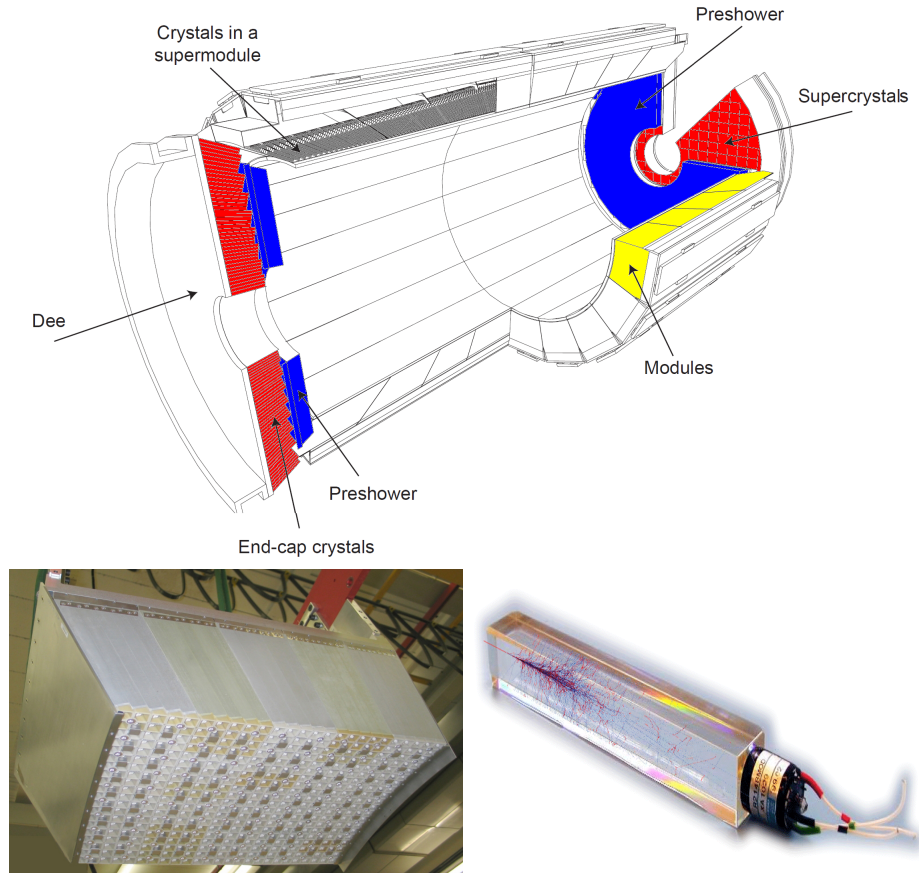


Figure 3.13: Top: CMS ECAL schematic view. Bottom: Module equipped with the crystals (left); ECAL crystal(right).

1197 3.3.4 Electromagnetic calorimeter

1198 The CMS electromagnetic calorimeter (ECAL) is designed to measure the energy of
 1199 electrons and photons. It is composed of 75848 lead tungstate crystals which has a
 1200 short radiation length (0.89 cm) and fast response given that 80% of the light is em-
 1201 mited within 25 ns; however, they are combined with Avalanche photodiodes (APDs)
 1202 as photodetectors given that crytals themself have a low light yield ($30\gamma/\text{MeV}$). An
 1203 schematic view of the ECAL is shown in figure 3.13.

1204

1205 Energy is measured by absorbing electrons and photons which generates an elec-

1206 electromagnetic “shower”, as seen in bottom right picture of the figure3.13. The ECAL
 1207 barrel (EB) cover the region $|\eta| < 1.479$, using crystals of depth of 23 cm and 2.2×2.2
 1208 cm^2 transverse section.

1209 The ECAL endcap (EE) cover the region $1.479 < |\eta| < 3.0$ using crystals of depth
 1210 22 cm and transverse section of $2.86 \times 2.86 \text{ cm}^2$; the photodetectors used are vacuum
 1211 phototriodes (VPTs). Each EE is divided in two structures called “Dees”.

1212

1213 In front of the EE, it is installed the preshower detector (ES) which covers the region
 1214 $1.653 < |\eta| < 2.6$. The ES provides a precise measurement of the position of electro-
 1215 magnetic showers, which allows to distinguish electrons and photons signals from π^0
 1216 decay signals. The ES is composed of a layer of lead absorber followed by a layer of
 1217 plastic scintillators

1218 **3.3.5 Hadronic calorimeter**

1219 Hadrons are not absorbed by the ECAL but by the hadron calorimeter (HCAL),
 1220 which is made of a combination of alternating brass absorber and silicon photo-
 1221 multiplier(SiPM) layers; therefore, particles passing through the scintillator material
 1222 produce showers, as in the ECAL, as a result of the inelastic scattering of the hadrons
 1223 with the detector material. Since the particles are not absorbed in the scintillator,
 1224 their energy is sampled; therefore the total energy is not measured but stimated,
 1225 which reduce the resolution of the detector. Brass was choosen as the absorber mate-
 1226 rial due to its short interaction lenght ($\lambda_I = 16.42\text{cm}$) and its non-magnetivity. Figure
 1227 3.14 shows an schematic view of the CMS HCAL.

1228

1229 The HCAL is divided in four sections; the Hadron Barrel (HB), the Hadron Outer

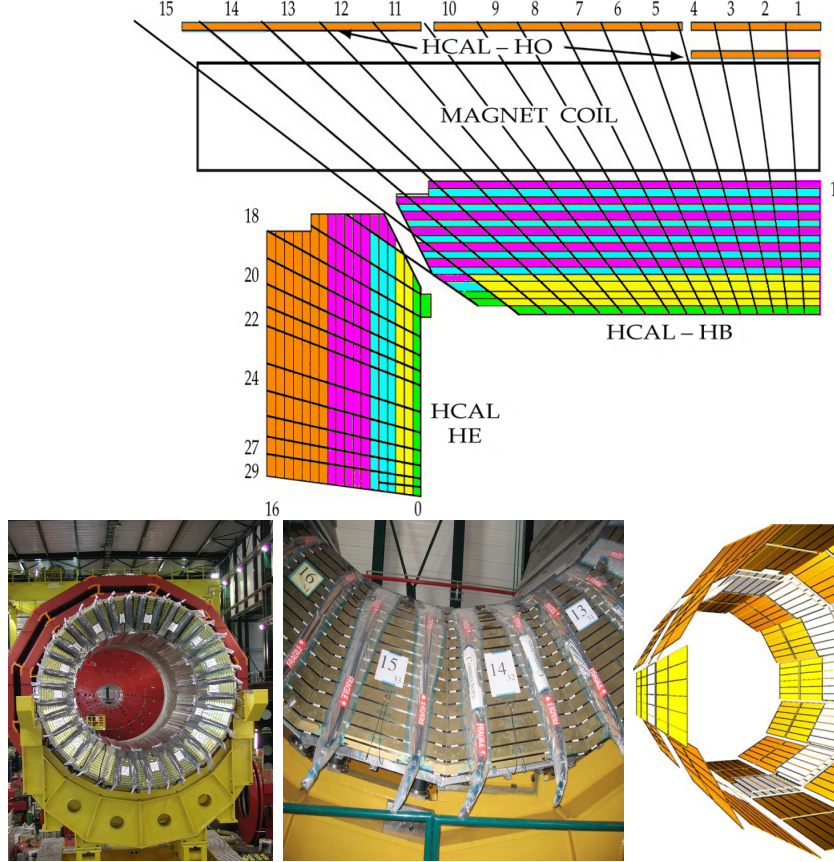


Figure 3.14: Top: CMS HCAL schematic view, the colors indicate the layers that are grouped into the same readout channels. Bottom: picture of a section of the HB; the absorber material is the golden region and scintillators are placed in between the absorber material (left and center). Schematic view of the HO (right). [79, 80]

1230 (HO), the Hadron Endcap (HE) and the Hadron Forward (HF) sections. The HB
 1231 cover the region $0 < |\eta| < 1.4$, while the HE covers the region $1.3 < |\eta| < 3.0$. The HF,
 1232 made of quartz fiber scintillator and steel as absorption material, covers the forward
 1233 region $3.0 < |\eta| < 5.2$. Both the HB and HF are located inside the solenoid. The HO
 1234 is placed outside the magnet as an additional layer of scintillators with the purpose
 1235 of measure the energy tails of particles passing through the HB and the magnet
 1236 (see figure 3.14 top and bottom right) . The upgrades made to the HCAL during
 1237 the technical stop 2016-2017 consisted in the replacement of the phototransducers,

1238 improving the efficiency.

1239 **3.3.6 Superconducting solenoid magnet**

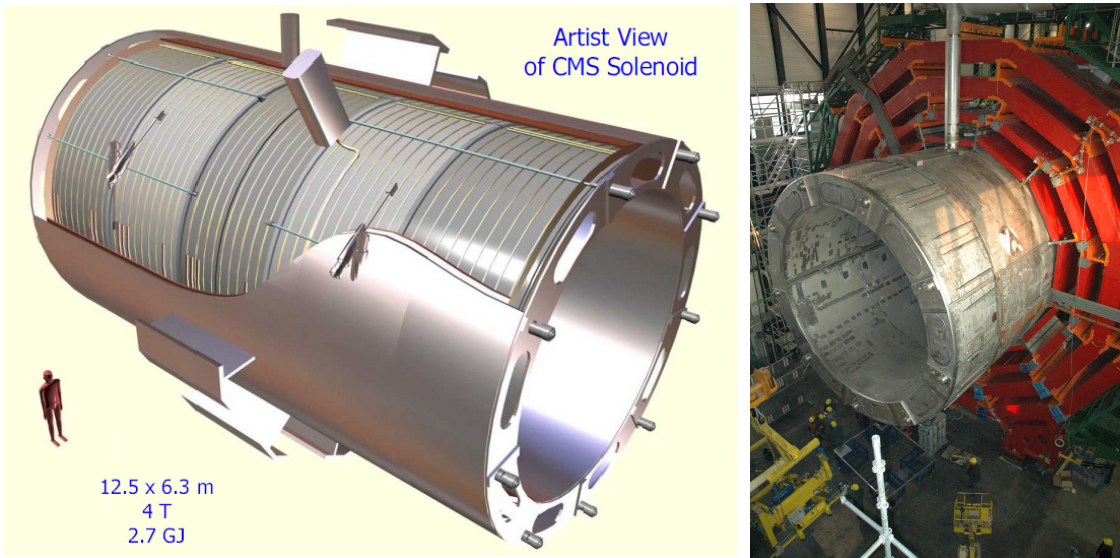


Figure 3.15: Artistic representation of the CMS solenoid magnet(left). The magnet is supported on an iron yoke (right) which also serves as the house of the muon detector and as mechanical support for the whole CMS detector [74].

1240 The superconducting magnet installed is the CMS detector is designed to provide an
 1241 intense and highly uniform magnetic field in the central part of the detector. In fact,
 1242 the tracking system takes advantage of the bending power of the magnetic field to
 1243 measure with precision the momentum of the particles that traverse it; the unam-
 1244 biguous determination of the sign for high momentum muons was a driven principle
 1245 during the design of the magnet. The magnet has a diameter of 6.3 m, a length of
 1246 12.5 m in a cold mass of 220 t; the generated magnetic field reach a strength of 3.8T.
 1247 Since it is made of Ni-Tb superconducting cable it has to operate at a temperature
 1248 of 4.7 K by using a helium cryogenic system; the current circulating in the cables
 1249 reach 18800 A under normal running conditions. The left side of figure 3.15 shows
 1250 an artistic view of the CMS magnet, while the right side shows a transverse view of

1251 the cold mass where the winding structure is visible.

1252

1253 The yoke (see figure 3.15), composed of 5 barrel wheels and 6 endcap disks made
 1254 of iron, serves not only as the media for magnetic flux return, but also provides the
 1255 house for the muon detector system and structural stability to the full detector.

1256 **3.3.7 Muon system**

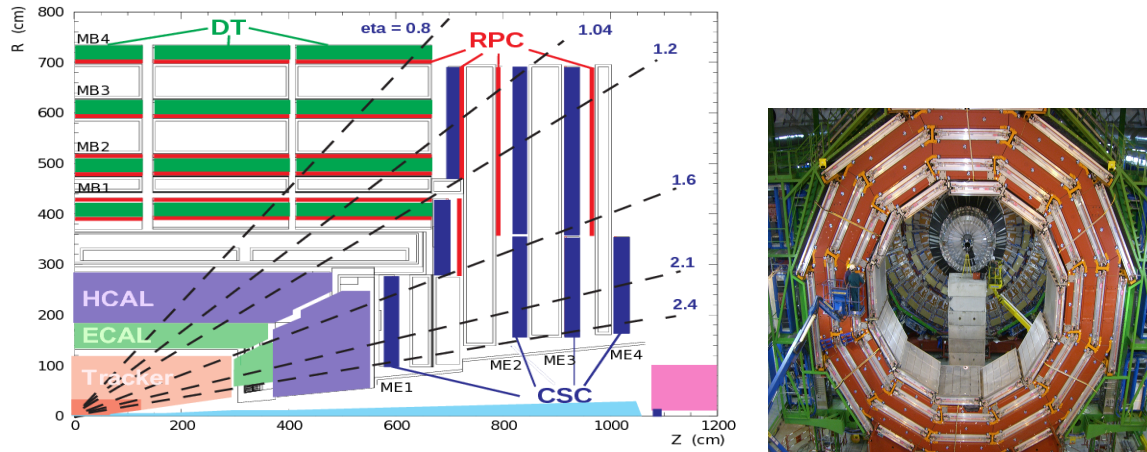


Figure 3.16: Left: CMS muon system schematic view; Right: one of the yoke rings with the muon DTs and RPCs installed; in the back it is possible to see the muon endcap [81].

1257 Muons are the only charged particles able pass through all the CMS detector due to
 1258 their low ionization energy loss; thus, muons can be separated easily from the high
 1259 amount of particles produced in a pp collision. Also, muons are expected to be pro-
 1260 duced in the decay of several new particles; therefore, a good detection of muons was
 1261 on the leading principles when designing the CMS detector.

1262

1263 The CMS muon detection system is embedded in the return yoke as seen in figure
 1264 3.16. It is composed of three different detector types; the drift tube chambers (DT)
 1265 are located in the central region $\eta < 1.2$ arranged in four layers of drift chambers filled

1266 with an Ar/CO₂ gas mixture.

1267

1268 The muon endcaps are made of Cathode strip chambers (CSC) covering the region
1269 $\eta < 2.4$ and filled with a mixture of Ar/CO₂/CF₄. The reason behind using a different
1270 detector type lies on the different conditions in the forward region like the high muon
1271 rate and high residual magnetic field.

1272

1273 The third type of detector used in the muon system is a set four disks of resistive
1274 plate chambers (RPC) working in avalanche mode. The RPCs provide good spatial
1275 and time resolutions. The track of $high - p_T$ muon candidate is build combining
1276 information from the tracking system and the signal from up to 6 RPCs and 4 DT
1277 chambers.

1278 **3.3.8 CMS trigger system**

1279 Under normal conditions, CMS expect pp collisions every 25 ns i.e. an interaction
1280 rate of 40 MHz for which it is not possible to store the recorded data in full. In order
1281 to handle this high event rate data, an online event selection, known as triggering, is
1282 performed; triggering reduce the event rate to 100 Hz for storage and further offline
1283 analysis.

1284

1285 The trigger system starts with a reduction of the event rate to 100 kHz in the so-called
1286 “level 1 trigger (L1)”. L1 is based on dedicated programmable hardware like Field
1287 Programmable Gate Arrays (FPGAs) and Application Specific Integrated Circuits
1288 (ASICs), partly located in the detector itself; other portion it located in the CMS
1289 under-ground cavern. Hit patterns information from the muon chambers and the

1290 energy deposits in the calorimeter are used to decide if an event is accepted or rejected,
 1291 according to selection requirements previously defined which reflect the interesting
 1292 physics processes. Figure 3.17 shows the L1 trigger architecture

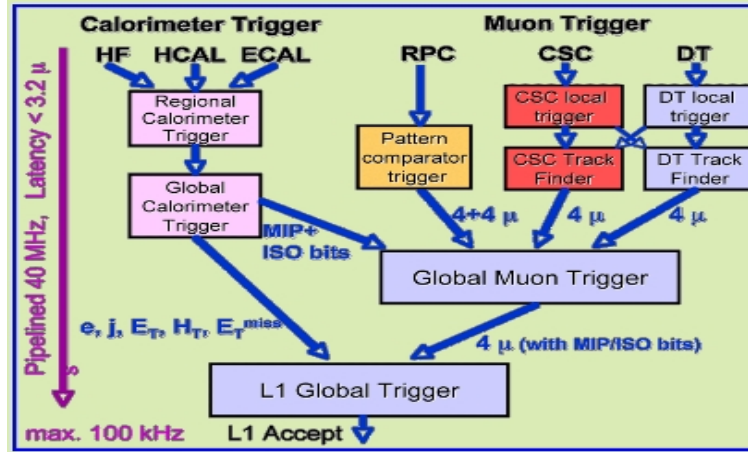


Figure 3.17: CMS Level-1 trigger architecture [82].

1293 The second stage in the trigger system is called “high level trigger (HLT)”; events
 1294 accepted by L1 are passed to HLT in order to make an initial reconstruction of them.

1295 HLT is software based and runs on a dedicated server farm, using selection algo-
 1296 rithms and high level object definitions; the event rate at HLT is reduced to 100 Hz.

1297 The first HLT stage takes information from the muon detectors and the calorimeters
 1298 to make the initial object reconstruction; in the next HLT stage, information from
 1299 the pixel and strip detectors is used to do first fast tracking and then full tracking
 1300 online. This initial object reconstruction is used in further steps of the trigger system.

1301

1302 Events and preliminary reconstructed physics objects from HLT are sent to be fully
 1303 reconstructed at the CERN computing center. Again, the pixel detector information
 1304 provides high quality seeds for the track reconstruction algorithm offline, primary ver-
 1305 tex reconstruction, electron and photon identification, muon reconstruction, τ iden-
 1306 tification and b-tagging. After full reconstruction, data sets are made available for

1307 offline analyses.

1308

1309 During the 2016-2017 technical stop, the L1 system was updated in order to improve
 1310 the physics object identification by improving the algorithms and accounting for the
 1311 increasing pile-up scenario.

1312 **3.3.9 CMS computing**

1313 After the data, coming from the experiment, are processed at several levels, they have
 1314 to be stored and made available for further analysis; in order to cope all the tasks
 1315 implied in the offline data processing, like transfer, simulation, reconstruction and
 1316 reprocessing, among others, a big computing power is required. The CMS computing
 1317 system is based in the distributed architecture concept, where users of the system
 1318 and physical computer centers are distributed worldwide and interconnected by high-
 1319 speed networks.

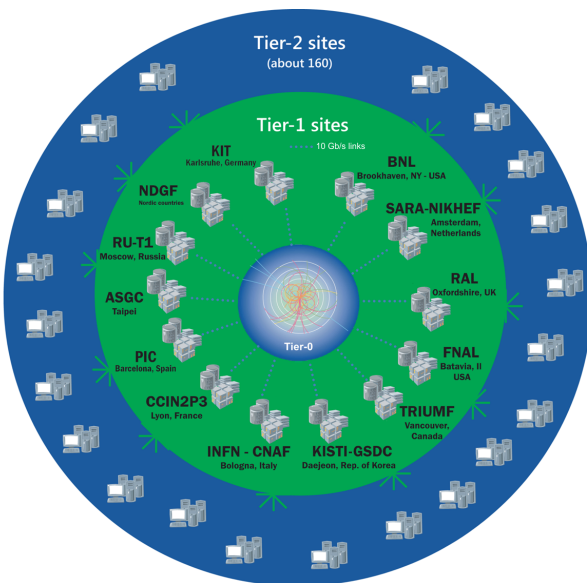


Figure 3.18: WLCG structure. The primary computer centers (Tier-0) are located at CERN (data center) and at the Wigner datacenter in Budapest. Tier-1 is composed of 13 centers and Tier-2 is composed of about 160 centers. [83].

1320 The worldwide LHC computing grid (WLCG) is the mechanism used to provide that
1321 distributed environment. WLCG is a tiered structure connecting computing centers
1322 around the world, which provide the necessary storage and computing facilities. The
1323 primary computing centers of the WLCG are located at the CERN and the Wigner
1324 datacenter in Budapest and are known as Tier-0 as shown in figure 3.18. The main
1325 responsibilities for each tier level are [83]

- 1326 • **Tier-0:** initial reconstruction of recorded events and storage of the resulting
1327 datasets, the distribution of raw data to the Tier-1 centers.
- 1328 • **Tier-1:** provide storage capacity, support for the Grid, safe-keeping of a pro-
1329 portional share of raw and reconstructed data, large-scale reprocessing and safe-
1330 keeping of corresponding output, generation of simulated events, distribution
1331 of data to Tier 2s, safe-keeping of a share of simulated data produced at these
1332 Tier 2s.
- 1333 • **Tier-2:** store sufficient data and provide adequate computing power for specific
1334 analysis tasks, provide analysis requirements and proportional share of simu-
1335 lated event production and reconstruction.

1336 Aside of the general computing strategy to manage the huge amount of data produced
1337 by experiments, CMS uses a framework to perform a variety of processing, selection
1338 and analysis tasks. The central concept of the CMS data model is the “Event”; there-
1339 fore, an event is the unit that contains the information from a single bunch crossing
1340 as well as any data derived from that information like the reconstructed objects, the
1341 details under which additional data are derived.

1342

1343 Events are passed as the input to the “physics modules” that obtain information from
1344 them and create new one; for instance, “event data producers” add new data into the
1345 events, “analizers” produce a information summary from an event set, “filters” per-
1346 form selection and triggering.

1347

1348 CMS uses several event formats with different levels of detail and precision

1349 • **Raw format:** events in this format contain the full recorded information from
1350 the detector as well as trigger decision and other metadata. An extended version
1351 of raw data is used to store information from the CMS Monte Carlo simulation
1352 tools. Raw data are stored permanently, occupying about 2MB/event

1353 • **RECO format:** events in this format correspond to raw data that have been
1354 submitted to reconstruction algorithms like primary and secondary vertex re-
1355 construction, particle ID, track-finding. RECO events contain physical objects
1356 and all the information used to reconstruct them; average size is about 0.5
1357 MB/event.

1358 • **AOD format:** Analysis Object Data (AOD) is the data format used in the
1359 physics analyses given that it contains the parameters describing the high-level
1360 physics objects in addition to enough information to allow a kinematic refitting
1361 if needed. AOD events are filtered versions of the RECO events to which skim-
1362 ming or other kind processes have been applied. Requires about 100 kB/event.

1363 • **Non-event data** are data needed to interpret and reconstruct events. Some
1364 of the non-event data used by CMS contains information about the detector
1365 contraction and condition data like calibrations, alignment and detector status.

1366 Figure 3.19 shows the dataflow scheme between CMS detector and hardware tiers.

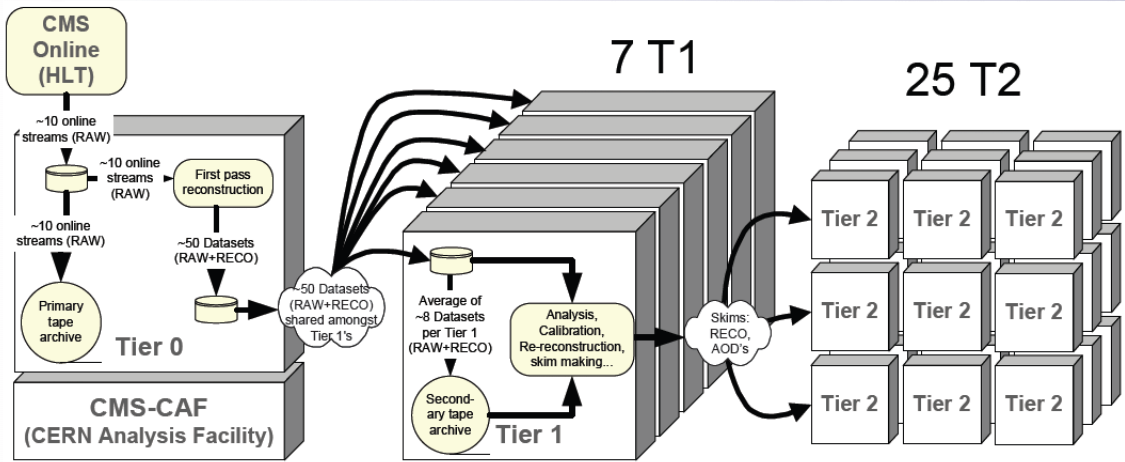


Figure 3.19: Detector data flow through hardware Tiers.

1367 **3.4 Event generation simulation and**
1368 **reconstruction**

1369 **3.4.1 event generation**

1370 **3.4.2 Hard scattering**

1371 **3.4.3 parton shower**

1372 **3.4.4 hadronization and decays**

1373 **3.4.5 underlying events and pileup**

1374 **3.4.6 MC - MadEvent, MadGraph and madgraphNLO,**
1375 **powheg, pythia, tauola**

1376 **3.4.7 detector simulation**

1377 **3.4.8 event reconstruction- particle flow algorithm,**
1378 **vertexing , muon reco, electron reco, photon and**
1379 **hadron reco, jets reco, anti-kt algoritm, jet energy**
1380 **corrections, btagging, MET**

1381 **3.4.9 MVA methods, NN, BDT, boosting, overtraining,**
1382 **variable ranking**

1383 **3.4.10 statistical inference, likelihood parametrization**

1384 **3.4.11 nuisance paraeters**

1385 **3.4.12 exclusion limits**

1386 **3.4.13 asymptotic limits**

¹³⁸⁷ **Chapter 4**

¹³⁸⁸ **Search for production of a Higgs**

¹³⁸⁹ **boson and a single top quark in**

¹³⁹⁰ **multilepton final states in pp**

¹³⁹¹ **collisions at $\sqrt{s} = 13$ TeV**

¹³⁹² **4.1 Introduction**

¹³⁹³ Dont forget to mention previous constrains to ct check reference ?? and references

¹³⁹⁴ <https://link.springer.com/content/pdf/10.1007%2FJHEP01>

¹³⁹⁵ A. Azatov, R. Contino and J. Galloway, \rightarrow Model-Independent Bounds on a

¹³⁹⁶ Light Higgs, \rightarrow JHEP 1204 (2012) 127 [arXiv:1202.3415 [hep-ph]].

¹³⁹⁷ J. R. Espinosa, C. Grojean, M. Muhlleitner and M. Trott, \rightarrow Fingerprinting

¹³⁹⁸ Higgs Suspects at the LHC, \rightarrow JHEP 1205 (2012) 097 [arXiv:1202.3697 [hep-ph]].

¹³⁹⁹ This chapter present the search for the associated production of a Higgs boson and

¹⁴⁰⁰ a single top quark events with three leptons in the final state, targeting Higgs decay

modes to WW , ZZ , and $\tau\tau$. The analysis uses the 13 TeV dataset produced in 2016, corresponding to an integrated luminosity of 35.9fb^{-1} . It is based on and expands previous analyses at 8 TeV [84, 85] and searches for associated production of $t\bar{t}$ and Higgs in the same channel [86], and complements searches in other decay channels targeting $H \rightarrow b\bar{b}$ [87].
 As showed in section 2.4, the cross section of the associated production of a Higgs boson and a single top quark (tHq) process is driven by a destructive interference of two contributions (see Figure 4.1), where the Higgs couples to either the W boson or the top quark. Any deviation from the standard model (SM) in the Higgs coupling structure could therefore lead to a large enhancement of the cross section, making this analysis sensitive to such deviations. A second process, where the Higgs and top quark are accompanied by a W boson (tHW) has similar behavior, albeit with a weaker interference pattern.

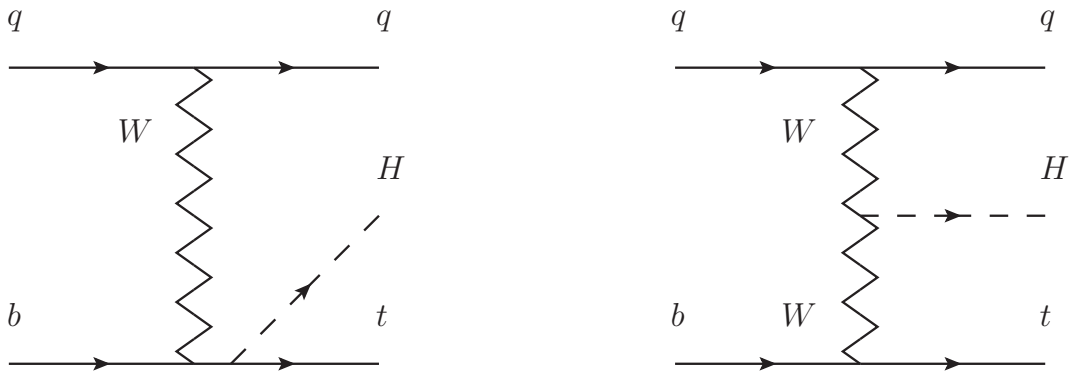


Figure 4.1: The two leading-order diagrams of tHq production.

We selects events with three leptons and a b tagged jet in the final state. The tHq signal contribution is then determined in a fit of the observed data to two multivariate classifier outputs, each trained to discriminate against one of the two dominant backgrounds of events with non-prompt leptons from $t\bar{t}$ and of associated production of $t\bar{t}$

1418 and vector bosons ($t\bar{t}W$, $t\bar{t}Z$). The fit result is then used to set an upper limit on the
 1419 combined $t\bar{t}H$, tHq and tHW production cross section, as a function of the relative
 1420 coupling strengths of Higgs and top quark and Higgs and W boson, respectively.

1421 4.2 Data and MC Samples

1422 The data considered in this analysis were collected by the CMS experiment dur-
 1423 ing 2016 and correspond to a total integrated luminosity of 35.9fb^{-1} . Only periods
 1424 when the CMS magnet was on were considered when selecting the data samples, that
 1425 corresponds to the 23 Sep 2016 (Run B to G) and PromptReco (Run H) versions
 1426 of the datasets. The MC samples used in this analysis correspond to the RunI-
 1427 ISummer16MiniAODv2 campaign produced with CMSSW 80X. The two signal sam-
 1428 ples (for tHq and tHW) were produced with MG5_aMC@NLO (version 5.222), in
 1429 leading-order mode, and are normalized to next-to-leading-order cross sections,
 1430 see Tab. 4.1. Each sample is generated with a set of event weights corresponding to
 1431 different values of κ_t and κ_V couplings as shown in Tab. 4.2.

1432 4.2.1 Full 2016 dataset and MC samples

Sample	σ [pb]	BF
/THQ_Hincl_13TeV-madgraph-pythia8_TuneCUETP8M1/	0.7927	0.324
/THW_Hincl_13TeV-madgraph-pythia8_TuneCUETP8M1/	0.1472	1.0

Table 4.1: Signal samples and their cross section and branching fraction used in this analysis. See Ref. [88] for more details.

1433 Different MC generators were used to generate the background processes. The
 1434 dominant sources ($t\bar{t}$, $t\bar{t}W$, $t\bar{t}Z$, $t\bar{t}H$) were produced using AMC@NLO interfaced
 1435 to PYTHIA8, and are scaled to NLO cross sections. Other processes are simulated

		<i>tHq</i>		<i>tHW</i>		
κ_V	κ_t	sum of weights	cross section [pb]	sum of weights	cross section [pb]	LHE weights
1.0	-3.0	35.700022	2.991	11.030445	0.6409	LHEweight_wgt[446]
1.0	-2.0	20.124298	1.706	5.967205	0.3458	LHEweight_wgt[447]
1.0	-1.5	14.043198	1.205	4.029093	0.2353	LHEweight_wgt[448]
1.0	-1.25	11.429338	0.9869	3.208415	0.1876	LHEweight_wgt[449]
1.0	-1.0		0.7927		0.1472	
1.0	-0.75	7.054998	0.6212	1.863811	0.1102	LHEweight_wgt[450]
1.0	-0.5	5.294518	0.4723	1.339886	0.07979	LHEweight_wgt[451]
1.0	-0.25	3.818499	0.3505	0.914880	0.05518	LHEweight_wgt[452]
1.0	0.0	2.627360	0.2482	0.588902	0.03881	LHEweight_wgt[453]
1.0	0.25	1.719841	0.1694	0.361621	0.02226	LHEweight_wgt[454]
1.0	0.5	1.097202	0.1133	0.233368	0.01444	LHEweight_wgt[455]
1.0	0.75	0.759024	0.08059	0.204034	0.01222	LHEweight_wgt[456]
1.0	1.0	0.705305	0.07096	0.273617	0.01561	LHEweight_wgt[457]
1.0	1.25	0.936047	0.0839	0.442119	0.02481	LHEweight_wgt[458]
1.0	1.5	1.451249	0.1199	0.709538	0.03935	LHEweight_wgt[459]
1.0	2.0	3.335034	0.2602	1.541132	0.08605	LHEweight_wgt[460]
1.0	3.0	10.516125	0.8210	4.391335	0.2465	LHEweight_wgt[461]
1.5	-3.0	45.281492	3.845	13.426212	0.7825	LHEweight_wgt[462]
1.5	-2.0	27.606715	2.371	7.809713	0.4574	LHEweight_wgt[463]
1.5	-1.5	20.476088	1.784	5.594971	0.3290	LHEweight_wgt[464]
1.5	-1.25	17.337465	1.518	4.635978	0.2749	LHEweight_wgt[465]
1.5	-1.0	14.483302	1.287	3.775902	0.2244	LHEweight_wgt[466]
1.5	-0.75	11.913599	1.067	3.014744	0.1799	LHEweight_wgt[467]
1.5	-0.5	9.628357	0.874	2.352505	0.1410	LHEweight_wgt[468]
1.5	-0.25	7.627574	0.702	1.789184	0.1081	LHEweight_wgt[469]
1.5	0.0	5.911882	0.5577	1.324946	0.08056	LHEweight_wgt[470]
1.5	0.25	4.479390	0.4365	0.959295	0.05893	LHEweight_wgt[471]
1.5	0.5	3.331988	0.3343	0.692727	0.04277	LHEweight_wgt[472]
1.5	0.75	2.469046	0.2558	0.525078	0.03263	LHEweight_wgt[473]
1.5	1.0	1.890565	0.2003	0.456347	0.02768	LHEweight_wgt[474]
1.5	1.25	1.596544	0.1689	0.486534	0.02864	LHEweight_wgt[475]
1.5	1.5	1.586983	0.1594	0.615638	0.03509	LHEweight_wgt[476]
1.5	2.0	2.421241	0.2105	1.170602	0.06515	LHEweight_wgt[477]
1.5	3.0	7.503280	0.5889	3.467546	0.1930	LHEweight_wgt[478]
0.5	-3.0	27.432685	2.260	8.929074	0.5136	LHEweight_wgt[479]
0.5	-2.0	13.956013	1.160	4.419093	0.2547	LHEweight_wgt[480]
0.5	-1.5	8.924438	0.7478	2.757611	0.1591	LHEweight_wgt[481]
0.5	-1.25	6.835341	0.5726	2.075247	0.1204	LHEweight_wgt[482]
0.5	-1.0	5.030704	0.4273	1.491801	0.08696	LHEweight_wgt[483]
0.5	-0.75	3.510528	0.2999	1.007273	0.05885	LHEweight_wgt[484]
0.5	-0.5	2.274811	0.1982	0.621663	0.03658	LHEweight_wgt[485]
0.5	-0.25	1.323555	0.1189	0.334972	0.01996	LHEweight_wgt[486]
0.5	0.0	0.656969	0.06223	0.147253	0.008986	LHEweight_wgt[487]
0.5	0.25	0.274423	0.02830	0.058342	0.003608	LHEweight_wgt[488]
0.5	0.5	0.176548	0.01778	0.068404	0.003902	LHEweight_wgt[489]
0.5	0.75	0.363132	0.03008	0.177385	0.009854	LHEweight_wgt[490]
0.5	1.0	0.834177	0.06550	0.385283	0.02145	LHEweight_wgt[491]
0.5	1.25	1.589682	0.1241	0.692099	0.03848	LHEweight_wgt[492]
0.5	1.5	2.629647	0.2047	1.097834	0.06136	LHEweight_wgt[493]
0.5	2.0	5.562958	0.4358	2.206057	0.1246	LHEweight_wgt[494]
0.5	3.0	14.843102	1.177	5.609519	0.3172	LHEweight_wgt[495]

Table 4.2: κ_V and κ_t combinations generated for the two signal samples and their NLO cross sections. The *tHq* cross section is multiplied by the branching fraction of the enforced leptonic decay of the top quark (0.324). See also Ref. [88].

Sample	σ [pb]
TTWJetsToLNu_TuneCUETP8M1_13TeV-amcatnloFXFX-madspin-pythia8	0.2043
TTZToLLNuNu_M-10_TuneCUETP8M1_13TeV-amcatnlo-pythia8	0.2529
tthJetToNonbb_M125_13TeV_amcatnloFXFX_madspin_pythia8_mWCutfix /store/cmst3/group/susy/gpetrucc/13TeV/u/TTLL_m1to10_L0_NoMS_for76X/	0.2151 0.0283
WGToLNuG_TuneCUETP8M1_13TeV-madgraphMLM-pythia8	585.8
ZGTo2LG_TuneCUETP8M1_13TeV-amcatnloFXFX-pythia8	131.3
TGJets_TuneCUETP8M1_13TeV_amcatnlo_madspin_pythia8	2.967
TGJets_TuneCUETP8M1_13TeV_amcatnlo_madspin_pythia8	2.967
TTGJets_TuneCUETP8M1_13TeV-amcatnloFXFX-madspin-pythia8	3.697
WpWpJJ_EWK_QCD_TuneCUETP8M1_13TeV-madgraph-pythia8	0.03711
ZZZ_TuneCUETP8M1_13TeV-amcatnlo-pythia8	0.01398
WWZ_TuneCUETP8M1_13TeV-amcatnlo-pythia8	0.1651
WZZ_TuneCUETP8M1_13TeV-amcatnlo-pythia8	0.05565
WW_DoubleScattering_13TeV-pythia8	1.64
tZq_ll_4f_13TeV-amcatnlo-pythia8_TuneCUETP8M1	0.0758
ST_tWll_5f_LO_13TeV-MadGraph-pythia8	0.01123
TTTT_TuneCUETP8M1_13TeV-amcatnlo-pythia8	0.009103
WZTo3LNu_TuneCUETP8M1_13TeV-powheg-pythia8	4.4296
ZZTo4L_13TeV_powheg_pythia8	1.256
TTJets_SingleLeptFromTbar_TuneCUETP8M1_13TeV-madgraphMLM-pythia8	182.1754
TTJets_SingleLeptFromT_TuneCUETP8M1_13TeV-madgraphMLM-pythia8	182.1754
TTJets_DiLept_TuneCUETP8M1_13TeV-madgraphMLM-pythia8	87.3
DYJetsToLL_M-10to50_TuneCUETP8M1_13TeV-amcatnloFXFX-pythia8	18610
DYJetsToLL_M-50_TuneCUETP8M1_13TeV-madgraphMLM-pythia8	6024
WJetsToLNu_TuneCUETP8M1_13TeV-amcatnloFXFX-pythia8	61526.7
ST_tW_top_5f_inclusiveDecays_13TeV-powheg-pythia8_TuneCUETP8M1	35.6
ST_tW_antitop_5f_inclusiveDecays_13TeV-powheg-pythia8_TuneCUETP8M1	35.6
ST_t-channel_4f_leptonDecays_13TeV-amcatnlo-pythia8_TuneCUETP8M1	70.3144
ST_t-channel_antitop_4f_leptonDecays_13TeV-powheg-pythia8_TuneCUETP8M1	26.2278
ST_s-channel_4f_leptonDecays_13TeV-amcatnlo-pythia8_TuneCUETP8M1	3.68064
WWTo2L2Nu_13TeV-powheg	10.481

Table 4.3: List of background samples used in this analysis (CMSSW 80X). In the first section of the table are listed the samples of the processes for which we use the simulation to extract the final yields and shapes, in the second section the samples of the processes we will estimate from data. The MC simulation is used to design the data driven methods and derive the associated systematics.

Sample	σ [pb]
ttWJets_13TeV_madgraphMLM	0.6105
ttZJets_13TeV_madgraphMLM	0.5297/0.692

Table 4.4: Leading-order $t\bar{t}W$ and $t\bar{t}Z$ samples used in the signal BDT training.

1436 using POWHEG interfaced to PYTHIA, or bare PYTHIA (see table 4.3 and [86]
1437 for more details).

Three lepton and Four lepton
HLT_DiMu9_Ele9_CaloIdL_TrackIdL_v*
HLT_Mu8_DiEle12_CaloIdL_TrackIdL_v*
HLT_TripleMu_12_10_5_v*
HLT_Ele16_Ele12_Ele8_CaloIdL_TrackIdL_v*
HLT_Mu23_TrkIsoVVL_Ele8_CaloIdL_TrackIdL_IsoVL_v*
HLT_Mu23_TrkIsoVVL_Ele8_CaloIdL_TrackIdL_IsoVL_DZ_v*
HLT_Mu8_TrkIsoVVL_Ele23_CaloIdL_TrackIdL_IsoVL_v*
HLT_Mu8_TrkIsoVVL_Ele23_CaloIdL_TrackIdL_IsoVL_DZ_v*
HLT_Ele23_Ele12_CaloIdL_TrackIdL_IsoVL_DZ_v*
HLT_Mu17_TrkIsoVVL_Mu8_TrkIsoVVL_DZ_v*
HLT_Mu17_TrkIsoVVL_TkMu8_TrkIsoVVL_DZ_v*
HLT_IsoMu22_v*
HLT_IsoTkMu22_v*
HLT_IsoMu22_eta2p1_v*
HLT_IsoTkMu22_eta2p1_v*
HLT_IsoMu24_v*
HLT_IsoTkMu24_v*
HLT_Ele27_WPTight_Gsf_v*
HLT_Ele25_eta2p1_WPTight_Gsf_v*
HLT_Ele27_eta2p1_WPLoose_Gsf_v*

Table 4.5: Table of high-level triggers that we consider in the analysis.

1438 4.2.2 Triggers

1439 We consider online-reconstructed events triggered by one, two, or three leptons.
 1440 Single-lepton triggers are included to boost the acceptance of events where the p_T of
 1441 the sub-leading lepton falls below the threshold of the double-lepton triggers. Ad-
 1442 ditionally, by including double-lepton triggers in the ≥ 3 lepton category, as well
 1443 as single-lepton triggers in all categories, we increase the efficiency, considering the
 1444 logical “or” of the trigger decisions of all the individual triggers in a given category.
 1445 Tab. 4.5 shows the lowest-threshold non-prescaled triggers present in the High-Level
 1446 Trigger (HLT) menus for both Monte-Carlo and data in 2016.

1447 4.2.2.1 Trigger efficiency scale factors

1448 The efficiency of events to pass the trigger is measured in simulation (trivially using
 1449 generator information) and in the data (using event collected by an uncorrelated

Category	Scale Factor
ee	1.01 ± 0.02
e μ	1.01 ± 0.01
$\mu\mu$	1.00 ± 0.01
3l	1.00 ± 0.03

Table 4.6: Trigger efficiency scale factors and associated uncertainties, shown here rounded to the nearest percent.

1450 MET trigger). Small differences between the data and MC efficiencies are corrected
 1451 by applying scale factors as shown in Tab. 4.6. The exact procedure and control plots
 1452 are documented in [89] for the current analysis.

1453 4.3 Object Identification and event selection

1454 4.3.1 Jets and b tagging

1455 The analysis uses anti- k_t (0.4) particle-flow (PF) jets, corrected for charged hadrons
 1456 not coming from the primary vertex (charged hadron subtraction), and having jet
 1457 energy corrections (`Summer16_23Sep2016V3`) applied as a function of the jet E_T and
 1458 η . Jets are only considered if they have a transverse energy above 25GeV.

1459 In addition, they are required to be separated from any lepton candidates passing
 1460 the fakeable object selections (see Tables 4.7 and 4.8) by $\Delta R > 0.4$.

1461 The loose and medium working points of the CSV b-tagging algorithm are used to
 1462 identify b jets. Data/simulation differences in the b tagging performance are corrected
 1463 by applying per-jet weights to the simulation, dependent on the jet p_T , eta, b tagging
 1464 discriminator, and flavor (from simulation truth) [90]. The per-event weight is taken
 1465 as the product of the per-jet weights, including those of the jets associated to the
 1466 leptons. More details can be found in the corresponding $t\bar{t}H$ documentation [86, 89].

¹⁴⁶⁷ **4.3.2 Lepton selection**

Cut	Loose	Fakeable object	Tight
$ \eta < 2.4$	✓	✓	✓
p_T	$> 5\text{GeV}$	$> 15\text{GeV}$	$> 15\text{GeV}$
$ d_{xy} < 0.05 \text{ (cm)}$	✓	✓	✓
$ d_z < 0.1 \text{ (cm)}$	✓	✓	✓
$\text{SIP}_{3D} < 8$	✓	✓	✓
$I_{\text{mini}} < 0.4$	✓	✓	✓
is Loose Muon	✓	✓	✓
jet CSV	—	< 0.8484	< 0.8484
is Medium Muon	—	—	✓
tight-charge	—	—	✓
lepMVA > 0.90	—	—	✓

Table 4.7: Requirements on each of the three muon selections. In the cases where the cut values change between the selections, those values are listed in the table. Otherwise, whether the cut is applied is indicated. For the two p_T^{ratio} and CSV rows, the cuts marked with a † are applied to leptons that fail the lepton MVA cut, while the loose cut value is applied to those that pass the lepton MVA cut.

¹⁴⁶⁸ The lepton reconstruction and selection is identical to that used in the $t\bar{t}H$ mul-
¹⁴⁶⁹ tilepton analysis, as documented in Refs. [86, 89]. For details on the reconstruction
¹⁴⁷⁰ algorithms, isolation, pileup mitigation, and a description of the lepton MVA discrim-
¹⁴⁷¹ inator and validation plots thereof, we refer to that document since they are out of
¹⁴⁷² the scope of this thesis. Three different selections are defined both for the electron
¹⁴⁷³ and muon object identification: the *Loose*, *Fakeable Object*, and *Tight* selection. As
¹⁴⁷⁴ described in more detail later, these are used for event level vetoes, the fake rate
¹⁴⁷⁵ estimation application region, and the final signal selection, respectively. The p_T of
¹⁴⁷⁶ fakeable objects is defined as $0.85 \times p_T(\text{jet})$, where the jet is the one associated to the
¹⁴⁷⁷ lepton object. This mitigates the dependence of the fake rate on the momentum of
¹⁴⁷⁸ the fakeable object and thereby improves the precision of the method.

¹⁴⁷⁹ Tables 4.7 and 4.8 list the full criteria for the different selections of muons and
¹⁴⁸⁰ electrons.

Cut	Loose	Fakeable Object	Tight
$ \eta < 2.5$	✓	✓	✓
p_T	$> 7\text{GeV}$	$> 15\text{GeV}$	$> 15\text{GeV}$
$ d_{xy} < 0.05 \text{ (cm)}$	✓	✓	✓
$ d_z < 0.1 \text{ (cm)}$	✓	✓	✓
$\text{SIP}_{3D} < 8$	✓	✓	✓
$I_{\text{mini}} < 0.4$	✓	✓	✓
MVA ID $> (0.0, 0.0, 0.7)$	✓	✓	✓
$\sigma_{in\eta} < (0.011, 0.011, 0.030)$	—	✓	✓
$\text{H/E} < (0.10, 0.10, 0.07)$	—	✓	✓
$\Delta\eta_{in} < (0.01, 0.01, 0.008)$	—	✓	✓
$\Delta\phi_{in} < (0.04, 0.04, 0.07)$	—	✓	✓
$-0.05 < 1/E - 1/p < (0.010, 0.010, 0.005)$	—	✓	✓
p_T^{ratio}	—	$> 0.5^\dagger / -$	—
jet CSV	—	$< 0.3^\dagger / < 0.8484$	< 0.8484
tight-charge conversion rejection	—	—	✓
Number of missing hits	< 2	$== 0$	$== 0$
lepMVA > 0.90	—	—	✓

Table 4.8: Criteria for each of the three electron selections. In cases where the cut values change between selections, those values are listed in the table. Otherwise, whether the cut is applied is indicated. In some cases, the cut values change for different η ranges. These ranges are $0 < |\eta| < 0.8$, $0.8 < |\eta| < 1.479$, and $1.479 < |\eta| < 2.5$ and the respective cut values are given in the form (value₁, value₂, value₃).

4.3.3 Lepton selection efficiency

Efficiencies of reconstruction and selecting loose leptons are measured both for muons and electrons using a tag and probe method on both data and MC, using $Z \rightarrow \ell^+ \ell^-$. Corresponding scale factors are derived from the ratio of efficiencies and applied to the selected These. Events are produced for the leptonic SUSY analyses using equivalent lepton selections and recycled for the $t\bar{t}H$ analysis as well as for this analysis. The efficiencies of applying the tight selection as defined in Tables 4.7 and 4.8, on the loose leptons are determined again by using a tag and probe method on a sample of DY-enriched events. They are documented for the $t\bar{t}H$ analysis in Ref. [89] and are exactly equivalent for this analysis.

1491 4.4 Background predictions

1492 The modeling of reducible and irreducible backgrounds in this analysis uses the exact
 1493 methods, analysis code, and ROOT trees used for the $t\bar{t}H$ multilepton analysis. We
 1494 give a brief description of the methods and refer to the documentation of that analysis
 1495 in Refs. [86, 89] for any details.

1496 The backgrounds in three-lepton final states can be split in two broad categories:
 1497 irreducible backgrounds with genuine prompt leptons (i.e. from on-shell W and Z
 1498 boson decays); and reducible backgrounds where at least one of the leptons is “non-
 1499 prompt”, i.e. produced within a hadronic jet, either a genuine lepton from heavy
 1500 flavor decays, or simply mis-reconstructed jets.

1501 Irreducible backgrounds can be reliably estimated directly from Monte-Carlo sim-
 1502 ulated events, using higher-order cross sections or data control regions for the overall
 1503 normalization. This is done in this analysis for all backgrounds involving prompt lep-
 1504 tons: $t\bar{t}W$, $t\bar{t}Z$, $t\bar{t}H$, WZ , ZZ , $W^\pm W^\pm qq$, $t\bar{t}t\bar{t}$, tZq , tZW , WWW , WWZ , WZZ ,
 1505 ZZZ .

1506 Reducible backgrounds, on the other hand, are not well predicted by simulation,
 1507 and are estimated using data-driven methods. In the case of non-prompt leptons, a
 1508 fake rate method is used, where the contribution to the final selection is estimated by
 1509 extrapolating from a sideband (or “application region”) with a looser lepton definition
 1510 (the fakeable object definitions in Tabs. 4.7 and 4.8) to the signal selection. The tight-
 1511 to-loose ratios (or “fake rates”) are measured in several background dominated data
 1512 events with dedicated triggers, subtracting the residual prompt lepton contribution
 1513 using MC. Non-prompt leptons in our signal regions are predominantly produced in $t\bar{t}$
 1514 events, with a much smaller contribution, from Drell–Yan production. The systematic
 1515 uncertainty on the normalization of the non-prompt background estimation is on the

order of 50%, and thereby one of the dominant limitations on the performance of multilepton analyses in general and this analysis in particular. It consists of several individual sources, such as the result of closure tests of the method using simulated events, limited statistics in the data control regions due to necessary prescaling of lepton triggers, and the uncertainty in the subtraction of residual prompt leptons from the control region.

The fake background where the leptons pass the looser selection are weighted according to how many of them fail the tight criteria. Events with a single failing lepton are weighted with the factor $f/(1-f)$ for the estimate to the tight selection region, where f is the fake rate. Events with two failing leptons are given the negative weight $-f_i f_j / (1-f_i)(1-f_j)$, and for three leptons the weight is positive and equal to the product of $f/(1-f)$ factor evaluated for each failing lepton.

Figures 4.2 show the distributions of some relevant kinematic variables, normalized to the cross section of the respective processes and to the integrated luminosity.

4.5 Signal discrimination

The tHq signal is separated from the main backgrounds using a boosted decision tree (BDT) classifier, trained on simulated signal and background events. A set of discriminating variables are given as input to the BDT which produces a output distribution maximizing the discrimination power. Table 4.9 lists the input variables used while Figures 4.3 show their distributions for the relevant signal and background samples, for the three lepton channel. Two BDT classifiers are trained for the two main backgrounds expected in the analysis: events with prompt leptons from $t\bar{t}W$ and $t\bar{t}Z$ (also referred to as $t\bar{t}V$), and events with non-prompt leptons from $t\bar{t}$. The datasets used in the training are the tHq signal (see Tab. 4.1), and LO MADGRAPH samples

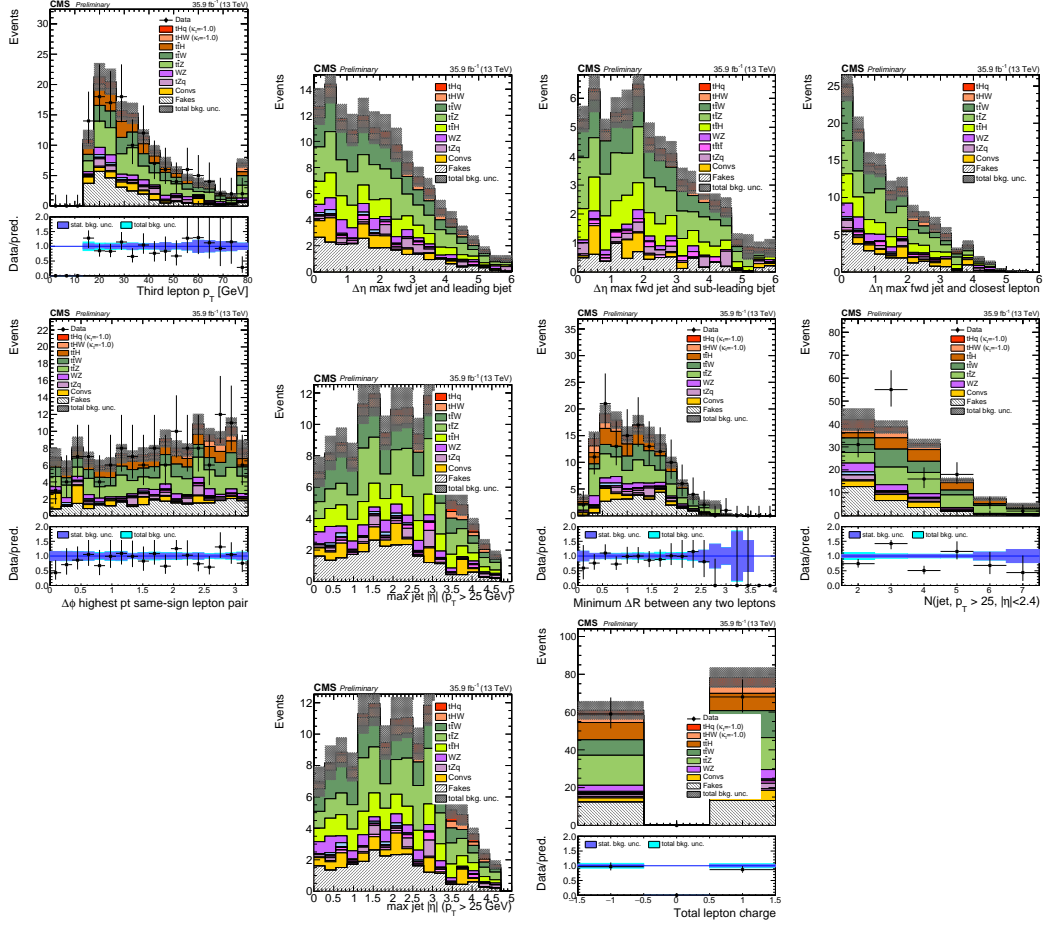


Figure 4.2: Distributions of input variables to the BDT for signal discrimination, three lepton channel, normalized to their cross section and to 35.9 fb^{-1} .

of $t\bar{t}W$ and $t\bar{t}Z$, in an admixture proportional to their respective cross sections (see Tab. 4.4).

The MVA analysis consist of two stages: first a “training” where the MVA method is trained to discriminate between simulated signal and background events, then a “test” stage where the trained algorithm is used to classify different events from the samples. The sample is obtained from a pre-selection (see Tab. ?? with pre-selection cuts). Figures 4.4 show the input variables distributions as seen by the MVA algorithm. Note that in contrast to the distributions in Fig. 4.3 only the main backgrounds ($t\bar{t}$ from simulation, $t\bar{t}V$) are included.

Variable name	Description
nJet25	Number of jets with $p_T > 25$ GeV, $ \eta < 2.4$
MaxEtaJet25	Maximum $ \eta $ of any (non-CSV-loose) jet with $p_T > 25$ GeV
totCharge	Sum of lepton charges
nJetEta1	Number of jets with $ \eta > 1.0$, non-CSV-loose
detaFwdJetBJet	$\Delta\eta$ between forward light jet and hardest CSV loose jet
detaFwdJet2BJet	$\Delta\eta$ between forward light jet and second hardest CSV loose jet (defaults to -1 in events with only one CSV loose jet)
detaFwdJetClosestLep	$\Delta\eta$ between forward light jet and closest lepton
dphiHighestPtSSPair	$\Delta\phi$ of highest p_T same-sign lepton pair
minDRll	minimum ΔR between any two leptons
Lep3Pt/Lep2Pt	p_T of the 3 rd lepton (2 nd for ss2l)

Table 4.9: MVA input discriminating variables

1549 Note that splitting the training in two groups reveals that some variables show
 1550 opposite behavior for the two background sources; potentially screening the discrimi-
 1551 nation power if they were to be used in a single discriminant. For some other variables
 1552 the distributions are similar in both background cases.

1553 From table 4.9, it is clear that the input variables are correlated to some extend.
 1554 These correlations play an important role for some MVA methods like the Fisher
 1555 discriminant method in which the first step consist of performing a linear transfor-
 1556 mation to an phase space where the correlations between variables are removed. In
 1557 case a boosted decision tree (BDT) method however, correlations do not affect the
 1558 performance. Figure 4.6 show the linear correlation coefficients for signal and back-
 1559 ground for the two training cases (the signal values are identical by construction). As
 1560 expected, strong correlations appears for variables related to the forward jet activity.
 1561 Same trend is seen in case of the same sign dilepton channel in Figure ??.

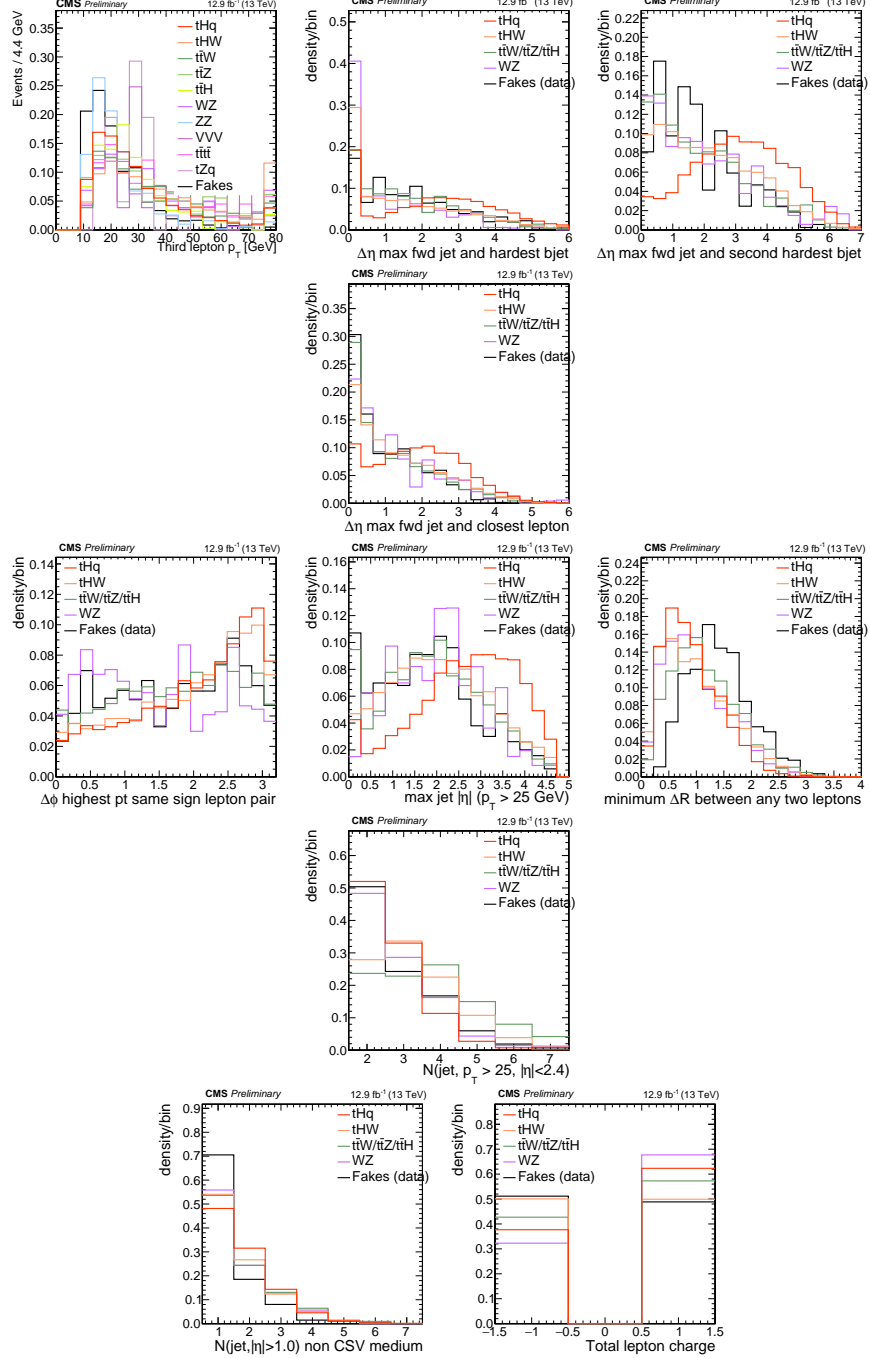


Figure 4.3: Distributions of input variables to the BDT for signal discrimination, three lepton channel.

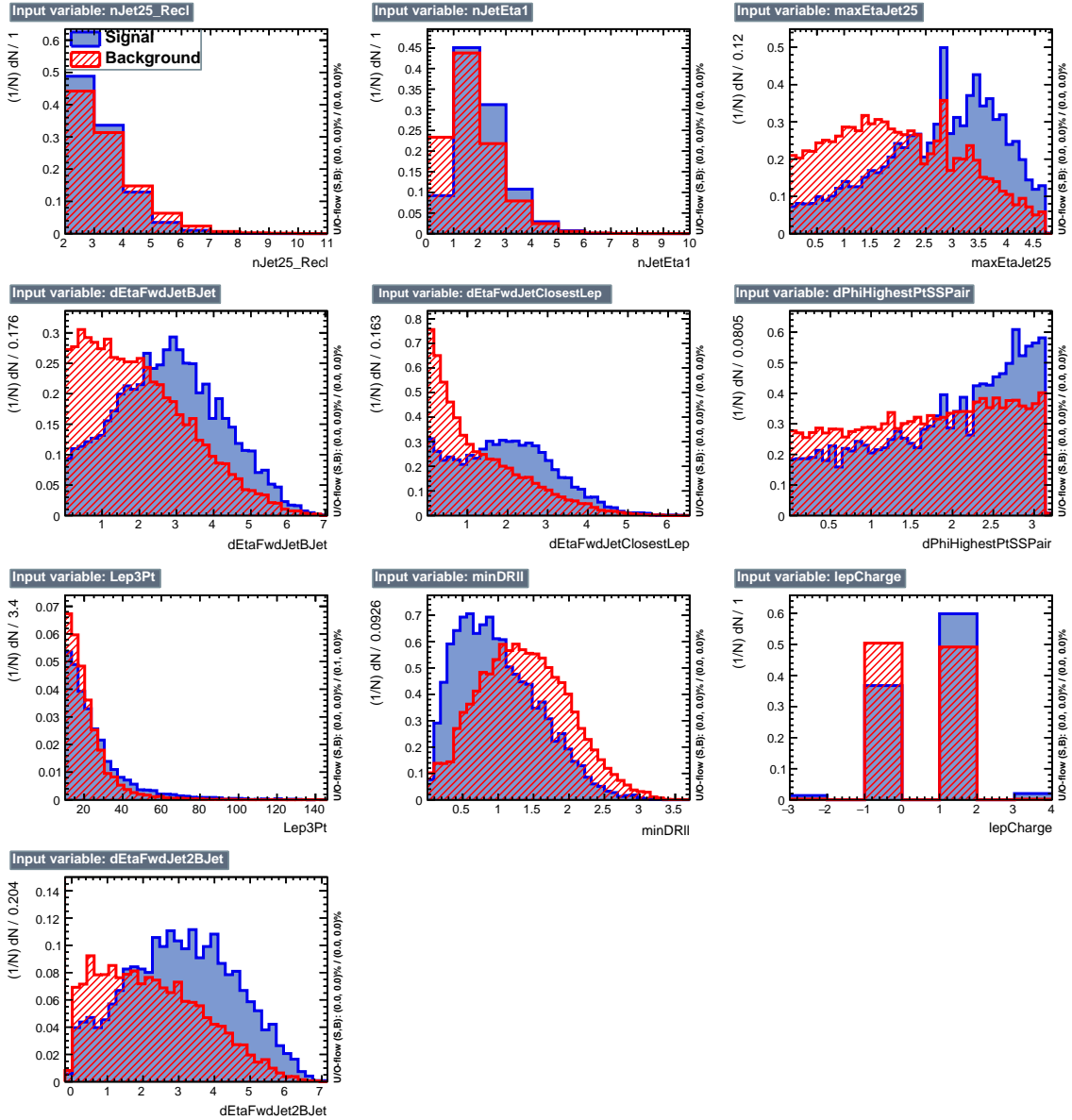


Figure 4.4: BDT inputs as seen by TMVA (signal, in blue, is tHq , background, in red, is $t\bar{t}$) for the three lepton channel, discriminated against $t\bar{t}$ (fakes) background.

1562 4.5.1 Classifiers response

1563 Several MVA algorithms were evaluated to determine the most appropriate method
 1564 for this analysis. The plots in Fig. 4.7 (top) show the background rejection as a
 1565 function of the signal efficiency for $t\bar{t}$ and $t\bar{t}V$ trainings (ROC curves) for the different

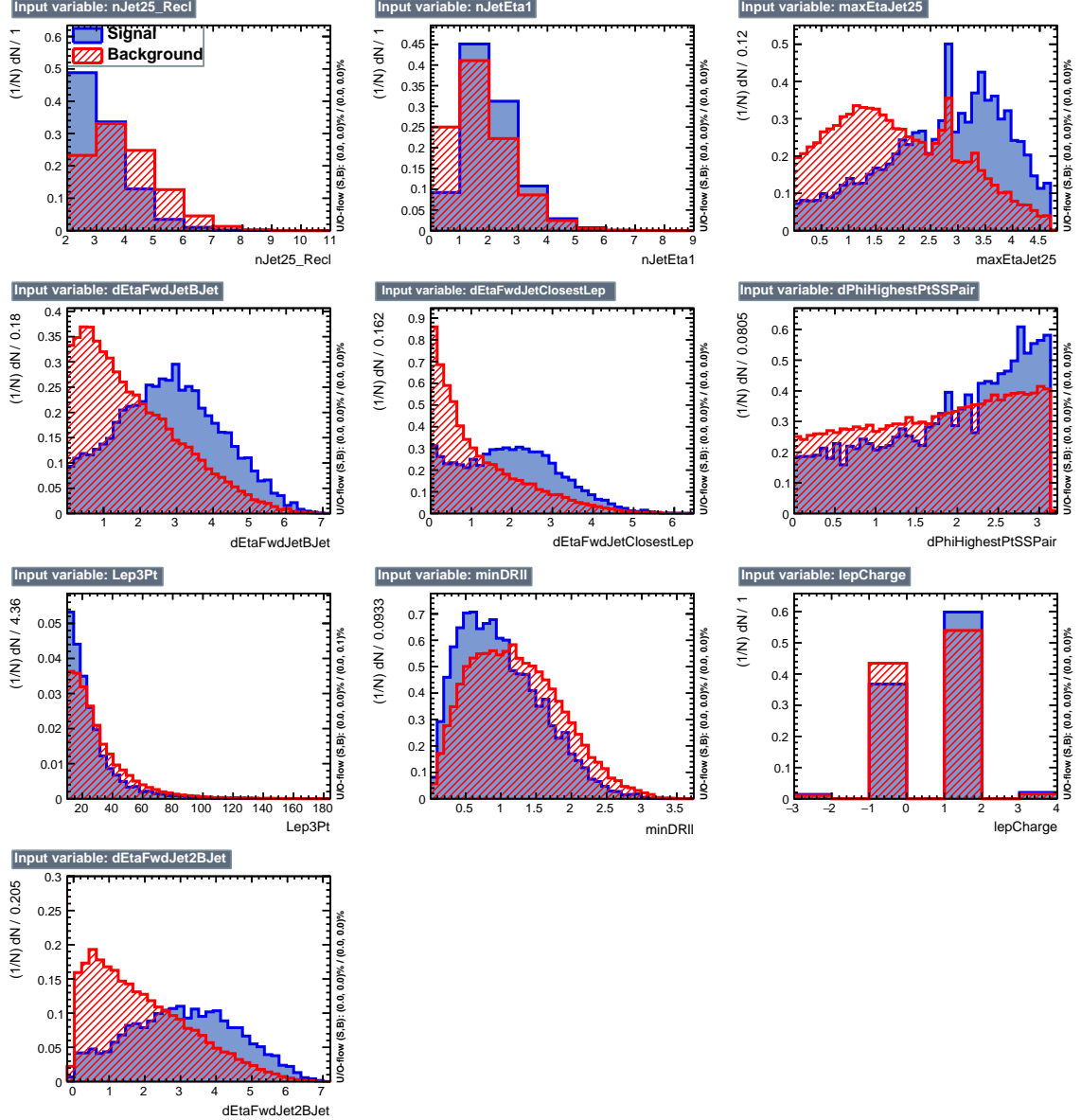


Figure 4.5: BDT inputs as seen by TMVA (signal, in blue, is tHq , background, in red, is $t\bar{t}W+t\bar{t}Z$) for the three lepton channel, discriminated against $t\bar{t}V$ background.

algorithms that were evaluated.

In both cases the gradient boosted decision tree (“BDTA_GRAD”) classifier offers the best results, followed by an adaptive BDT classifier (“BDTA”). The BDTA_GRAD classifier output distributions for signal and backgrounds are shown on the bottom of Fig. 4.7. As expected, a good discrimination power is obtained using default discrim-

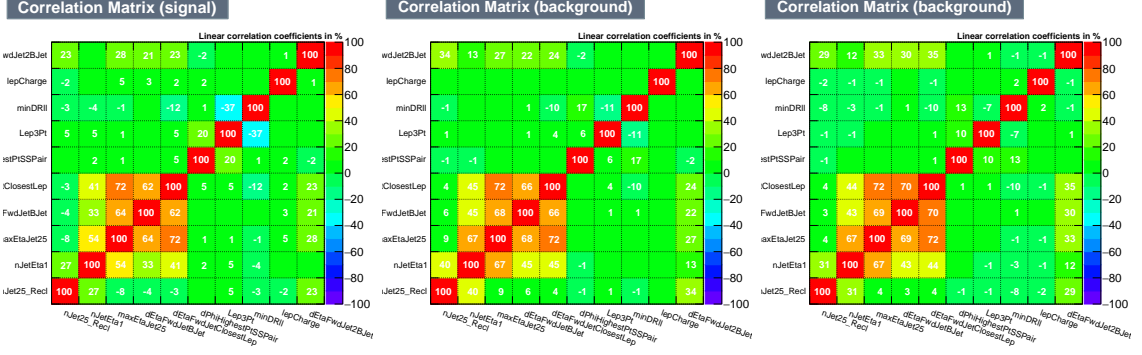


Figure 4.6: Signal (left), $t\bar{t}$ background (middle), and $t\bar{t}V$ background (right.) correlation matrices for the input variables in the TMVA analysis for the three lepton channel.

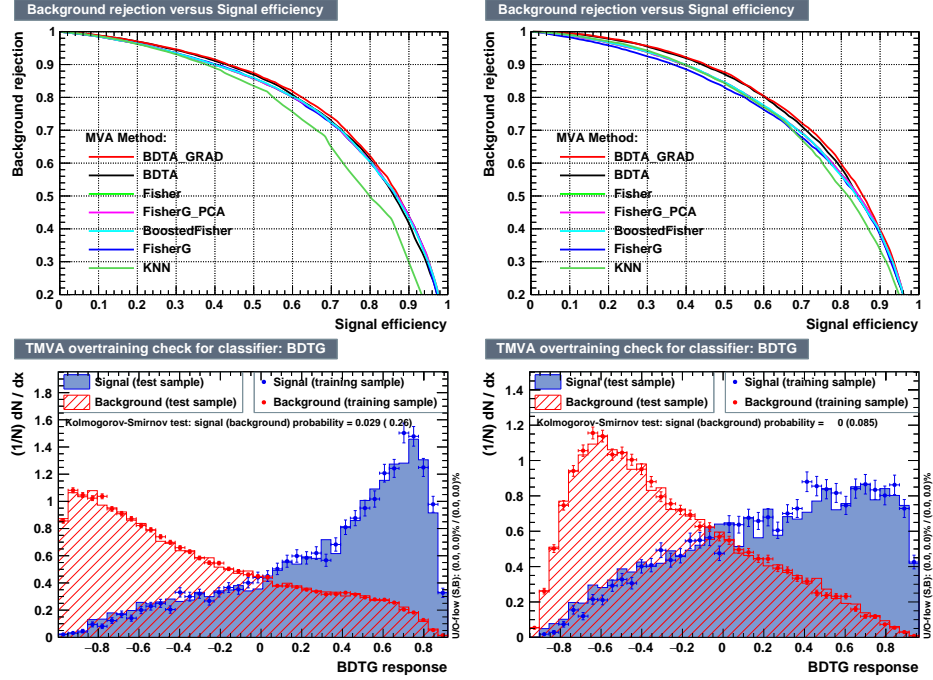


Figure 4.7: Top: background rejection vs signal efficiency (ROC curves) for various MVA classifiers (top) in the three lepton channel against $t\bar{t}V$ (left) and $t\bar{t}$ (right). Bottom: classifier output distributions for the gradient boosted decision trees, for training against $t\bar{t}V$ (left) and against $t\bar{t}$ (right).

1571 inator parameter values, with minimal overtraining. TMVA provides a ranking of the
 1572 input variables by their importance in the classification process, shown in Tab. 4.10.
 1573 The TMVA settings used in the BDT training are shown in Tab. 4.11.

ttbar training			ttV training		
Rank	Variable	Importance	Variable	Importance	Importance
1	minDRll	1.329e-01	dEtaFwdJetBJet	1.264e-01	
2	dEtaFwdJetClosestLep	1.294e-01	Lep3Pt	1.224e-01	
3	dEtaFwdJetBJet	1.209e-01	maxEtaJet25	1.221e-01	
4	dPhiHighestPtSSPair	1.192e-01	dEtaFwdJet2BJet	1.204e-01	
5	Lep3Pt	1.158e-01	dEtaFwdJetClosestLep	1.177e-01	
6	maxEtaJet25	1.121e-01	minDRll	1.143e-01	
7	dEtaFwdJet2BJet	9.363e-02	dPhiHighestPtSSPair	9.777e-02	
8	nJetEta1	6.730e-02	nJet25_Recl	9.034e-02	
9	nJet25_Recl	6.178e-02	nJetEta1	4.749e-02	
10	lepCharge	4.701e-02	lepCharge	4.116e-02	

Table 4.10: TMVA input variables ranking for BDTA_GRAD method for the trainings in the three lepton channel. For both trainings the rankings show almost the same 5 variables in the first places.

```

TMVA.Types.kBDT
NTrees=800
BoostType=Grad
Shrinkage=0.10
!UseBaggedGrad
nCuts=50
MaxDepth=3
NegWeightTreatment=PairNegWeightsGlobal
CreateMVAPdfs

```

Table 4.11: TMVA configuration used in the BDT training.

1574 4.6 Additional discriminating variables

1575 Two additional discriminating variables were tested considering the fact that the
 1576 forward jet in the background could come from the pileup; since we have a real
 1577 forward jet in the signal, it could give some improvement in the discriminating power.
 1578 The additional variables describe the forward jet momentum (fwdJetPt25) and the
 1579 forward jet identification(fwdJetPUID). Distributions for these variables in the three
 1580 lepton channel are shown in the figure 4.8. The forward jet identification distribution
 1581 show that for both, signal and background, jets are mostly real jets.

1582 The testing was made including in the MVA input one variable at a time, so we

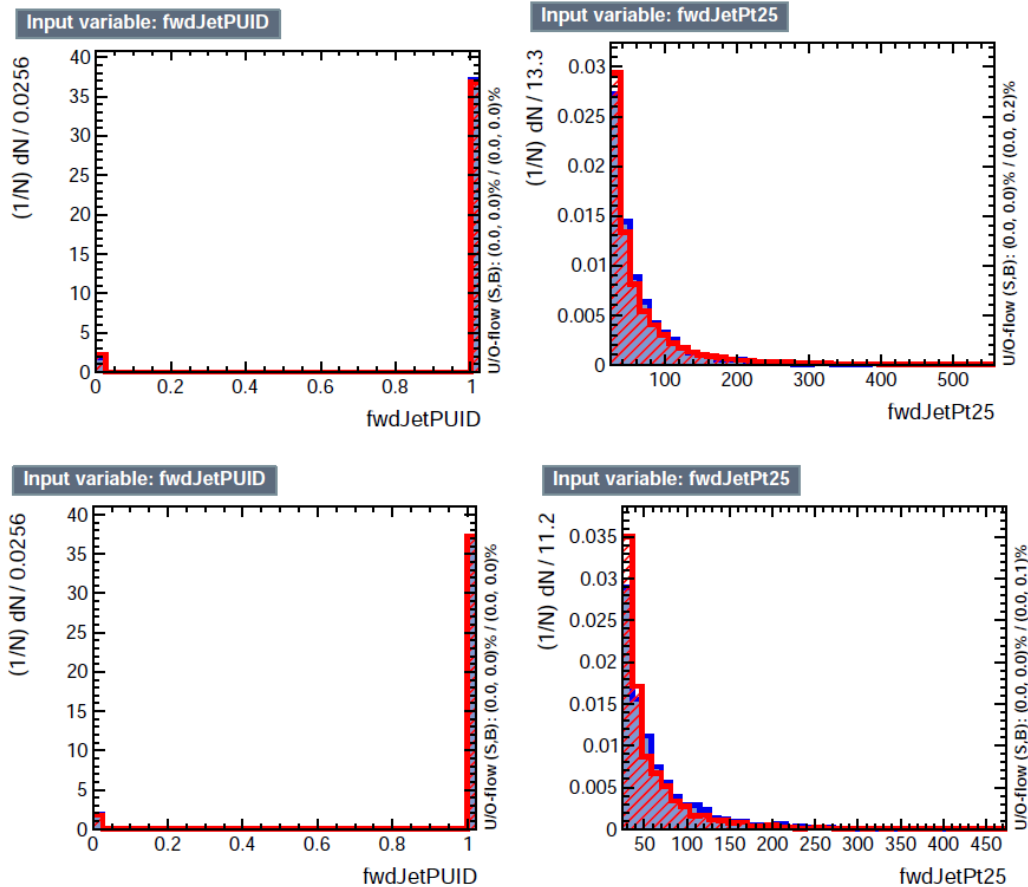


Figure 4.8: Additional discriminating variables distributions for ttV training (Top row) and tt training (bottom row) in the three lepton channel. The origin of the jets in the forward jet identification distribution is tagged as 0 for “pileup jets” while “real jets” are tagged as 1.

1583 can evaluate the discrimination power of each variable, and then both simultaneously.
 1584 fwdJetPUID was ranked in the last place in importance (11) in both training (ttV
 1585 and tt) while fwdJetPt25 was ranked 3 in the ttV training and 7 in the tt training.
 1586 When training using 12 variables, fwdJetPt25 was ranked 5 and 7 in the ttV and tt
 1587 trainings respectively, while fwdJetPUID was ranked 12 in both cases.

1588 The improvement in the discrimination performance provided by the additional
 1589 variables is about 1%, so it was decided not to include them in the procedure. Table
 1590 4.12 show the ROC-integral for all the testing cases we made.

ROC-integral	
base 10 var ttv	0.848
+ fwdJetPUID ttv	0.849
+ fwdJetPt25 ttv	0.856
12 var ttv	0.856
<hr/>	
base 10 var tt	0.777
+ fwdJetPUID tt	0.777
+ fwdJetPt25 tt	0.787
12 var	0.787

Table 4.12: ROC-integral for all the testing cases we made in the evaluation of the additional variables discriminating power. The improvement in the discrimination performance provided by the additional variables is about 1%

₁₅₉₁ **Chapter 5**

₁₅₉₂ **The CMS forward pixel detector**

₁₅₉₃ **5.0.1 The phase 1 FPix upgrade**

₁₅₉₄ **5.0.2 FPix module production line**

₁₅₉₅ **5.0.3 The Gluing stage**

₁₅₉₆ **5.0.4 The Encapsulation stage**

₁₅₉₇ **5.0.5 The FPix module production yields**

1598 **References**

- 1599 [1] D.J. Griffiths, “Introduction to electrodynamics”. 4th ed. Pearson, (2013).
- 1600 [2] F. Mandl, G. Shaw. “Quantum field theory.” Chichester: Wiley (2009).
- 1601 [3] F. Halzen, and A.D. Martin, “Quarks and leptons: An introductory course in
1602 modern particle physics”. New York: Wiley, (1984) .
- 1603 [4] J.C. Maxwell. “A dynamical theory of the electromagnetic field”. Philosophical
1604 Transactions of the Royal Society of London. 155: 459–512.(1865)
1605 doi:10.1098/rstl.1865.0008
- 1606 [5] M. Planck. “Über das Gesetz der Energieverteilung im Normalspektrum”.
1607 Annalen der Physik. 4 (3): 553.(1901).
- 1608 [6] A. Einstein “Über einen die Erzeugung und Verwandlung des Lichtes betref-
1609 fenden heuristischen Gesichtspunkt”. Annalen der Physik. 17 (6): 132–148,
1610 (1905).
- 1611 [7] A. Einstein. “Über die von der molekularkinetischen Theorie der Wärme
1612 geforderte Bewegung von in ruhenden Flüssigkeiten suspendierten Teilchen”.
1613 Annalen der Physik. 17 (8): 549–560, (1905).
- 1614 [8] A. Einstein. “Zur Elektrodynamik bewegter Körper”. Annalen der Physik. 17
1615 (10): 891–921, (1905).

- 1616 [9] A. Einstein, "Ist die TrÄdgheit eines KÃürpers von seinem Energieinhalt ab-
 1617 hÃdngig?". Annalen der Physik. 18 (13): 639â€¢641, (1905).
- 1618 [10] B. P. Abbott et al. "Observation of Gravitational Waves from a Binary Black
 1619 Hole Merger". PRL 116, 061102 (2016).
- 1620 [11] J. Schwinger. "Quantum Electrodynamics. I. A Covariant Formulation". Phys-
 1621 ical Review. 74 (10): 1439â€¢61, (1948).
- 1622 [12] R. P. Feynman. "Spaceâ€¢Time Approach to Quantum Electrodynamics".
 1623 Physical Review. 76 (6): 769â€¢89, (1949).
- 1624 [13] S. Tomonaga. "On a Relativistically Invariant Formulation of the Quantum
 1625 Theory of Wave Fields". Progress of Theoretical Physics. 1 (2): 27â€¢42, (1946).
- 1626 [14] S.L. Glashow. "Partial symmetries of weak interactions", Nucl. Phys. 22 579-
 1627 588, (1961).
- 1628 [15] A. Salam, J.C. Ward. "Electromagnetic and weak interactions", Physics Letters
 1629 13 168-171, (1964).
- 1630 [16] S. Weinberg, "A model of leptons", Physical Review Letters, vol. 19, no. 21, p.
 1631 1264, (1967).
- 1632 [17] E. Noether, "Invariante Variationsprobleme", Nachrichten von der Gesellschaft
 1633 der Wissenschaften zu GÃüttingen, mathematisch-physikalische Klasse, vol.
 1634 1918, pp. 235â€¢257, (1918).
- 1635 [18] File:Standard_Model_of_Elementary_Particle_dark.svg. (2017, June 12)
 1636 Wikimedia Commons, the free media repository. Retrieved November 27,
 1637 2017 from <https://www.collegiate-advanced-electricity.com/single-post/2017/04/10/The-Standard-Model-of-Particle-Physics>.

- 1639 [19] M. Goldhaber, L. Grodzins, A.W. Sunyar “Helicity of Neutrinos”, Phys. Rev.
 1640 109, 1015 (1958).
- 1641 [20] Palanque-Delabrouille N et al. “Neutrino masses and cosmology with Lyman-
 1642 alpha forest power spectrum”, JCAP 11 011 (2015).
- 1643 [21] C. Patrignani et al. (Particle Data Group), Chin. Phys. C, 40, 100001 (2016)
 1644 and 2017 update.
- 1645 [22] M. Gell-Mann. “A Schematic Model of Baryons and Mesons”. Physics Letters.
 1646 8 (3): 214–215 (1964).
- 1647 [23] G. Zweig. “An SU(3) Model for Strong Interaction Symmetry and its Breaking”
 1648 (PDF). CERN Report No.8182/TH.401 (1964).
- 1649 [24] G. Zweig. “An SU(3) Model for Strong Interaction Symmetry and its Breaking:
 1650 II” (PDF). CERN Report No.8419/TH.412(1964).
- 1651 [25] M. Gell-Mann. “The Interpretation of the New Particles as Displaced Charged
 1652 Multiplets”. Il Nuovo Cimento 4: 848. (1956).
- 1653 [26] T. Nakano, K. Nishijima. “Charge Independence for V-particles”. Progress of
 1654 Theoretical Physics 10 (5): 581-582. (1953).
- 1655 [27] N. Cabibbo, “Unitary symmetry and leptonic decays” Physical Review Letters,
 1656 vol. 10, no. 12, p. 531, (1963).
- 1657 [28] M.Kobayashi, T.Maskawa, “CP-violation in the renormalizable theory of weak
 1658 interaction,” Progress of Theoretical Physics, vol. 49, no. 2, pp. 652-657, (1973).
- 1659 [29] File:Weak Decay (flipped).svg. (2017, June 12). Wikimedia Com-
 1660 mons, the free media repository. Retrieved November 27, 2017

- 1661 from `https : //commons.wikimedia.org/w/index.php?title = File :`
 1662 `Weak_Decay_(flipped).svg&oldid = 247498592.`
- 1663 [30] Georgia Tech University. Coupling Constants for the Fundamental
 1664 Forces(2005). Retrieved January 10, 2018, from `http://hyperphysics.phy –`
 1665 `astr.gsu.edu/hbase/Forces/couple.html#c2`
- 1666 [31] M. Strassler. (May 31, 2013).The Strengths of the Known Forces. Retrieved
 1667 January 10, 2018, from `https://profmattstrassler.com/articles – and –`
 1668 `posts/particle – physics – basics/the – known – forces – of – nature/the –`
 1669 `strength – of – the – known – forces/`
- 1670 [32] M. Peskin, D. Schroeder, “An introduction to quantum field theory”. Perseus
 1671 Books Publishing L.L.C., (1995).
- 1672 [33] A. Pich. “The Standard Model of Electroweak Interactions”
 1673 `https://arxiv.org/abs/1201.0537`
- 1674 [34] F.Bellaiche. (2012, 2 September). “What’s this Higgs boson anyway?”. Retrieved
 1675 from: `https://www.quantum-bits.org/?p=233`
- 1676 [35] M. Endres et al. Nature 487, 454-458 (2012) doi:10.1038/nature11255
- 1677 [36] F. Englert, R. Brout. “Broken Symmetry and the Mass of Gauge
 1678 Vector Mesons”. Physical Review Letters. 13 (9): 321-23.(1964)
 1679 doi:10.1103/PhysRevLett.13.321
- 1680 [37] P.Higgs. “Broken Symmetries and the Masses of Gauge Bosons”. Physical Re-
 1681 view Letters. 13 (16): 508-509,(1964). doi:10.1103/PhysRevLett.13.508.

- 1682 [38] G.Guralnik, C.R. Hagen and T.W.B. Kibble. “Global Conservation Laws
 1683 and Massless Particles”. Physical Review Letters. 13 (20): 585-587, (1964).
 1684 doi:10.1103/PhysRevLett.13.585.
- 1685 [39] CMS collaboration. “Observation of a new boson at a mass of 125 GeV with
 1686 the CMS experiment at the LHC”. Physics Letters B. 716 (1): 30-61 (2012).
 1687 arXiv:1207.7235. doi:10.1016/j.physletb.2012.08.021
- 1688 [40] ATLAS collaboration. “Observation of a New Particle in the Search for the Stan-
 1689 dard Model Higgs Boson with the ATLAS Detector at the LHC”. Physics Letters
 1690 B. 716 (1): 1-29 (2012). arXiv:1207.7214. doi:10.1016/j.physletb.2012.08.020.
- 1691 [41] ATLAS collaboration; CMS collaboration (26 March 2015). “Combined Mea-
 1692 surement of the Higgs Boson Mass in pp Collisions at $\sqrt{s}=7$ and 8 TeV with
 1693 the ATLAS and CMS Experiments”. Physical Review Letters. 114 (19): 191803.
 1694 arXiv:1503.07589. doi:10.1103/PhysRevLett.114.191803.
- 1695 [42] CMS Collaboration, “SM Higgs Branching Ratios and To-
 1696 tal Decay Widths (up-date in CERN Report4 2016)”.
 1697 <https://twiki.cern.ch/twiki/bin/view/LHCPhysics/CERNYellowReportPageBR>, last accessed on 17.12.2017.
- 1699 [43] R.Grant V. “Determination of Higgs branching ratios in $H \rightarrow W^+W^- \rightarrow l^+l^- jj$ and $H \rightarrow ZZ \rightarrow l^+l^- jj$ channels”. Physics Department, Uni-
 1700 versity of Tennessee (Dated: October 31, 2012). Retrieved from
 1701 <http://aesop.phys.utk.edu/ph611/2012/projects/Riley.pdf>
- 1703 [44] LHC Higgs Cross Section Working Group, Denner, A., Heinemeyer, S. et al.
 1704 “Standard model Higgs-boson branching ratios with uncertainties”. Eur. Phys.
 1705 J. C (2011) 71: 1753. <https://doi.org/10.1140/epjc/s10052-011-1753-8>

- 1706 [45] LHC InternationalMasterclasses“When protons collide”. Retrieved from
 1707 http://atlas.physicsmasterclasses.org/en/zpath_protoncollisions.htm
- 1708 [46] F. Maltoni, K. Paul, T. Stelzer, and S. Willenbrock, “Associated production
 1709 of Higgs and single top at hadron colliders”, Phys.Rev. D64 (2001) 094023,
 1710 [hep-ph/0106293].
- 1711 [47] S. Biswas, E. Gabrielli, F. Margaroli, and B. Mele, “Direct constraints on the
 1712 top-Higgs coupling from the 8 TeV LHC data,” Journal of High Energy Physics,
 1713 vol. 07, p. 073, (2013).
- 1714 [48] M. Farina, C. Grojean, F. Maltoni, E. Salvioni, and A. Thamm, “Lifting de-
 1715 generacies in Higgs couplings using single top production in association with a
 1716 Higgs boson,” Journal of High Energy Physics, vol. 05, p. 022, (2013).
- 1717 [49] T.M. Tait and C.-P. Yuan, “Single top quark production as a window to physics
 1718 beyond the standard model”, Phys. Rev. D 63 (2000) 014018 [hep-ph/0007298].
- 1719 [50] F. Demartin, F. Maltoni, K. Mawatari, and M. Zaro, “Higgs production in
 1720 association with a single top quark at the LHC,” European Physical Journal C,
 1721 vol. 75, p. 267, (2015).
- 1722 [51] CMS Collaboration, “Modelling of the single top-quark pro-
 1723 duction in association with the Higgs boson at 13 TeV.”
 1724 <https://twiki.cern.ch/twiki/bin/viewauth/CMS/SingleTopHiggsGeneration13TeV>,
 1725 last accessed on 16.01.2018.
- 1726 [52] CMS Collaboration, “SM Higgs production cross sections at $\sqrt{s} = 13$ TeV.”
 1727 <https://twiki.cern.ch/twiki/bin/view/LHCPhysics/CERNYellowReportPageAt13TeV>, last
 1728 accessed on 16.01.2018.

- 1729 [53] S. Dawson, The effective W approximation, Nucl. Phys. B 249 (1985) 42.
- 1730 [54] S. Biswas, E. Gabrielli and B. Mele, JHEP 1301 (2013) 088 [arXiv:1211.0499
1731 [hep-ph]].
- 1732 [55] F. Demartin, B. Maier, F. Maltoni, K. Mawatari, and M. Zaro, “tWH associated
1733 production at the LHC”, European Physical Journal C, vol. 77, p. 34, (2017).
1734 arXiv:1607.05862
- 1735 [56] LHC Higgs Cross Section Working Group, “Handbook of LHC Higgs Cross
1736 Sections: 4.Deciphering the Nature of the Higgs Sector”, arXiv:1610.07922.
- 1737 [57] J. Ellis, D. S. Hwang, K. Sakurai, and M. Takeuchi.“Disentangling Higgs-Top
1738 Couplings in Associated Production”, JHEP 1404 (2014) 004, [arXiv:1312.5736].
- 1739 [58] CMS Collaboration, V. Khachatryan et al., “Precise determination of the mass
1740 of the Higgs boson and tests of compatibility of its couplings with the standard
1741 model predictions using proton collisions at 7 and 8 TeV,” arXiv:1412.8662.
- 1742 [59] ATLAS and CMS Collaborations, “Measurements of the Higgs boson produc-
1743 tion and decay rates and constraints on its couplings from a combined ATLAS
1744 and CMS analysis of the LHC pp collision data at $\sqrt{s} = 7$ and 8 TeV,” (2016).
1745 CERN-EP-2016-100, ATLAS-HIGG-2015-07, CMS-HIG-15-002.
- 1746 [60] File:Cern-accelerator-complex.svg. Wikimedia Commons,
1747 the free media repository. Retrieved January, 2018 from
1748 <https://commons.wikimedia.org/wiki/File:Cern-accelerator-complex.svg>
- 1749 [61] J.L. Caron , “Layout of the LEP tunnel including future LHC infrastructures.”,
1750 (Nov, 1993). A C Collection. Legacy of AC. Pictures from 1992 to 2002. Re-
1751 trieved from <https://cds.cern.ch/record/841542>

- 1752 [62] M. Vretenar, “The radio-frequency quadrupole”. CERN Yellow Report CERN-
 1753 2013-001, pp.207-223 DOI:10.5170/CERN-2013-001.207. arXiv:1303.6762
- 1754 [63] L.Evans. P. Bryant (editors). “LHC Machine”. JINST 3 S08001 (2008).
- 1755 [64] CERN Photographic Service.“Radio-frequency quadrupole, RFQ-1”, March
 1756 1983, CERN-AC-8303511. Retrieved from <https://cds.cern.ch/record/615852>.
- 1757 [65] CERN Photographic Service “Animation of CERN’s accelerator net-
 1758 work”, 14 October 2013. DOI: 10.17181/cds.1610170 Retrieved from
 1759 <https://videos.cern.ch/record/1610170>
- 1760 [66] C.Sutton. “Particle accelerator”.Encyclopedia Britannica. July 17, 2013. Re-
 1761 trieved from <https://www.britannica.com/technology/particle-accelerator>.
- 1762 [67] L.Guiraud. “Installation of LHC cavity in vacuum tank.”. July 27 2000. CERN-
 1763 AC-0007016. Retrieved from <https://cds.cern.ch/record/41567>.
- 1764 [68] J.L. Caron, “Magnetic field induced by the LHC dipole’s superconducting coils”.
 1765 March 1998. AC Collection. Legacy of AC. Pictures from 1992 to 2002. LHC-
 1766 PHO-1998-325. Retrieved from <https://cds.cern.ch/record/841511>
- 1767 [69] AC Team. “Diagram of an LHC dipole magnet”. June 1999. CERN-DI-9906025
 1768 retrieved from <https://cds.cern.ch/record/40524>.
- 1769 [70] CMS Collaboration “Public CMS Luminosity Information”.
 1770 https://twiki.cern.ch/twiki/bin/view/CMSPublic/LumiPublicResults#2016_proton_proton
 1771 last accessed 24.01.2018
- 1772 [71] J.L Caron. “LHC Layout” AC Collection. Legacy of AC. Pictures
 1773 from 1992 to 2002. September 1997, LHC-PHO-1997-060. Retrieved from
 1774 <https://cds.cern.ch/record/841573>.

- 1775 [72] CMS Collaboration. “The CMS experiment at the CERN LHC” JINST 3 S08004
1776 (2008).
- 1777 [73] CMS Collaboration. “CMS detector drawings 2012” CMS-PHO-GEN-2012-002.
1778 Retrieved from <http://cds.cern.ch/record/1433717>.
- 1779 [74] R. Breedon. “View through the CMS detector during the cooldown of the
1780 solenoid on February 2006. CMS Collection”, February 2006, CMS-PHO-
1781 OREACH-2005-004, Retrieved from <https://cds.cern.ch/record/930094>.
- 1782 [75] A. Dominguez et. al. “CMS Technical Design Report for the Pixel Detector
1783 Upgrade”, CERN-LHCC-2012-016. CMS-TDR-11.
- 1784 [76] CMS Collaboration. “Description and performance of track and primary-vertex
1785 reconstruction with the CMS tracker,” Journal of Instrumentation, vol. 9, no.
1786 10, p. P10009,(2014).
- 1787 [77] CMS Collaboration and M. Brice. “Images of the CMS Tracker Inner
1788 Barrel”, November 2008, CMS-PHO-TRACKER-2008-002. Retrieved from
1789 <https://cds.cern.ch/record/1431467>.
- 1790 [78] M. Weber. “The CMS tracker”. 6th international conference on hyperons, charm
1791 and beauty hadrons Chicago, June 28-July 3 2004.
- 1792 [79] CMS Collaboration. “Projected Performance of an Upgraded CMS Detector at
1793 the LHC and HL-LHC: Contribution to the Snowmass Process”. Jul 26, 2013.
1794 arXiv:1307.7135
- 1795 [80] L. Veillet. “End assembly of HB with EB rails and rotation in-
1796 side SX ”,January 2002. CMS-PHO-HCAL-2002-002. Retrieved from
1797 <https://cds.cern.ch/record/42594>.

- 1798 [81] J. Puerta-Pelayo.“First DT+RPC chambers installation round in the
 1799 UX5 cavern.”. January 2007, CMS-PHO-OREACH-2007-001. Retrieved from
 1800 <https://cds.cern.ch/record/1019185>
- 1801 [82] X. Cid Vidal and R. Cid Manzano. “CMS Global Muon Trigger” web
 1802 site: Taking a closer look at LHC. Retrieved from https://www.lhc-closer.es/taking_a_closer_look_at_lhc/0.lhc_trigger
 1803
- 1804 [83] WLCG Project Office, “Documents & Reference - Tiers - Structure,” (2014).
 1805 <http://wlcg.web.cern.ch/documents-reference> , last accessed on 30.01.2018.
- 1806 [84] CMS Collaboration, “Search for the associated production of a Higgs boson
 1807 with a single top quark in proton-proton collisions at $\sqrt{s} = 8$ TeV”, JHEP 06
 1808 (2016) 177,doi:10.1007/JHEP06(2016)177, arXiv:1509.08159.
- 1809 [85] B. Stieger, C. Jorda Lope et al., “Search for Associated Production of a Single
 1810 Top Quark and a Higgs Boson in Leptonic Channels”, CMS Analysis Note CMS
 1811 AN-14-140, 2014.
- 1812 [86] M. Peruzzi, C. Mueller, B. Stieger et al., “Search for ttH in multilepton final
 1813 states at $\sqrt{s} = 13$ TeV”, CMS Analysis Note CMS AN-16-211, 2016.
- 1814 [87] CMS Collaboration, “Search for H to bbar in association with a single top quark
 1815 as a test of Higgs boson couplings at $\sqrt{s} = 13$ TeV”, CMS Physics Analysis
 1816 Summary CMS-PAS-HIG-16-019, 2016.
- 1817 [88] B. Maier, “SingleTopHiggProduction13TeV”, February, 2016.
 1818 <https://twiki.cern.ch/twiki/bin/viewauth/CMS/SingleTopHiggsGeneration13TeV>.
- 1819 [89] M. Peruzzi, F. Romeo, B. Stieger et al., “Search for ttH in multilepton final1
 1820 states at $\sqrt{s} = 13$ TeV”, CMS Analysis Note CMS AN-17-029, 2017.

1821 [90] B. WG, “BtagRecommendation80XReReco”, February, 2017.
1822 <https://twiki.cern.ch/twiki/bin/view/CMS/BtagRecommendation80XReReco>.